Statistical Signal Processing Techniques for Coherent Transversal Beam Dynamics in Synchrotrons

Vom Fachbereich 18
Elektrotechnik und Informationstechnik
der Technischen Universität Darmstadt
zur Erlangung der Würde eines
Doktor-Ingenieurs (Dr.-Ing.)
genehmigte Dissertation

von
M.Sc. Mouhammad Alhumaidi
geboren am 01.01.1984 in Raqa (Syrien)

Referent:	Prof. Dr.-Ing. Abdelhak M. Zoubir
Korreferent:	Prof. Dr.-Ing. Harald Klingbeil
Tag der Einreichung:	21.01.2015
Tag der mündlichen Prüfung:	04.03.2015

D 17
Darmstadt, 2015

To my family

Acknowledgments

I would like to thank all people who have supported and inspired me during my doctoral work.

I especially wish to thank Prof. Dr.-Ing. Abdelhak Zoubir for supervising this work. It is really an honor and a pleasure to be supervised by an outstanding professor who gave me a highly inspiring mix of freedom in work and research with guidance that made my time as doctoral student in his Signal Processing Group very pleasurable.

I wish to thank Jürgen Florenkowski, Kevin Lang, Dr. Udo Blell, Thomas Lommel, Dr. Vladimir Kornilov, and Rahul Singh from the GSI Helmholzzentrum für Schwerionenforschung GmbH for the inspiring talks, and technical support and help during the implementation of the TFS project.

I wish to thank Prof. Dr.-Ing. Harald Klingbeil who acted as co-referent of the dissertation.

My thanks go to my ex-colleagues from the Signal Processing Group at TU Darmstadt. I was very happy to work in such a convivial environment. Thanks to Raquel Fandos, Christian Debes, Philipp Heidenreich, Wassim Suleiman, Michael Leigsnering, Jürgen Hahn, Christian Weiss, Adrian Sosic, Sara Al-Sayed, Mark Ryan Balthasar, Nevine Demitri, Michael Fauss, Gökhan Gül, Lala Khadidja Hamaidi, Di Jin, Sahar Khawatmi, Michael Lang, Michael Muma, Tim Schäck, Freweyni Kidane Teklehaymanot, Simon Rosenkranz, Weaam Alkhaldi, Ahmed Mustafa, Fiky Suratman, Feng Yin, Yacine Chakhchoukh, Stefan Leier, Waqas Sharif, Zhihua Lu, Gebremichael Teame, Renate Koschella, and Hauke Fath.

I wish to thank the friends in Darmstadt and the guests of the International Generation Meeting (IGM) who made Darmstadt to my home city in Germany.

I wish to thank my parents Saada & Omar Alhumaidi for their immeasurably great and unconditional love and support since I was born. I wish also to thank my brothers and sisters and the rest of my family.

Last but not least, I am most grateful to my wife Nour Abboud and my son Ryan Alhumaidi for their love, understanding, encouragement, support, and joy.

Kurzfassung

Transversal kohärente Strahlschwingungen können in Synchrotronen direkt nach der Injektion aufgrund der Positions- und Winkelfehler, die durch ungenaue Reaktion des Injektions-Kickers entstehen, auftreten. Darüber hinaus wird der Bedarf nach höheren Strahlintensitäten immer größer bei heutigen Teilchenbeschleunigeranlagen, was zu stärkeren Wechselwirkungen zwischen den Strahlteilchen und den Komponenten des Teilchenbeschleunigers führt, da die Stärke der durch die zu beschleunigenden Teilchen erzeugten Elektromagnetischen Felder bei höherer Strahlintensitäten ansteigt. Dies erhöht folglich das Potential kohärenter Instabilitäten. Dadurch werden unerwünschte Strahlschwingungen auftreten, wenn die natürliche Dämpfung unzureichend wird, die durch die Instabilitäten entstehenden kohärenten Strahlschwingungen zu unterdrücken. Die Instabilitäten und Strahlschwingungen können generell sowohl in transversaler als auch vertikaler Richtung auftreten. In der vorliegenden Arbeit werden nur transversal kohärente Strahlschwingungen betrachtet.

Im Normalbetrieb eines Teilchenbeschleunigers sind transversale Strahlschwingungen unerwünscht, da sie durch das Emittanzwachstum mittels der Dekohärenz der Oszillationen der einzelnen Teilchen des Strahls zu Strahlqualitätsverschlechterung führen. Die Ursache der Dekohärenz der Oszillationen der einzelnen Teilchen ist die Tune-Unschärfe. Bei einem Collider führt die Emittanzaufblähung beispielsweise zu niedrigerer Luminosität und somit schlechterer Kollisionenqualität [1, 2]. Aus diesem Grunde müssen die Strahlschwingungen für einen besseren Betrieb des Teilchenbeschleunigers unterdrückt werden. Zu diesem Zweck sind Transversale Feedback-Systeme (TFS) sehr wirksam. Sie messen die Strahlschwingungen mittels der sogenannten Pickup Sonden (PU) und korrigieren den Strahl dementsprechend mittels Aktuatoren, die als Kicker benannt werden [3, 4].

In dieser Dissertation wird ein neuartiges Konzept zur Verwendung mehrerer PUs für die Schätzung der Strahlablage an der Beschleunigerstelle mit 90° Phasenvorschub vor der Kickerstelle vorgestellt. Die Signale aus den verschiedenen PUs müssen so verzögert werden, dass sie dem gleichen Bunch entsprechen. Anschließend wird eine gewichtete Summe dieser verzögerten Signale als Schätzer des Feedbackkorrektursignals berechnet. Die Gewichtungskoeffizienten werden so berechnet, dass ein erwartungstreuer Schätzer erreicht wird. D.h. der Ausgangswert dieses Schätzers der echten Strahlablage an der Stelle mit 90° Phasenvorschub vor dem Kicker entspricht, wenn die PUs die Strahlablage ohne Rauschen messen würden. Ferner muss der Schätzer minimale Rauschleistung am Ausgang unter allen linearen erwartungstreuen Schätzern bieten. Dieses Konzept wird in einem anderen neuartigen Ansatz zur Bestimmung optimaler

PU-Kicker Stellenkonstellation am Beschleunigerring angewandt. Die Optimalität wird hier im Sinne vom minimalen Rauscheffekt auf die Feedbackqualität betrachtet. Ein neues Design von einem TFS für die Schwerionensynchrotrone SIS 18 und SIS 100 bei der GSI wurden im Rahmen dieser Arbeit entwickelt und auf FPGA implementiert.

Das Korrektursignal vom TFS wird in der Regel basierend auf den Transfermatrizen zwischen den PUs und dem Kicker berechnet. Diese Parameter werden normalerweise von der Beschleunigersteuerung geliefert. Die Transfermatrizen können jedoch aufgrund von Magnetfeld- Fehlern, Imperfektionen, Magneten-Alterung und Versatz von ihren Nominalwerten abweichen. Daher kann die Verwendung der fehlerhaften Nominalwerte der Transfer-Optik in der Berechnung des TFS Korrektursignals zu Feedbackqualitätsverlust und somit Strahlstörungen führen.

Um diese Problematik zu beheben, stellen wir ein neuartiges Konzept für robuste Feedbacksysteme gegenüber Optikfehlern und Ungewissheiten vor. Wir nehmen mehrere PUs und einen Kicker für jede transversale Richtung an. Es werden Störanteile in den Transfermatrizen zwischen den PUs und dem Kicker berücksichtigt. Anschließend wird ein erweiterter Kalman-Filter eingesetzt, um aus den Messwerten an den PUs das Feedbackkorrektursignal sowie die Störterme in den Transfermatrizen zu schätzen.

Des Weiteren stellen wir ein Verfahren zur Messung des Phasenvorschubs sowie der Amplitudenskalierung zwischen dem Kicker und den PUs vor. Direkt nach Anregung durch einen starken Kick werden die PU-Signale erfasst. Anschließend wird der Second-Order Blind Identification (SOBI) Algorithmus zur Zerlegung der aufgezeichneten verrauschten Signale in eine Mischung von unabhängigen Quellen angewandt [5, 6]. Schließlich bestimmen wir die erforderlichen Optik-Parameter durch die Identifizierung und Analyse der durch den Kick entstehenden Betatronschwingung auf der Grundlage ihrer räumlichen und zeitlichen Muster.

Die Magneten der Beschleunigeroptik können unerwünschte lineare und nicht-lineare Störfelder [7] aufgrund von Fabrikationssfehlern oder Alterung erzeugen. Diese Störfelder können unerwünschte Resonanzen anregen, die zusammen mit der Raumladungstuneunschärfe zu langfristigen Strahlverlusten führen können. Dies führt daher zur Verkleinerung der dynamischen Apertur [8–10]. Daher ist die Kenntnis der linearen und nicht-linearen magnetischen Störfelder in der Beschleunigeroptik bei Synchrotronen sehr entscheidend für die Steuerung und Kompensierung potentieller Resonanzen und den daraus folgenden Strahlverlusten und Strahlqualitätsverschlechterungen. Dies ist unabdingbar, insbesondere bei Beschleunigern mit hoher Strahlintensität. Da die Beziehung zwischen den Strahlschwingungen an den PU Stellen eine Manifestierung der Beschleunigeroptik ist, kann sie für die Bestimmung der linearen und nicht-linearen

Optik-Komponenten ausgenutzt werden. So können transversale Strahlschwingungen gezielt zu Diagnosezwecken bei gesondertem Diagnosebetrieb des Beschleunigers angeregt werden.

Wir stellen in dieser Arbeit ein neuartiges Verfahren zur Detektierung und Schätzung nicht-linearer Optikkomponenten auf der zwischen zwei PUs liegenden Strecke mittels der Analyse der erfassten Signale an diesen zwei PUs und einem dritten vor. Abhänging von den nicht- linearen Komponenten auf der Beschleunigeroptik-Strecke zwischen den PUs folgt die Strahlablage an den Stellen dieser PUs einem entsprechenden multivariaten Polynom. Nach der Berechnung der Kovarianzmatrix der Polynomterme setzten wir die Generalized Total Least Squares (GTLS) Methode zur Berechnung der Modellparameter, und somit der nicht-linearen Komponenten, ein. Für die Modellordnungsselektion verwenden wir Hypothesen-Tests mittels Bootstrap-Technik. Konfidenzintervalle der Modellparameter werden ebenfalls durch Bootstrap-Technik bestimmt.

Abstract

Transversal coherent beam oscillations can occur in synchrotrons directly after injection due to errors in position and angle, which stem from inaccurate injection kicker reactions. Furthermore, the demand for higher beam intensities is always increasing in particle accelerators. The wake fields generated by the traveling particles will be increased by increasing the beam intensity. This leads to a stronger interaction between the beam and the different accelerator components, which increases the potential of coherent instabilities. Thus, undesired beam oscillations will occur when the natural damping is not enough to attenuate the oscillations generated by the coherent beam-accelerator interactions. The instabilities and oscillations can be either in transversal or longitudinal direction. In this work we are concerned with transversal beam oscillations only.

In normal operation, transversal beam oscillations are undesired since they lead to beam quality deterioration and emittance blow up caused by the decoherence of the oscillating beam. This decoherence is caused by the tune spread of the beam particles. The emittance blow up reduces the luminosity of the beam, and thus the collision quality [1,2]. Therefore, beam oscillations must be suppressed in order to maintain high beam quality during acceleration. A powerful way to mitigate coherent instabilities is to employ a feedback system. A Transversal Feedback System (TFS) senses instabilities of the beam by means of Pickups (PUs), and acts back on the beam through actuators, called kickers [3, 4].

In this thesis, a novel concept to use multiple PUs for estimating the beam displacement at the position with 90° phase advance before the kicker is proposed. The estimated values should be the driving feedback signal. The signals from the different PUs are delayed such that they correspond to the same bunch. Subsequently, a weighted sum of the delayed signals is suggested as an estimator of the feedback correction signal. The weighting coefficients are calculated in order to achieve an unbiased estimator, i.e., the output corresponds to the actual beam displacement at the position with 90° phase advance before the kicker for non-noisy PU signals. Furthermore, the estimator must provide the minimal noise power at the output among all linear unbiased estimators. This proposed concept is applied in our new approach to find optimal places for the PUs and the kicker around the accelerator ring such that the noise effect on the feedback quality is minimized. A new TFS design for the heavy ions synchrotrons SIS 18 and SIS 100 at the GSI has been developed and implemented using FPGA.

The correction signal of transverse feedback system is usually calculated according to the transfer matrices between the pickups and the kickers. However, errors due

to magnetic field imperfections and magnets misalignment lead to deviations in the transfer matrices from their nominal values. Therefore, using the nominal values of the transfer optics with uncertainties leads to feedback quality degradation, and thus beam disturbances.

Therefore, we address a novel concept for feedback systems that are robust against optics errors or uncertainties. One kicker and multiple pickups are assumed to be used for each transversal direction. We introduce perturbation terms to the transfer matrices between the kicker and the pickups. Subsequently, the Extended Kalman Filter is used to estimate the feedback signal and the perturbation terms using the measurements from the pickups.

Moreover, we propose a method for measuring the phase advances and amplitude scaling between the positions of the kicker and the Beam Position Monitors (BPMs). Directly after applying a kick on the beam by means of the kicker, we record the BPM signals. Subsequently, we use the Second-Order Blind Identification (SOBI) algorithm to decompose the recorded noised signals into independent sources mixture [5, 6]. Finally, we determine the required optics parameters by identifying and analyzing the betatron oscillation sourced from the kick based on its mixing and temporal patterns.

The accelerator magnets can generate unwanted spurious linear and non-linear fields [7] due to fabrication errors or aging. These error fields in the magnets can excite undesired resonances leading together with the space charge tune spread to long term beam losses and reducing dynamic aperture [8–10]. Therefore, the knowledge of the linear and non-linear magnets errors in circular accelerator optics is very crucial for controlling and compensating resonances and their consequent beam losses and beam quality deterioration. This is indispensable, especially for high beam intensity machines. Fortunately, the relationship between the beam offset oscillation signals recorded at the BPMs is a manifestation of the accelerator optics, and can therefore be exploited in the determination of the optics linear and non-linear components. Thus, beam transversal oscillations can be excited deliberately for purposes of dignostics operation of particle accelerators.

In this thesis, we propose a novel method for detecting and estimating the optics lattice non-linear components located in-between the locations of two BPMs by analyzing the beam offset oscillation signals of a BPMs-triple containing these two BPMs. Depending on the non-linear components in-between the locations of the BPMs-triple, the relationship between the beam offsets follows a multivariate polynomial accordingly. After calculating the covariance matrix of the polynomial terms, the Generalized Total Least Squares method is used to find the model parameters, and thus the non-linear

components. A bootstrap technique is used to detect the existing polynomial model orders by means of multiple hypothesis testing, and determine confidence intervals for the model parameters.

Contents

Chapter 1

Introduction and Motivation

Particle accelerators are facilities for accelerating charged particles by means of electromagnetic fields. They are very important devices for fundamental and applied research in physics and have a wide range of applications. They can be used as colliders, light sources, in particle therapy for treating tumors to fight cancer, or in many other applications [11, 12].

The very first concepts of particle accelerators were based on electrostatic fields, like the Cockcroft and Walton as well as the Van de Graaff accelerator. The acceleration capability of such concepts is however limited by the breakdown voltage. Therefore, new concepts of particle accelerators using alternating electromagnetic fields were developed meanwhile. The main topology of particle accelerators can be either linear or circular. In linear accelerators, particles are accelerated in a straight line where the acceleration capability is limited by the length of the accelerator. The advantage of Circular accelerators over linear ones is that the particles can travel very long distances during acceleration to nearly reach the speed of light. Therefore, they usually allow much higher energies. Linear accelerators are usually employed as injector into circular accelerators. Synchrotrons are the most powerful modern circular accelerators. They can nowadays provide energies up to some TeV like the Large Hadron Collider (LHC) at CERN.

1.1 Motivation

Beam transversal oscillations are undesired since they lead to beam quality deterioration and emittance blow up caused by the decoherence of the oscillating beam. This decoherence is caused by the tune spread of the beam particles. The emittance blow up reduces the luminosity of the beam, and thus the collision quality [1, 2]. Therefore, beam oscillations must be suppressed in order to maintain high beam quality during acceleration. A powerful way to mitigate coherent instabilities is to employ a feedback system. A Transversal Feedback System (TFS) senses instabilities of the beam by means of Pickups (PUs), and acts back on the beam through actuators, called kickers [3, 4].

In general, the signals at the PUs are disturbed by noise, which could make the Signal-to-Noise power Ratio (SNR) unacceptably low. This will worsen the feedback correction quality as it leads to beam heating [13,14] and emittance blow up [4]. For this issue, we address in this work a novel approach for mitigating noise at the PUs using more than two PUs at different positions to estimate the feedback correction signal. Furthermore, we address another approach for finding the best positions to place the PUs and the kicker among all possible free locations around the accelerator ring, which are not occupied by other accelerator devices. The PUs and the kicker should be placed such that the noise generated at the PUs causes the smallest disturbance to the feedback quality.

The feedback signal is calculated based on the accelerator optics, i.e., the transfer matrices between the PUs and the kicker. Thus, any deviations in the optics parameters from the known nominal values lead to perturbations in the calculated feedback signal. Therefore, the beam will be disturbed and get worse. There are many reasons for optics errors in particle accelerators, e.g., magnetic field imperfections and magnets misalignments. Consequently, the optics transfer between the kicker and the PUs must be measured precisely in order to get real values and reach a better feedback quality. In this work, we address a method for measuring the phase advance and amplitude ratio between the beam oscillation at the kicker and the PUs positions. A novel concept for robust feedback system against optics errors or uncertainties is addressed in this work as well.

The accelerator magnets can generate unwanted spurious linear and non-linear fields [15] due to fabrication errors or aging. These error fields in the magnets can excite undesired resonances leading together with the space charge tune spread to long term beam losses and reducing dynamic aperture [16, 17]. Therefore, these magnets errors and their impact on the beam must be studied and evaluated in order to control and compensate them for better machine operation, such that the demand for higher beam intensity can be fulfilled. Thus, the measurement of the linear and non-linear error components in circular accelerator optics is indispensable, especially for high intensity machines. In this work, we address a novel Lightweight approach for exploiting transversal beam oscillations to detect and determine optics linear and non-linear components in a circular particle accelerator without requiring extensive measurement campaigns.

1.2 State-of-the-Art

The feedback correction signal applied by the kicker of the TFS must have a 90° phase advance with respect to the betatron oscillation signal at the kicker position in order to have a damping impact. This can be achieved by passing the signal of one PU through a feedback filter, e.g., finite impulse response (FIR) filter with suitable phase response at the fractional tune frequency, with proper delay [4]. The number of the filter taps can be increased in order to have more degrees of freedom for optimizing the filter response, e.g., to have maximum flatness around the working point for robustness against tune changes [4,18], higher selectivity for better rejection of undesired frequency components [4], minimum amplitude response at specific frequencies that should not be fed back [19], stabilize different tune frequencies simultaneously [20]. Advanced concepts from the control theory have been applied also in the design of the feedback filter [21]. These approaches introduce however extra turns delay depending on how many taps the FIR filter consists of.

In [3], an approach was proposed to calculate the feedback correction signal using PUs located at two different positions along the accelerator ring for each of the horizontal and vertical directions, which is the smallest number of PUs for determining the beam trace space since only beam offsets can be measured by the PUs, but not the angles of the beam. Nevertheless, this approach does not consider the harmful noise at the PUs neither the robustness of the system against unwanted deviations.

The closed orbit (CO) response to the steering angle change, i.e., orbit response matrix (ORM), has been exploited to provide information on the linear magnetic field errors [22–24]. In [8,9,25], the Non-Linear Tune Response Matrix (NTRM) technique has been proposed to be used to diagnose non-linear magnetic field components, which extends the ORM analogy to the non-linear errors. In this method the tune response to the deformed closed orbit is explored for the reconstruction of sextupolar components [8]. The utilization of non-linear chromaticity measurement in determining the non-linear optics model has been presented in [26,27]. These methods are however very costly and require extensive measurement campaigns since the tune must be measured many times over different steering constellations. Furthermore, they have difficulties in estimating non-linear components with mixed and higher orders.

1.3 Contributions

The major contributions of this thesis are listed in the following:

- **TFS Noise Power Minimization:** A novel concept to use multiple PUs for estimating the beam displacement at the position with 90° phase advance before the kicker is proposed. The estimated values should be the driving feedback signal. The signals from the different PUs are delayed such that they correspond to the same bunch. Subsequently, a weighted sum of the delayed signals is suggested as an estimator of the feedback correction signal. The weighting coefficients are calculated in order to achieve an unbiased estimator, i.e., the output corresponds to the actual beam displacement at the position with 90° phase advance before the kicker for non-noisy PU signals. Furthermore, the estimator must provide the minimal noise power at the output among all linear unbiased estimators. This proposed concept is applied in our new approach to find optimal places for the PUs and the kicker around the accelerator ring such that the noise effect on the feedback quality is minimized.

  A new TFS design for the heavy ions synchrotrons SIS 18 and SIS 100 at the GSI has been developed and implemented on an FPGA board using the hardware description language VHDL. Furthermore, many tests and measurements with the system electronic modules and sub-modules has been conducted in the lab and with real beam in the accelerator during the system implementation phase. Many hardware operation and implementation challenges have been solved on the way to the system integration.

- **TFS with Optics Uncertainties:** A method for measuring the phase advances and amplitude scaling between the positions of the kicker and the BPMs is proposed. Directly after applying a kick on the beam by means of the kicker, we record the BPM signals. Consequently, we use the Second-Order Blind Identification (SOBI) algorithm to decompose the noised recorded signals into independent sources mixture. Finally, we determine the required optics parameters by identifying and analyzing the betatron oscillation sourced from the kick based on its mixing and temporal patterns.

  Furthermore, we address a novel concept for robust feedback system against optics errors or uncertainties. This concept can be applied independently as an alternative of the previous method using optics parameters with uncertainties due to the robustness. A kicker and multiple pickups are assumed to be used for each transversal direction. We introduce perturbation terms to the transfer matrices between the kicker and the pickups, which are important for the calculation of the feedback correction signal. Subsequently, the Extended Kalman Filter is used to estimate the feedback signal and the perturbation terms by means of the measurements from the pickups. The observability of the proposed model has been analyzed and proven within this thesis.

- **Non-Linear Optics Components Detection and Measurement:** A novel method for estimating lattice non-linear components located in-between the positions of two BPMs by analyzing the beam offset signals of a BPMs triple containing these two BPMs is proposed. Depending on the nonlinear components in-between the locations of the BPMs triple, the relationship between the beam offsets follows a multivariate polynomial. After calculating the covariance matrix of the polynomial terms, the Generalized Total Least Squares method is used to find the model parameters, and thus the non-linear components. Subsequently, detection and orders determination of the non-linear components is achieved using multiple testing for restricted combinations based on bootstrap techniques. bootstrap techniques are also used to determine confidence intervals for the model parameters.

1.4 Publications

Internationally Refereed Journal Articles

- M. Alhumaidi and A.M. Zoubir, "Using Multiple Pickups for Transverse Feedback Systems and Optimal Pickups-Kicker Placement for Noise Power Minimization". Submitted to *Nuclear Instruments and Methods in Physics Research A*.
- M. Alhumaidi and A.M. Zoubir, "Bootstrap Techniques for the Detection of Optics Non-Linear Components in Particle Accelerator". To be submitted.

Internationally Refereed Conference Papers

- M. Alhumaidi and A.M. Zoubir, "Optics Non-Linear Components Measurement Using BPM Signals". In *Proceedings of the 2nd International Beam Instrumentation Conference (IBIC 2013)*, pp. 279 - 282, Oxford, UK, September 2013.
- T. Rueckelt, M. Alhumaidi and A.M. Zoubir, "Realization of Transverse Feedback System for SIS18/100 using FPGA". In *Proceedings of the 2nd International Beam Instrumentation Conference (IBIC 2013)*, pp. 128 - 131, Oxford, UK, September 2013.
- M. Alhumaidi and A.M. Zoubir, "Determination of Optics Transfer Between the Kicker and BPMs for Transverse Feedback System". In *Proceedings of the 4th International Particle Accelerator Conference (IPAC'13)*, pp. 2923 - 2925, Shanghai, China, May 2013.

- M. Alhumaidi and A.M. Zoubir, "A Robust Transverse Feedback System". In *Proceedings of the 3rd International Particle Accelerator Conference (IPAC'12)*, pp. 2843 - 2845, New Orleans, Louisiana, USA, May 2012.
- M. Alhumaidi and A.M. Zoubir, "A Transverse Feedback System using Multiple Pickups for Noise Minimization". In *Proceedings of the 2nd International Particle Accelerator Conference (IPAC'11)*, pp. 487 - 489, San Sebastin, Spain, September 2011.

Technical Reports

- M. Alhumaidi, U. Blell, J. Florenkowski and V. Kornilov, "TFS for SIS18/SIS100". In *GSI Scientific Report 2012*.
- M. Alhumaidi, U. Blell, J. Florenkowski and V. Kornilov, "Status and Results of the TFS for SIS18/SIS100". In *GSI Scientific Report 2013*.

1.5 Thesis Overview

The thesis is outlined as follows: Chapter 2 presents an introduction to particle accelerators, synchrotrons in particular. It describes the focusing, and particle transversal movement model. Furthermore, it gives an overview of possible sources for beam instabilities and oscillations.

Chapter 3 describes the TFS, and considers the problem of the minimization of the noise power applied by the TFS on the beam. The use of multiple PUs, and finding the optimal places for the PUs and the kicker around the accelerator ring are addressed in this chapter.

In Chapter 4, the problem of the TFS with optics uncertainties is considered. A method for determining the optics transfer between the kicker and the PUs, as well as the robustification of the TFS against optics uncertainties are addressed here.

Non-linear optics components detection and estimation are considered in Chapter 5. The problem of orders determination, and confidence interval estimation for the non-linear model parameters are tackled in this chapter.

Conclusions are summarized in Chapter 6. An outlook for future work is presented in this chapter as well.

Chapter 2

Transversal Particle Movement in Synchrotrons

This chapter gives an introduction to the physics ruling the particle movement in the synchrotron, particularly in the transversal direction. The general structure of a synchrotron is firstly presented. The optics and focusing principles and equations in synchrotrons are discussed here. Potential sources for beam instabilities are lastly introduced.

2.1 Synchrotron

A synchrotron is a special type of cyclic accelerators with time dependent magnetic and electric fields. It is called synchrotron since the electromagnetic fields must be synchronized with the accelerated beam of particles [28–33].

The movement of charged particles in accelerators is enforced by the Lorentz force given by

$$\vec{F} = q(\vec{E} + \vec{V} \times \vec{B}), \tag{2.1}$$

where $\vec{E}$ is the electric field, $\vec{B}$ the magnetic field, $\vec{V}$ the particle speed, and q the particle charge.

Since the particles travel very long distances inside synchrotrons, transverse focusing is a major function of an accelerator. Equation (2.1) shows that the magnetic force is perpendicular to the particle direction, and can only lead to beam deflection without increasing velocity. Therefore in high energy accelerators, magnetic fields are employed for focusing and bending, and electric fields for acceleration. The electric fields are usually generated by resonance cavities, and magnetic fields by electric magnets. The bending is usually done via uniform magnetic fields generated by dipolar electric magnets, and focusing via magnetic field gradients generated by quadrupolar electric magnets [28–33].

Figure 2.1 shows an overview of the heavy ions synchrotron SIS 18 at the GSI in Darmstadt, Germany [3, 34]. One can see from the figure that this synchrotron is

composed of 12 periods. The red parts are the bending (deflecting) dipole magnets. The yellow parts represent the quadrupole magnets. The two accelerating cavities are shown as well.

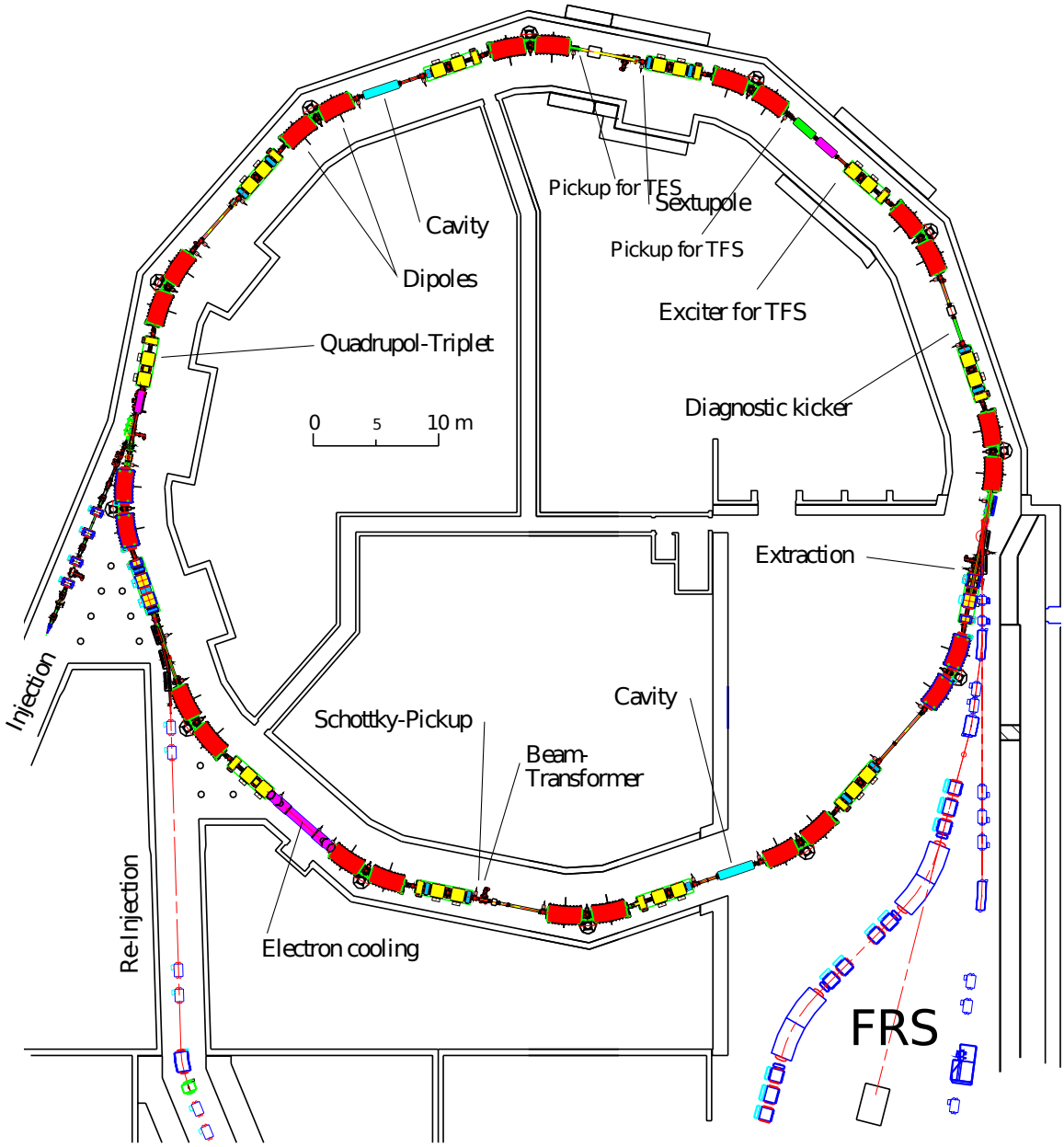

Figure 2.1. Heavy ions synchrotron SIS 18 at the GSI [3, 34].

In the free space (vacuum), we have from the Maxwell's equations $\nabla \times \vec{B} = \vec{0}$, since no currents exist and no electric fields are generated by the magnets. Leading to

$$\frac{\partial B_y}{\partial x} = \frac{\partial B_x}{\partial y}. \tag{2.2}$$

The quadrupole magnetic field can be written as

$$B_x = B_0 \frac{y}{a},\ B_y = B_0 \frac{x}{a}. \tag{2.3}$$

The focusing strength for a quadrupole magnet is defined as [28, 35]

$$\kappa_x = \frac{q}{p_0} \frac{\partial B_y}{\partial x}, \kappa_y = -\frac{q}{p_0} \frac{\partial B_x}{\partial y}. \tag{2.4}$$

Therefore, magnetic field gradients that provide focusing in the horizontal direction x, provide defocusing in the vertical direction y and vice versa. This motivates the use of FODO cells [28, 31, 32].

2.1.1 FODO Cells

Most of synchrotrons, storage rings, as well as beam transfer lines are composed of periodic segments of focusing/defocusing quadrupoles with drift tubes in-between. This is the strong focusing concept of the so called FODO cells. Figure 2.2 shows an example for a sequence of two FODO cells.

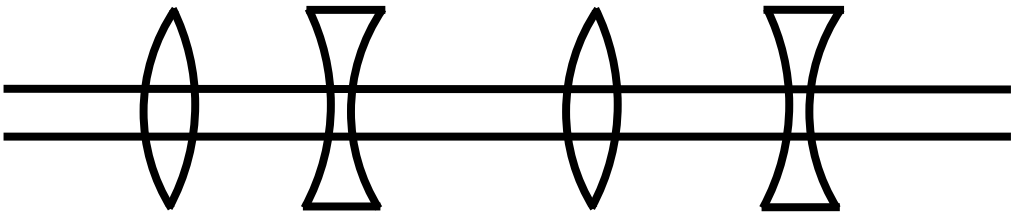

Figure 2.2. FODO cells.

With this optics structure, the focusing strength κ alternates between positive (focusing), zero (drift tube), and negative (defocusing) in each transverse direction. Using the general movement equations $\dot{p}_x = F_x$ and $\dot{p}_y = F_y$ one can write the particle transversal movement equation in FODO cells after neglecting the effect of dipole magnets as

$$x''(s) + \kappa(s)x(s) = 0 \tag{2.5a}$$

$$y''(s) - \kappa(s)y(s) = 0, \tag{2.5b}$$

these are the so called Hill equations, where s denotes the longitudinal position around the accelerator ring.

2.1.2 Particle Movement

The transversal movement of the particles inside a synchrotron is described by the solution of Equations (2.5). When the function $\kappa(s)$ is periodic, i.e., $\kappa(s+L) = \kappa(s)$ for some positive value L, i.e., the circumference of a circular accelerator, the transversal movement equations can be solved by the Courant-Snyder ansatz. We show the solution only for $x(s)$ since the solution for $y(s)$ has the same form. The general solution for the Hill equation is given as [28, 36, 37]

$$x(s) = \sqrt{\epsilon}\sqrt{\beta(s)}\cos(\Psi(s) + \Psi_0), \tag{2.6}$$

where

$$\Psi'(s) = \frac{1}{\beta(s)}. \tag{2.7}$$

The betatron function $\beta(s)$ is a continuous function, which depends on the focusing strength $\kappa(s)$ and thus the lattice structure. ϵ and Ψ_0 depend on the initial conditions. Equation (2.7) shows that the phase of the betatron motion $\Psi(s)$ changes faster for smaller values of $\beta(s)$.

The number of betatron oscillations a particle does after one turn is called the tune Q. It is a very important machine parameter, where the optics lattice must be designed such that the working point of the tunes is set far from resonance points. The tune can be calculated based on Equation (2.7) as

$$Q = \frac{1}{2\pi}\int_0^L \frac{1}{\beta(s)}ds. \tag{2.8}$$

Equation (2.6) can alternatively be written as

$$x(s) = a_0\sqrt{\beta(s)}\cos(\Psi(s)) + b_0\sqrt{\beta(s)}\sin(\Psi(s)). \tag{2.9}$$

Without loss of generality, we consider the starting position $s = 0$ such that $\Psi(0) = 0$. the derivative of x with respect to s at this position is then given by

$$x'(0) = -a_0\frac{\alpha(0)}{\sqrt{\beta(0)}} + b_0\frac{1}{\sqrt{\beta(0)}}, \tag{2.10}$$

with

$$\alpha(s) = -\frac{\beta'(s)}{2}. \tag{2.11}$$

One finds therefore

$$a_0 = \frac{x(0)}{\sqrt{\beta(0)}}, \tag{2.12a}$$

$$b_0 = \sqrt{\beta(0)}x'(0) + \frac{\alpha(0)}{\sqrt{\beta(0)}}x(0). \tag{2.12b}$$

By substituting Equations (2.12) in Equation (2.9) and the derivative of $x(s)$, and solving the system of equations one can write in matrix form

$$\begin{pmatrix} x(s) \\ x'(s) \end{pmatrix} = \mathbf{M} \cdot \begin{pmatrix} x(0) \\ x'(0) \end{pmatrix}, \tag{2.13}$$

where the transfer matrix is given by

$$\mathbf{M} = \begin{pmatrix} \sqrt{\frac{\beta}{\beta_0}}[\cos(\Psi) + \alpha_0 \sin(\Psi)] & \sqrt{\beta\beta_0}\sin(\Psi) \\ \frac{-1}{\sqrt{\beta\beta_0}}[(1+\alpha\alpha_0)\sin(\Psi) + (\alpha - \alpha_0)\cos(\Psi)] & \sqrt{\frac{\beta_0}{\beta}}[\cos(\Psi) - \alpha\sin(\Psi)] \end{pmatrix}, \tag{2.14}$$

where $\beta = \beta(s)$, $\beta_0 = \beta(0)$, $\alpha = \alpha(s)$, $\alpha_0 = \alpha(0)$, and $\Psi = \Psi(s)$.

Equation (2.13) shows that the beam displacement x and angle x' can be calculated at any position around the accelerator ring by knowing them at an initial position via a transfer matrix dependency.

This section deals with particle movement ruled by the linear, i.e., ideal, lattice structure of the particle accelerator. Generally however, non-linear optics components are present. This can be intentionally placed for other purposes, e.g., for chromaticity correction or Landau damping increase, or it can be non-linear error components in the lattice magnets. In this situation, the relationship between the beam oscillation signals at different PUs is a manifestation of the accelerator optics linear and non-linear components, and can therefore be exploited in the determination of the optics linear and non-linear components [38].

2.1.3 Emittance

According to Liouville's theorem one can see that trace space of particles with the same value ϵ fulfills at every location s the equation [28, 36, 37]

$$\gamma x^2 + 2\alpha x x' + \beta x'^2 = \epsilon, \tag{2.15}$$

where

$$\gamma(s) = \frac{1 + \alpha(s)^2}{\beta(s)}, \tag{2.16}$$

β, α, and γ are called Courant-Snyder parameters.

This defines the so called trace space ellipse. At different locations along the accelerator ring, the betatron function changes, and the trace space ellipses will have different shapes and/or orientations. The surface of the ellipse will however stay constant, i.e., $\pi\epsilon$. Figure 2.3 shows an example trace space ellipse with typical extreme values of x and x'.

The emittance of the beam, ϵ_b, is defined such as the area of the trace space ellipse contains some portion, e.g., 95%, of the beam particles [28].

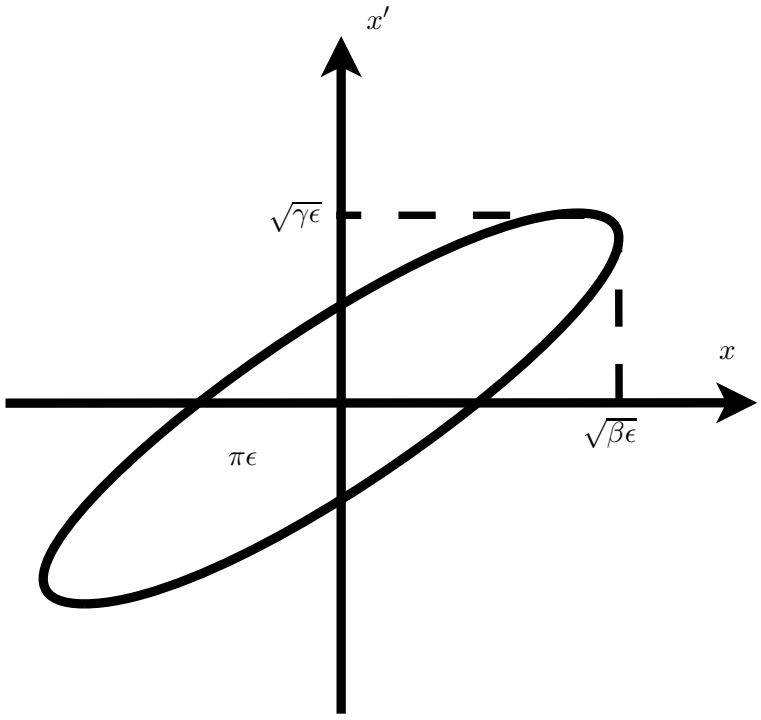

Figure 2.3. Trace space ellipse.

Thus, the emittance of a particle distribution is a metric for beam quality, which shows how compact the beam particles are together.

The higher the emittance, the worse is the beam. Luminosity, which is the quantity that measures the ability of a particle accelerator to produce the required number of interactions, is proportional to the inverse of the emittance [39].

Since the vacuum tube of an accelerator has a limited radius a, the allowed beam emittance is limited. Thus, the admittance of the accelerator is defined as the maximally

allowed beam emittance given as [35]

$$\epsilon_{b,max} = \frac{a^2}{\beta}. \tag{2.17}$$

The emittance growth is a crucial issue in particle accelerators. It limits the machine performance since it increases the beam losses and luminosity degradation. The key idea behind the emittance growth is the filamentation. This can be explained as follows: The rotational frequency of the particles in the phase space gets amplitude dependent when non-linear components or imperfections exist in the accelerator optics. Therefore, any initial displacement of the beam center of mass will be smeared out after some turns to fill the phase space ellipse [40]. The same happens when a mismatched injection of the beam occurs. A mismatched injection means that the phase space distribution of the injected beam does not have the same shape as the phase space ellipse of the accelerator at the injection position. The beam coherent instabilities, i.e., sources of exponential oscillation amplitude growth, lead usually to exponential emittance growth in time.

In Figure 2.4, an example of how the filamentation occurs for a mismatched beam is depicted. One can see here that the surface covered by the beam particles after full filamentation is higher than the surface covered by the initial beam.

2.2 Beam Instabilities

The focusing fields of the lattice optics in a particle accelerator are normally designed such that the beam particles oscillate in transversal direction around the ideal orbit. However, as traveling charged particles the beam generates own electromagnetic fields, i.e., the so called wake fields. These wake fields will interact with the accelerator objects, e.g., the walls of the vacuum tube. The wake fields generated by particles affect the particles behind them. That means that the motions of the particles affect each others and lead to coherent motions. These interactions are usually represented by the so called coupling impedances [41–43]. The accelerator can be seen in this sense as a feedback system, where any transverse perturbation in the beam distribution may be amplified (or damped) by the electromagnetic forces generated by the perturbation itself [44].

The coupling impedances coming from several sources add up together and can get large at some frequencies leading to exponential beam oscillation growth, i.e., coherent

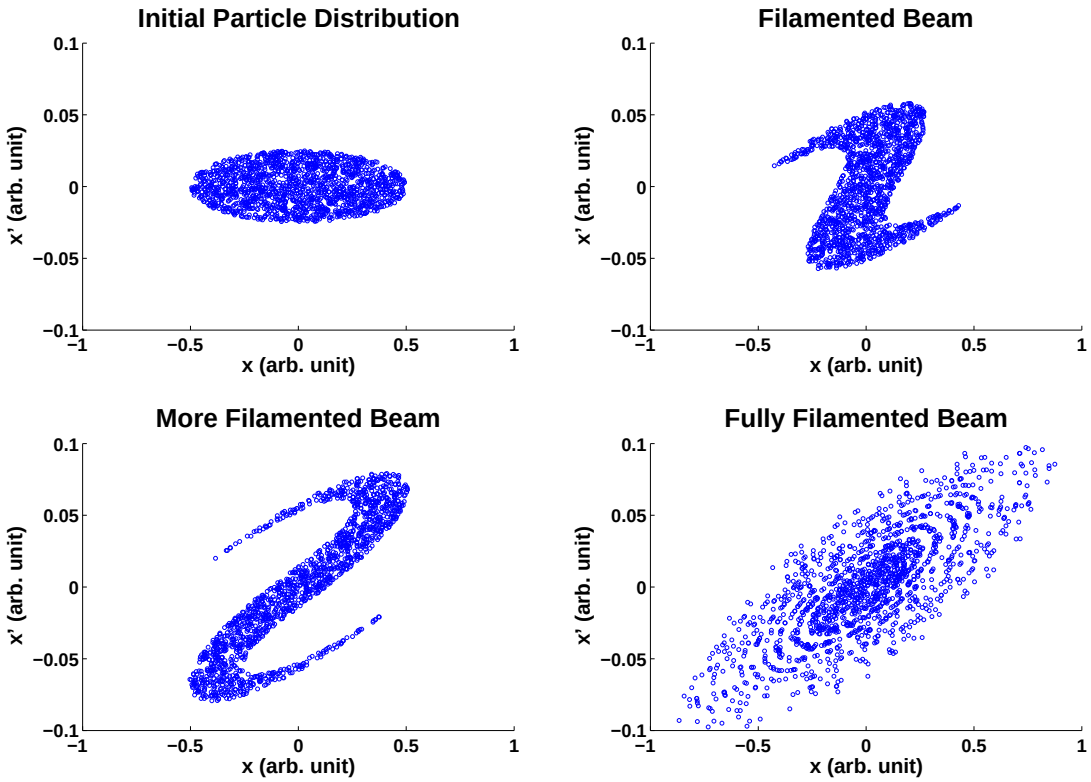

Figure 2.4. Beam filamentation.

instabilities. These so called "collective effects" are responsible for many phenomena which limit the performance of an accelerator in terms of beam quality and stored current [44]. Although nonlinear effects may sometimes limit the growth of the oscillations, the resulting particle dilution and/or loss gets usually unacceptable [43].

The wake fields are called so, because for very high particle velocities they are left mainly behind the traveling charges. For circular accelerators, the frequency domain analysis is usually adopted due to the intrinsic periodicity. There we need to compute the Fourier transform of the wake function. The wake function is defined as the wake potentials per unit charge [44]. The transverse coupling impedance is given as the Fourier transform of the transverse wake function $W_\perp(z)$, i.e., [44–50]

$$Z_\perp(\omega) = \frac{j}{c} \int_{-\infty}^{\infty} W_\perp(z) e^{-j\omega\frac{z}{c}} dz, \tag{2.18}$$

where c denotes the speed of light in vacuum.

The transverse coupling impedance can also be seen as the integral of the deflecting electromagnetic forces over one turn normalized by the dipole moment of the beam

current. It describes in other words the Lorentz forces acting on the beam due to the surroundings, i.e., the accelerator components [3, 49, 50]. Due to the increasing demand for higher beam intensities in modern particle accelerators, the forces acting on the beam get higher, which leads to more dangerous beam instabilities and losses [4].

The transverse wake function is the outcome of the effects of all accelerator components. For a given component, it is basically its Green function in time domain, i.e., response to a pulse excitation [50]. The transverse coupling impedance is a characteristic of the beam environment, i.e., the accelerator, but not of the beam itself.

The transverse coupling impedance given in Equation (2.18) is a complex function. The real part of this function is called the resistive part, and is responsible for the growth or damping of beam coherent oscillations. The imaginary part in contrast induces tune shift [3, 51]

In general, there are many sources for potential beam instabilities. We give in the following an overview of the major components and sources of the transverse coupling impedance in particle accelerator rings [3, 4, 51, 52].

2.2.1 Resistive Wall Impedance

The resistive wall impedance is one of the main sources for beam instabilities in synchrotrons and storage rings [53]. Its instabilities occur due to the interaction of the beam with the walls of the vacuum tube. The reason for these instabilities is the finite resistivity of the vacuum tube walls causing the so called skin effect [3, 4]. The resistive wall instability depends generally on the aperture and material of the vacuum tube walls. The standard transverse impedance for a thick wall of length L is given by [3, 4, 51, 54]

$$Z_{\perp}^{RW} = (1 - j\mathtt{sign}(\omega))\frac{LZ_0}{2\pi a^3}\sqrt{\frac{2c}{Z_0\sigma}}\frac{1}{\sqrt{|\omega|}}, \tag{2.19}$$

where Z_0 denotes the impedance of free space, a the radius of the vacuum tube, and σ the conductivity of the tube wall material. One can notice from this formula that the resistive wall effects are mainly very dangerous in the lower frequency band. This demands accurate impedance calculation in the low frequency (LF) range where the beam pipe and possibly also the structures behind the pipe are the dominating impedance sources [53].

2.2.2 Cavity High Order Modes

High spurious resonances of the particle accelerator cavity structure can be excited by the traveling beam and act back on the beam itself. High Order Modes (HOMs) of the cavities can couple with the wake fields generated by the beam particles, depending on the beam distribution, and affect the following particles leading to resonances, which increase the beam instabilities. This can occur in the horizontal as well as vertical direction [4,55]. This kind of instabilities affects the beam around the HOM resonance frequencies of the cavity. Therefore, its coupling impedance will have peaks at these resonance frequencies.

Beam instabilities due to cavity HOM can be mitigated through proper design of the cavity structure and employing mode dampers, e.g., antennas and resistive loads [4,56]. The full HOM spectrum of the cavity has to be analyzed already during the design phase in order to identify potentially dangerous modes, and to define their damping requirements. This can be achieved using beam simulation codes dedicated for this purpose [55].

2.2.3 Other Beam Instability Sources

Vacuum chamber discontinuities, or abrupt changes of the vacuum chamber cross section, can excite beam instabilities. Furthermore, small cavity-like structures located along the vacuum chamber, e.g., in the Beam Position Monitors (BPMs), can interact with beam such that HOMs of these structures get excited [3, 4]. The effect of these instability sources can be reduced by a proper design of the vaccum chamber and the various installed objects and devices of the accelerator [4, 57].

Depending on the shape of the beam profile, capacitive coupling of the beam with the wall of the vacuum chamber will occur. This is the so called space charge impedance, which has a pure imaginary contribution to total impedance of the particle accelerator. This coupling is basically dominant for non-relativistic beams, i.e., at lower energy [3].

The molecules of the rest gas in the vacuum chamber can be ionized through the collisions with the traveling charged beam. The interaction of the ionized molecules of the rest gas with traveling beam can lead to coherent resonant oscillations [4].

We have given so far an overview of the most important potential sources for beam coherent instabilities and possible cures. Besides these suggested cures that reduce

unwanted beam instabilities by acting directly on the sources, there are many other methods used in particle accelerators [4]. We give a short overview of these methods in the following subsection.

2.2.4 Generic Countermeasures

Coherent bunch instabilities can be mitigated by increasing the Landau damping. This can be achieved by increasing the betatron tune spread via increasing the momentum spread of the beam particles [4, 56]. The demand for higher beam intensities is always increasing for modern accelerators. This leads to stronger interaction between the traveling beam and accelerator objects, which increases the potential of coherent transversal instabilities. Therefore, passive measures become not enough to attenuate the beam oscillations and instabilities generated by the coherent beam-accelerator interactions. Thus, active measures by means of feedback system must be employed.

Chapter 3

Transverse Feedback System and Noise Minimization

In this chapter, we give an introduction to Transverse Feedback Systems (TFS). Further, we explain our proposed novel concept to use multiple pickups (PUs) for estimating the beam displacement at the position with 90° phase advance before the kicker position. The estimated values should be the driving feedback correction signal. The signals from the different PUs are delayed such that they correspond to the same bunch in every sample. Subsequently, a weighted sum of the delayed signals is suggested as an estimator of the feedback correction signal. The weighting coefficients are calculated in order to achieve an unbiased estimator, i.e., the output corresponds to the actual beam displacement at the position with 90° phase advance before the kicker for non-noisy PU signals. Furthermore, the estimator must provide the minimal noise power at the output among all linear unbiased estimators.

Further, this concept is applied in a new approach to find optimal places for the pickups and the kicker around the accelerator ring such that the noise effect on the feedback quality is minimized. Simulation results and system design for the heavy ions synchrotrons SIS 18 at the GSI are given at the end of this chapter.

3.1 Motivation

Transversal coherent beam oscillations have many sources in synchrotrons. They can occur directly after injection due to inaccurate injection kicker reactions leading to errors in position and angle of the beam after injection. Furthermore, the demand for higher beam intensities in modern particle accelerator facilities is always growing. The consequence of higher beam intensities is the increase of the interaction between the traveling beam and accelerator components, which strengthen the potential of coherent transversal instabilities. Thus, beam oscillations will occur when the natural damping becomes not enough to attenuate the oscillations generated by the coherent beam-accelerator interactions [4].

Due to the tune spread of the beam particles, de-coherence and filamentation will occur to the oscillating beam. That leads to emittance blow up, which is harmful

to the beam since it deteriorates the beam quality by increasing the beam losses and reducing the luminosity of colliders [1,58], i.e., number of interactions (useful collisions) per second [1,2,39]. Therefore, strong beam oscillations can not be tolerated, and must be suppressed in order to maintain high beam quality during acceleration cycle.

Coherent bunch instabilities can be mitigated by optimizing and controlling the particle accelerator objects and modules and their coupling impedances, and by increasing the Landau damping of the beam. This can be be achieved by increasing the betatron tune spread through increasing the momentum spread of the beam particles [4,56]. However, the always increasing demand for higher beam intensities leads to the fact that passive measures lack of the ability to stabilize the beam oscillations and instabilities. Thus, active measures by means of feedback system must be employed [4].

A very powerful mean for suppressing the coherent beam instabilities is the use of feedback systems. Transversal Feedback Systems (TFS) sense the instabilities of the beam by means of sensors, called Pickups (PUs), and act back on the beam by means of actuators, called kickers [3, 4].

3.2 Transverse Feedback System

The beam coherent oscillation can be modeled by the differential equation of a harmonic oscillator [4]

$$x''(t) + 2Dx'(t) + \omega^2 x(t) = F(t), \tag{3.1}$$

where D denotes the natural damping, e.g., due to synchrotron radiation. ω denotes the eigenfrequency of the oscillator, i.e., the betatron frequency in this case. The driving force $F(t)$ represents the coupling with other particles and the interaction with the accelerator objects.

With coherent instabilities, the oscillations of the individual particles become correlated and the center of mass of the bunches or beam slices oscillates coherently with the other bunches. Thus each bunch or beam slice oscillate with rising amplitude according to [4, 59]

$$x''(t) + 2(D - G)x'(t) + \omega^2 x(t) = 0, \tag{3.2}$$

with the growth time constant of the coherent instabilities $\tau_G = \frac{1}{G}$.

The solution of Equation (3.2) can be stated as [4]

$$x(t) = ke^{-\frac{t}{\tau}} sin(\omega t + \phi), \tag{3.3}$$

where $\tau = \frac{1}{D-G}$. The beam becomes stable when $D \geq G$, otherwise the beam oscillation grows exponentially.

The TFS action must affect the beam motion by compensating the growth rate. This happens when the feedback correction signal applies to the beam a force proportional to the derivative of the beam oscillation, i.e., $F_{fb}(t) = -2D_{fb}x'(t)$, such that the beam oscillation equation turns to

$$x''(t) + 2(D - G + D_{fb})x'(t) + \omega^2 x(t) = 0. \tag{3.4}$$

The TFS will be able to stabilize the beam, i.e., damp the beam oscillation, when its gain fulfills the following inequality

$$D - G + D_{fb} > 0. \tag{3.5}$$

Depending on the way how the feedback system senses and acts back on the beam instabilities, there are two main types [4]:

- **Frequency domain TFS:** Controls unstable beam modes in frequency domain. It is also called Mode-by-mode TFS. This concept is feasible when the number of potentially unstable frequencies is small enough, otherwise alternative time domain feedback must be employed.
- **Time domain TFS:** acts on the beam based on each sampled value by the Beam Position Monitor (BPM). When the action rate gets less, and every bunch of the beam gets one turn-by-turn kick, it is called bunch-by-bunch feedback system. The correction signal for each sample must act on the same beam slice corresponding to that sample via proper adjustable delay lines. This is the concept we adopt in this thesis.

Figure 3.1 shows a block diagram of the TFS. The BPM senses the beam displacement in horizontal and vertical direction by means of four plates. The signals of the BPM plates get merged by the combiner in order to get the beam displacement and the sum signal corresponding to the beam intensity. The role of the detector is to translate the BPM signal into the base-band. The heterodyne technique in telecommunications can be used in this part of the TFS [4]. Due to numerous advantages,e.g., reproducibility, programmability, easier and efficient integration, performance, and ability of more sophisticated processing, the signal processing part of the TFS is done nowadays only

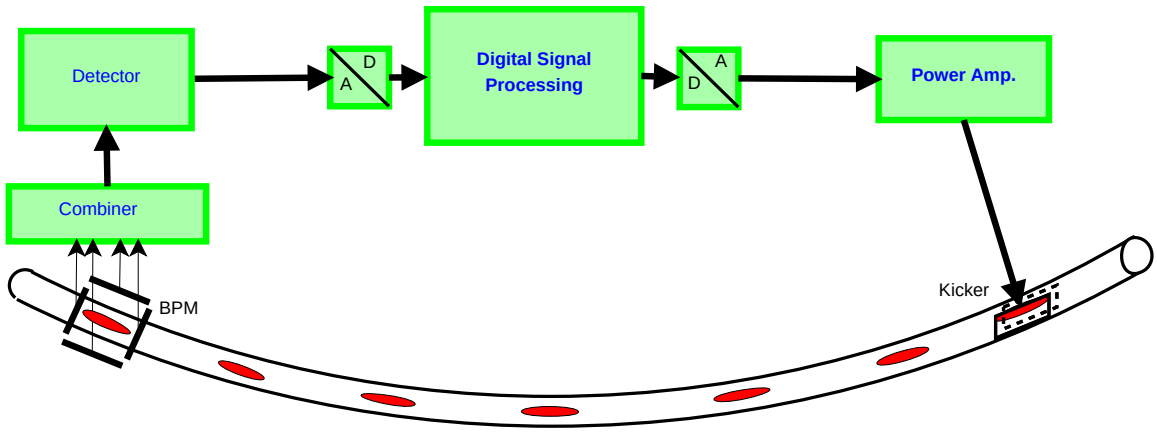

Figure 3.1. Block diagram of TFS.

in the digital domain using Digital Signal Processors (DSP) and/or FPGA. Therefore, converters from analog to digital and vice versa are required in the TFS. To close the feedback loop, the kicker equipped with a power amplifier is used to correct the beam position.

Since the beam oscillation motion has a sinusoidal form, the feedback correction signal applied by the kicker, i.e., actuator, corresponding to the derivative of the beam oscillation must have a 90° phase advance with respect to the betatron oscillation signal at the kicker position in order to have a damping impact. This can be achieved by passing the signal of one PU through a feedback filter, e.g., finite impulse response (FIR) filter with suitable phase response at the fractional tune frequency, with proper delay [4]. The number of the filter taps can be increased in order to have more degrees of freedom for optimizing the filter response, e.g., to have maximum flatness around the working point for robustness against tune changes [4,18], higher selectivity for better rejection of undesired frequency components [4], minimum amplitude response at specific frequencies that should not be fed back [19], stabilize different tune frequencies simultaneously [20]. Advanced concepts from the control theory have been applied also in the design of the feedback filter [21]. These approaches introduce however extra turns delay depending on how many taps the FIR filter consists of.

In [3], an approach was proposed to calculate the horizontal and vertical beam displacements at the position with 90° phase difference before the kicker using PUs located at two different positions along the accelerator ring for each of the horizontal and vertical directions. The reason for requiring PUs at two different positions for defining the beam trace space is that only beam displacements from the ideal trajectory can be measured by the PUs, but not the angles of the beam. Nevertheless, this approach does not consider the harmful noise at the PUs neither the robustness of the system

against unwanted deviations.

In general, the signals at the PUs are disturbed by noise. The Signal-to-Noise power Ratio (SNR) can be unacceptably low or not high enough. This is the case especially for lower currents where the beam is getting corrected by a big noise portion during the feedback. That will worsen the feedback correction quality as it leads to beam heating [13,14] and emittance blow up [4], as already mentioned in the previous chapter.

3.3 Using Multiple Pickups in TFS for Noise Power Minimization

In this section, we address a novel approach for mitigating noise at the PUs using more than two PUs at different positions to estimate the feedback correction signal for the kicker position, which has 90° phase difference from the betatron motion at this position. This is done by calculating a weighted sum of the PUs signals after proper synchronization [60, 61]. The idea here is to have more degrees of freedom using more PUs to adjust the sum weights such that the noise power contained in the estimated signal is minimized, while keeping a correct formula for calculating the beam displacement at the position with 90° phase advance before the kicker position in absence of PUs noise.

This is the Best Linear Unbiased Estimator (BLUE). Ideally, one would like to have the Minimum-Variance Unbiased Estimator (MVUE). The maximum likelihood estimator (MLE) is a well known preferable estimator in this sense due to its asymptotic optimality. This requires however the knowledge of the probability density of the noise. Furthermore, it leads to optimization problems that generally do not have analytical solutions, but must be solved iteratively. This is not really applicable for a TFS that needs calculations in real time. Also, in the special case of Gaussian noise with the linear model, the MLE becomes the same as the BLUE [62].

3.3.1 System Model

For each position along the synchrotron ring, three coordinate axes are defined, which determine the different possible beam displacements from the ideal trajectory. Figure 3.2 shows the transversal directions at some point along the accelerator ring: x-axis for horizontal displacement, and y-axis for vertical displacement. The longitudinal direction axis is marked by s.

The TFS is composed of multiple PUs located at different positions along the accelerator ring and one kicker for each transversal direction. The signals from the PUs, which correspond to the transversal beam displacement from the ideal trajectory, are delayed accordingly by $\tau_1, \tau_2, \ldots, \tau_M$, such that they correspond to the same bunch or slice of particles at every sample. The driving signal at the kicker is digitally filtered version of the weighted sum of the delayed signals. A block diagram of the TFS is shown in Figure 3.2.

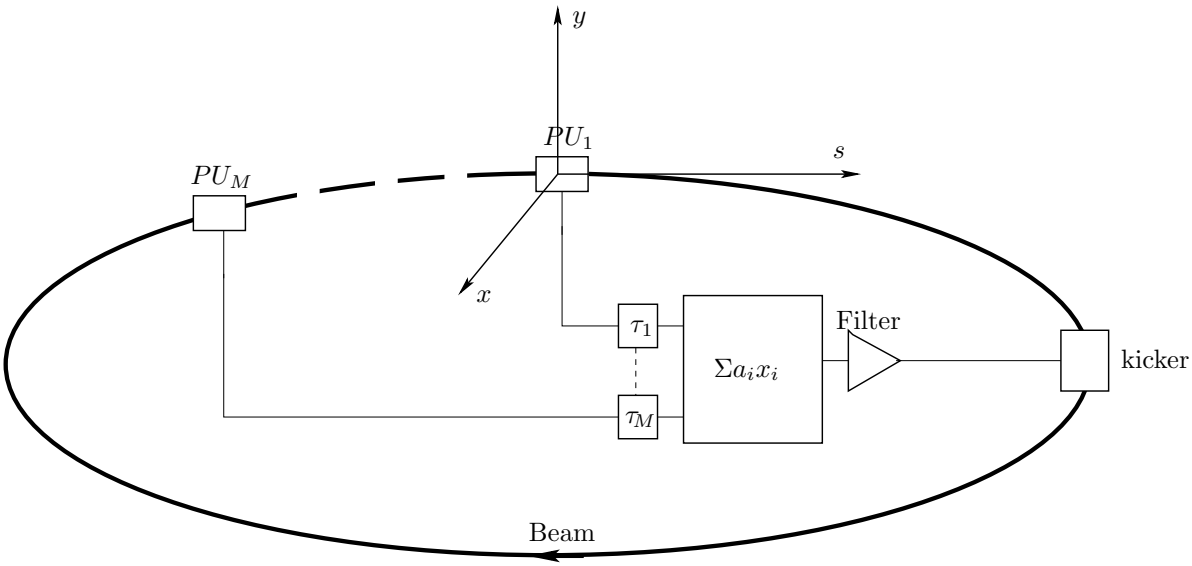

Figure 3.2. Block diagram of the TFS with multiple PUs.

We consider here the horizontal direction only and the vertical direction will have exactly the same formulae by substituting x with y. Let x_i be the signal at the pickup $\texttt{PU}_i$, which is located at the position s_i along the accelerator ring. This signal corresponds to the actual beam transversal displacement $\tilde{x}_i$ at the same position s_i perturbed by a noise term z_i, i.e.,

$$x_i = \tilde{x}_i + z_i. \tag{3.6}$$

In vector notation, one can write

$$\mathbf{x} = \tilde{\mathbf{x}} + \mathbf{z}, \tag{3.7}$$

where $\mathbf{x} = [x_1,\ x_2, \cdots, x_M]^T$ denotes the vector of signals for the M PUs, $\mathbf{z} = [z_1,\ z_2 \cdots, z_M]^T$ denotes the noise vector from the PUs with the covariance matrix for unbiased noise given by

$$\mathbf{R_{zz}} = \mathtt{E}\{\mathbf{z}\mathbf{z}^T\}. \tag{3.8}$$

In Equation (3.7), $\tilde{\mathbf{x}} = [\tilde{x}_1,\ \tilde{x}_2 \cdots\ , \tilde{x}_M]^T$ denotes the actual beam displacements vector at the PUs positions $s_1,\ s_2, \cdots, s_M$.

The noise part in the signal can be caused by different sources, e.g., thermal noise generated by the PUs electronics and disturbances from other devices. Thermal noise can be modeled as white noise spectrally shaped by the front-end electronics of each of the PUs. This noise part is basically uncorrelated between the signals from different PUs. The PUs can produce thermal noise powers different from each other when they are not similar, or placed in different environments, like in cryostat or room temperature. The disturbances at the PUs depend mainly on the locations of the PUs, and could be correlated between some neighbored PUs. This noise contribution could have narrow-band or wide-band spectral components, depending on the disturbers.

According to Equation (2.13) and Equation (2.14) the beam displacement at the position s_{k90} with 90° phase advance before the kicker position can be calculated using the beam status at the position of PU_i in the form

$$\begin{pmatrix} x(s_{k90}) \\ x'(s_{k90}) \end{pmatrix} = \begin{pmatrix} A_i & B_i \\ C_i & D_i \end{pmatrix} \cdot \begin{pmatrix} x(s_i) \\ x'(s_i) \end{pmatrix}. \tag{3.9}$$

Therefore, one can calculate x_{k90} using the beam displacements $\tilde{x}_{i_1}$ and $\tilde{x}_{i_2}$ at the positions s_{i_1} and s_{i_2} of PU_{i_1} and PU_{i_2}, where $i_1, i_2 \in \{1,\ 2, \cdots,\ M\}$, according to the vector summation approach introduced in [3] as

$$x(s_{k90}) = \alpha_{1,i_1,i_2}\tilde{x}_{i_1} + \alpha_{2,i_1,i_2}\tilde{x}_{i_2}, \tag{3.10}$$

where

$$\alpha_{1,i_1,i_2} = \frac{A_{i_1}B_{i_2}D_{i_1} - B_{i_1}C_{i_1}B_{i_2}}{B_{i_2}D_{i_1} - D_{i_2}B_{i_1}}, \tag{3.11}$$

and

$$\alpha_{2,i_1,i_2} = \frac{B_{i_1}C_{i_2}B_{i_2} - B_{i_1}D_{i_2}A_{i_2}}{B_{i_2}D_{i_1} - D_{i_2}B_{i_1}}. \tag{3.12}$$

Thus, the estimator of the feedback correction signal for the kicker position can be expressed by

$$\begin{aligned} \bar{x}_{i_1,i_2} &= \alpha_{1,i_1,i_2}x_{i_1} + \alpha_{2,i_1,i_2}x_{i_2} \\ &= \alpha_{1,i_1,i_2}\tilde{x}_{i_1} + \alpha_{2,i_1,i_2}\tilde{x}_{i_2} + \alpha_{1,i_1,i_2}z_{i_1} + \alpha_{2,i_1,i_2}z_{i_2} \\ &= x_{k90} + z_{i_1,i_2} \end{aligned} \tag{3.13}$$

where $x_{k90} = x(s_{k90})$ is the ideal feedback correction signal driving the kicker, α_{1,i_1,i_2} and α_{2,i_1,i_2} are constants, which depend on the lattice functions of the accelerator according to Courant-Snyder Ansatz [28, 36, 63]. In Equation (3.13), z_{i_1,i_2} denotes the noise part in the estimate of the feedback correction signal.

The noise-free signals at each PU for each bunch are sinusoidal with the fractional-tune frequency with different phases, considering a linear lattice. Therefore, the turn-wise weighted sum of these signals will give a sinusoidal signal with the same frequency, where the phase and amplitude are proportional to the summation weights. In practice however, only kicking on the second or a later turn is feasible. This kicking delay will only affect the required phase shift, and hence the weighting factors.

3.3.2 Optimal Linear Combiner

In order to mitigate the disturbing noise part in the estimation of the feedback correction signal at the kicker position, we address a new approach to calculating an optimally weighted sum of the signals from multiple PUs to be the feedback correction.

The idea of this approach is to filter out the noise from the PU signals by estimating the beam displacement at the position s_{k90} located 90° before the kicker as a weighted sum of the signals from M PUs, i.e., three or more. The weighting coefficients must be calculated in an optimal way such that the power of the noise part at the estimator output signal is minimized and the weighted sum of the actual beam displacement at the PUs positions without noise corresponds to the actual beam displacement at the position s_{k90}.

The optimization problem can be formulated as follows

$$[\hat{a}_1, \cdots, \hat{a}_M] = \underset{a_1,\cdots,a_M}{\operatorname{argmin}} \, \mathrm{E}\{|\sum_{i=1}^{M} a_i z_i|^2\} \tag{3.14a}$$

$$\texttt{s.t.} \qquad \sum_{i=1}^{M} a_i \tilde{x}_i(t) = x_{k90}(t), \;\; \forall t \in \mathbb{R}. \tag{3.14b}$$

This is a convex optimization problem and can be reformulated as

$$\mathbf{a}_{opt} = [\hat{a}_1, \cdots, \hat{a}_M]^T = \underset{\mathbf{a}}{\operatorname{argmin}} \, \mathbf{a}^T \mathbf{R}_{\mathbf{zz}} \mathbf{a} \tag{3.15a}$$

$$\texttt{s.t.} \quad \mathbf{a}^T\mathbf{b_r} = 1 \tag{3.15b}$$

$$\mathbf{a}^T\mathbf{b_i} = 0, \tag{3.15c}$$

where $\mathbf{b_r} \in \mathbb{R}^M$ and $\mathbf{b_i} \in \mathbb{R}^M$ are the real and imaginary parts of the phasors of the PU signals, respectively. The betatron oscillation at the position with 90° phase advance with respect to the kicker is considered here as a reference for the phasors.

Many iterative methods exist to solve such a convex optimization problem efficiently. However, a closed form solution would be more preferable since this solution will be applied on a later approach with exhaustive search nested iterations.

3.3.2.1 Analytical Solution

The Method of Lagrange Multipliers can be used to find an analytical solution for the optimization problem given in Equations (3.15). The Lagrange function of this problem is given as

$$\mathcal{L} = \mathbf{a}^T\mathbf{R_{zz}}\mathbf{a} + \lambda_r(\mathbf{a}^T\mathbf{b_r} - 1) + \lambda_i\mathbf{a}^T\mathbf{b_i}. \tag{3.16}$$

A solution can be found by solving the equation

$$\nabla_{\mathbf{a},\lambda_r,\lambda_i}\mathcal{L} = \mathbf{0}, \tag{3.17}$$

therefore,

$$2\mathbf{R_{zz}}\mathbf{a} = -\lambda_r\mathbf{b_r} - \lambda_i\mathbf{b_i} \tag{3.18}$$

$$\mathbf{a}^T\mathbf{b_r} = 1 \tag{3.19}$$

$$\mathbf{a}^T\mathbf{b_i} = 0. \tag{3.20}$$

From Equation (3.18), one finds

$$\mathbf{a} = -\frac{\lambda_r}{2}\mathbf{R_{zz}^{-1}}\mathbf{b_r} - \frac{\lambda_i}{2}\mathbf{R_{zz}^{-1}}\mathbf{b_i}, \tag{3.21}$$

substituting in Equation (3.19) and Equation (3.20) one finds out that

$$\lambda_r = \frac{-2\mathbf{b_i}^T\mathbf{R_{zz}^{-1}}\mathbf{b_i}}{\mathbf{b_i}^T\mathbf{R_{zz}^{-1}}\mathbf{b_i}\mathbf{b_r}^T\mathbf{R_{zz}^{-1}}\mathbf{b_r} - (\mathbf{b_r}^T\mathbf{R_{zz}^{-1}}\mathbf{b_i})^2} \tag{3.22}$$

$$\lambda_i = \frac{2\mathbf{b_r}^T\mathbf{R_{zz}^{-1}}\mathbf{b_i}}{\mathbf{b_i}^T\mathbf{R_{zz}^{-1}}\mathbf{b_i}\mathbf{b_r}^T\mathbf{R_{zz}^{-1}}\mathbf{b_r} - (\mathbf{b_r}^T\mathbf{R_{zz}^{-1}}\mathbf{b_i})^2} \tag{3.23}$$

Subsequently, the optimal weights $\mathbf{a}_{opt}$ can be found by substituting the values of λ_r and λ_i given in Equation (3.22) and Equation (3.23) into Equation (3.21) as

$$\mathbf{a}_{opt} = \frac{\mathbf{R_{zz}^{-1}}\mathbf{b_r}\mathbf{b_i}^T\mathbf{R_{zz}^{-1}}\mathbf{b_i} - \mathbf{R_{zz}^{-1}}\mathbf{b_i}\mathbf{b_r}^T\mathbf{R_{zz}^{-1}}\mathbf{b_i}}{\mathbf{b_i}^T\mathbf{R_{zz}^{-1}}\mathbf{b_i}\mathbf{b_r}^T\mathbf{R_{zz}^{-1}}\mathbf{b_r} - (\mathbf{b_r}^T\mathbf{R_{zz}^{-1}}\mathbf{b_i})^2}, \tag{3.24}$$

leading to the optimal noise power

$$P_{N\mathtt{min}} = \mathbf{a}_{opt}^T\mathbf{R_{zz}}\mathbf{a}_{opt}. \tag{3.25}$$

3.3.2.2 Alternative Solution

The optimization problem stated in Equation (3.14) can also be solved by reformulating it using vector summations of PU signals pairwise as follows: The beam displacement signal at the position s_{k90} with 90° phase advance with respect to the kicker position can be estimated according to the vector summation approach using any two of the M PU signals. Consider the consecutive signal pairs $\{x_1,\ x_2\}$, $\{x_2,\ x_3\}$, $\cdots$, $\{x_{M-1},\ x_M\}$, The estimates can be written in matrix notation as follows

$$\begin{pmatrix} \bar{x}_{1,2} \\ \bar{x}_{2,3} \\ \vdots \\ \bar{x}_{M-1,M} \end{pmatrix} = \mathbf{\Lambda} \begin{pmatrix} x_1 \\ x_2 \\ \vdots \\ x_M \end{pmatrix} \tag{3.26}$$

$$= \mathbf{\Lambda}\tilde{\mathbf{x}} + \mathbf{\Lambda}\mathbf{z} \tag{3.27}$$

$$= \begin{pmatrix} x_{k90} \\ \vdots \\ x_{k90} \end{pmatrix} + \mathbf{\Lambda}\mathbf{z} \tag{3.28}$$

where the matrix $\mathbf{\Lambda}$ is given via the vector summation of the above mentioned PU pairs by

$$\mathbf{\Lambda} = \begin{pmatrix} \alpha_{1,1,2} & \alpha_{2,1,2} & 0 & & \cdots & 0 \\ 0 & \alpha_{1,2,3} & \alpha_{2,2,3} & 0 & \cdots & 0 \\ 0 & 0 & \ddots & \ddots & 0 & \cdots \\ \vdots & \vdots & \cdots & 0 \ddots & \ddots & \cdots \\ 0 & \cdots & 0 & \cdots & \alpha_{1,M-1,M} & \alpha_{2,M-1,M} \end{pmatrix} \tag{3.29}$$

When the consecutive PUs of some pairs are located with betatron phase shift of $k\pi, \quad k \in \mathbb{Z}$, it is not possible to construct the vector summation. In this special case, the PUs must be reordered and $M-1$ independent pairs must be considered such that the vector summation can be achieved for all given new pairs, and the matrix $\mathbf{\Lambda}$ must be constructed accordingly.

Let $\mathbf{w} = [w_1,\ w_2, \cdots, w_{M-2},\ 1 - \sum_{i=1}^{M-2} w_i]^T$, then the following holds:

$$\mathbf{w}^T \begin{pmatrix} \bar{x}_{1,2} \\ \bar{x}_{2,3} \\ \vdots \\ \bar{x}_{M-1,M} \end{pmatrix} = x_{k90} + \mathbf{w}^T \mathbf{\Lambda} \mathbf{z} \quad \forall w_1, \cdots, w_{M-2} \in \mathbb{R}^{M-2} \tag{3.30}$$

The optimization problem given in Equation (3.14) is equivalent to finding the optimal vector $\mathbf{w}_{opt}$ which minimizes the power of the noise term in Equation (3.30), i.e., $\mathrm{E}|\mathbf{w}^T \mathbf{\Lambda} \mathbf{z}|^2$, where the optimal weights can be written as

$$\mathbf{a}_{opt}^T = \mathbf{w}_{opt}^T \mathbf{\Lambda}. \tag{3.31}$$

The reason for this equivalence is that both problems have the same number of dimensions, i.e., $N_D = M - 2$, in addition to describing the same unbiased estimator with minimized noise.

The vector $\mathbf{w}$ can be written in the following form

$$\mathbf{w} = \mathbf{D}\hat{\mathbf{w}} + \mathbf{e}_{M-1} \tag{3.32}$$

where

$$\hat{\mathbf{w}} = [w_1,\ w_2, \cdots\ , w_{M-2}]^T, \tag{3.33}$$

$$\mathbf{e}_{M-1} = [0,\ 0,\ \cdots,\ 0, 1]^T\ \in \mathbb{R}^{M-1}, \tag{3.34}$$

and $\mathbf{D} \in \mathbb{R}^{M-1 \times M-2}$ with all ones in the main diagonal, all -1 on the last row, and zeros elsewhere.

Therefore, the noise power is given by

$$\begin{aligned} P_N &= E|\mathbf{w}^T \mathbf{\Lambda z}|^2 \\ &= \hat{\mathbf{w}}^T \mathbf{D}^T \mathbf{\Lambda R_{zz}} \mathbf{\Lambda}^T \mathbf{D} \hat{\mathbf{w}} \\ &+ 2\hat{\mathbf{w}}^T \mathbf{D}^T \mathbf{\Lambda R_{zz}} \mathbf{\Lambda}^T \mathbf{e}_{M-1} \\ &+ \mathbf{e}_{M-1}^T \mathbf{\Lambda R_{zz}} \mathbf{\Lambda}^T \mathbf{e}_{M-1} \end{aligned} \tag{3.35}$$

An optimal solution $\hat{\mathbf{w}}_{opt}$ can be found by setting the derivative of P_N with respect to $\mathbf{w}$ to zero and solving, i.e.,

$$\left.\frac{\partial P_N}{\partial \hat{\mathbf{w}}}\right|_{\hat{\mathbf{w}}_{opt}} = 0 \tag{3.36}$$

for which the solution is found to be

$$\hat{\mathbf{w}}_{opt} = -(\mathbf{D}^T \mathbf{\Lambda R_{zz}} \mathbf{\Lambda}^T \mathbf{D})^{-1} \mathbf{D}^T \mathbf{\Lambda R_{zz}} \mathbf{\Lambda}^T \mathbf{e}_{M-1} \tag{3.37}$$

Finally, the optimal weights $\mathbf{a}_{opt}$ can be calculated using Equation (3.31) and Equation (3.37), i.e.,

$$\mathbf{a}_{opt} = (-\mathbf{D}(\mathbf{D}^T \mathbf{\Lambda R_{zz}} \mathbf{\Lambda}^T \mathbf{D})^{-1} \mathbf{D}^T \mathbf{\Lambda R_{zz}} \mathbf{\Lambda}^T \mathbf{e}_{M-1} + \mathbf{e}_{M-1})^T \mathbf{\Lambda}. \tag{3.38}$$

3.3.2.3 Example

In order to illustrate the equivalence between the solutions given in Equation (3.24) and Equation (3.38), we consider the following example:

Let the kicker be placed at a position with a phase of $-90°$. The phase reference of the betatron oscillation at the position with 90° phase advance with respect to the kicker has thus zero phase. Suppose we have $\mathtt{PU}_1$, $\mathtt{PU}_2$ and $\mathtt{PU}_3$ with the phases 120°, 180° and 240°, respectively, and the same β values as at the kicker position. Therefore, we have $\mathbf{b_r} = [-0.5, -1, -0.5]^T$ and $\mathbf{b_i} = [0.866, 0, -0.866]^T$. Assuming $\mathbf{R_{zz}} = \mathbf{I}_3$ to be the identity matrix of dimensions 3×3 for i.i.d. noise at the PUs, we find according to Equation (3.21) using the optimal values for λ_i and λ_r that the optimal weights are $\mathbf{a}_{opt} = [-0.333, -0.667, -0.333]$.

Taking the pairs $\{\mathtt{PU}_1,\ \mathtt{PU}_3\}$ and $\{\mathtt{PU}_3,\ \mathtt{PU}_2\}$, and according to Equation (3.29), we have

$$\mathbf{\Lambda} = \begin{pmatrix} -1 & -1 & 0 \\ 0 & 0 & -1 \end{pmatrix}.$$

Having $\mathbf{D} = [1, -1]^T$ and $\mathbf{e}_{M-1} = [0, 1]^T$, and applying Equation (3.38), we come up with the same weights as before.

3.4 Optimal Pickups-Kicker Placement for Noise Power Minimization

In the previous section, we introduced the optimal linear unbiased minimum variance estimator by using multiple PUs and one kicker for the TFS, where the positions $s_1, \cdots, s_M$ of the PUs and s_k of the kicker are fixed and known a priori. However, if the PUs and the kicker are placed in the accelerator without any further considerations, except for free space, the performance of the TFS might be limited or even poor, even when using an optimal approach for calculating the feedback correction signal based on the given combination of the PU signals. This can be the case, especially when the randomly chosen positions of the PUs and the kicker are close to the worst possible positions, or very far away from the ideal positions.

In this section, we address a new approach for finding the best positions to place the PUs and the kicker among all possible free locations around the accelerator ring, which are not occupied by other accelerator devices. The PUs and the kicker should be

placed such that the noise generated at the PUs causes the smallest disturbance to the feedback quality. As a metric for the noise disturbance, we use the SNR at the feedback correction signal estimate for the kicker position. The noise power is considered here at the output of the previously mentioned MVUE, which is the lowest possible noise power at the output of a linear unbiased estimator of the feedback correction signal for the given placement.

Since the beam displacement at the position with 90° betatron phase shift from the kicker position is the signal of interest for this approach, we take the squared value of the maximum possible amplitude at that position as a measure for the signal power. From the trace-space ellipse depicted in Figure 2.3, one can see that the maximum at a specific position s is given by

$$x_{k\ max}(s) = \sqrt{\beta(s)\epsilon}, \tag{3.39}$$

where ϵ is scaling factor, which is independent of the position s. Therefore, we take the signal power as

$$P_{Sig} = |x_{k\ max}(s)|^2 \sim \beta(s). \tag{3.40}$$

Hence, the SNR in one transversal (horizontal or vertical) direction for the given locations of the PUs and the kicker can be written as

$$\mathtt{SNR}_{x/y} = \frac{\beta_{x/y}(s_k)}{P_{N_{x/y}\mathtt{min}}(s_1,\ s_2, \cdots,\ s_M,\ s_k)}, \tag{3.41}$$

where the minimum noise power for a specific transversal direction $P_{N_{x/y}\mathtt{min}}$ is given in Equation (3.25). Thus, the SNR value depends on the betatron value $\beta_{x/y}(s_k)$ and $P_{N_{x/y}\mathtt{min}}(s_1,\ s_2, \cdots,\ s_M,\ s_k)$, which depend according to Equation (3.35) and Equation (3.37) on the noise covariance matrix $\mathbf{R_{zz}}$, and the parameters α_{ij} stated in Equation (3.29). These parameters again depend on the Twiss parameters for the PUs and kicker locations, and the phase differences between the PUs and the kicker. In summary, the SNR value depends on all of the Twiss parameters and phases for the PUs and kicker positions.

Since the PUs and the kicker are devices for both of the horizontal and vertical directions at once, the optimized SNR value should include the summation of the SNRs of both transversal directions, i.e.,

$$\mathtt{SNR} = \mathtt{SNR}_x + \mathtt{SNR}_y. \tag{3.42}$$

The optimal positions $[\hat{s}_1,\ \hat{s}_2, \cdots,\ \hat{s}_M,\ \hat{s}_k]$ of the PUs and the kicker can thus be calculated by

$$[\hat{s}_1,\ \hat{s}_2, \cdots,\ \hat{s}_M,\ \hat{s}_k] = \underset{s_1, s_2, \cdots, s_M, s_k}{\operatorname{argmax}}\ \mathtt{SNR} \tag{3.43a}$$

$$\mathtt{s.t.} \qquad [s_1, s_2, \cdots, s_M,\ s_k] \in \mathcal{F}^{M+1}, \tag{3.43b}$$

where $\mathcal{F}$ is the ensemble of unoccupied positions around the accelerator ring, where the PUs and the kicker can be placed at.

3.4.1 Changing Optics

The previous design technique requires the lattice functions to be constant during the acceleration cycle, i.e., constant focusing. However, the focusing can be changed during acceleration, e.g., from triplet mode to doublet mode as at the SIS 18 at the GSI in Darmstadt [3].

The quadrupole magnets of the SIS 18 are distributed around the accelerator ring in twelve segments. Each segment contains a triplet of quadrupoles. This constellation can provide low and smooth betatron function [34]. This increases the acceptance of the machine at the injection energy, which is important to cope with the injection errors.

Nevertheless, the beam extraction requires higher betatron values. This can be fulfilled using doublets of quadrupole magnets in the twelve segments of the accelerator ring [3, 34]. Therefore, the transition from the triplet optics at the injection energy to the doublet optics at the extraction energy level is passed continuously during the acceleration ramp.

For this variable focusing, an average value or a weighted average of the SNR, depending on the importance, can be maximized. In the case of smoothly changing focusing optics

like from triplet to doublet, the averaging of the SNR can be done via a cycle variable $\tau_{focusing}$, which defines for instance the strength of triplet operation at the SIS 18. $\tau_{focusing} = 0$ corresponds to doublet mode and $\tau_{focusing} = 1$ corresponds to triplet mode. Therefore, the optimal positions of the PUs and the kicker can be calculated for variable focusing by

$$\mathbf{s}_{opt} = \underset{\mathbf{s}}{\operatorname{argmax}} \int_0^1 w(\tau) SNR(\tau)\, \mathrm{d}\tau \tag{3.44a}$$

$$\mathtt{s.t.} \quad \mathbf{s} = [s_1,\ s_2, \cdots,\ s_M,\ s_k] \in \mathcal{F}^{M+1}, \tag{3.44b}$$

where $w(\tau)$ is a weighting function, which can be chosen constant for uniform averaging over an acceleration cycle.

3.5 Results

In this section, we show simulation results of the previously addressed approaches in this chapter for the heavy ions synchrotron SIS 18 at the GSI, which has a circumference of 216 m.

In the SIS 18, there are 12 PUs for the horizontal and the vertical directions, which are located periodically along the synchrotron ring. There is also one feedback kicker for both transversal directions. The phase difference between each two neighbouring pickups corresponds to the machine tune of every transversal direction divided by 12. For the horizontal direction, we have a phase difference of 129.3° between each two neighbouring pickups, and for the vertical direction 99.2°. During the acceleration, focusing changes continuously from the triplet mode to the doublet mode, which changes the betatron functions during each acceleration cycle, without changing the tune. The machine tunes for the horizontal and vertical directions are respectively $Q_x = 4.31$ and $Q_y = 3.31$.

The betatron functions $\beta_x(s)$ and $\beta_y(s)$ along the SIS 18 ring in the triplet and doublet modes are shown in Figure 3.3. The 12 periodical sections are clearly remarkable. Moreover, one can notice that the betatron function in the horizontal direction in the doublet mode has higher values than in the triplet mode. This is required for the extraction system [3, 34].

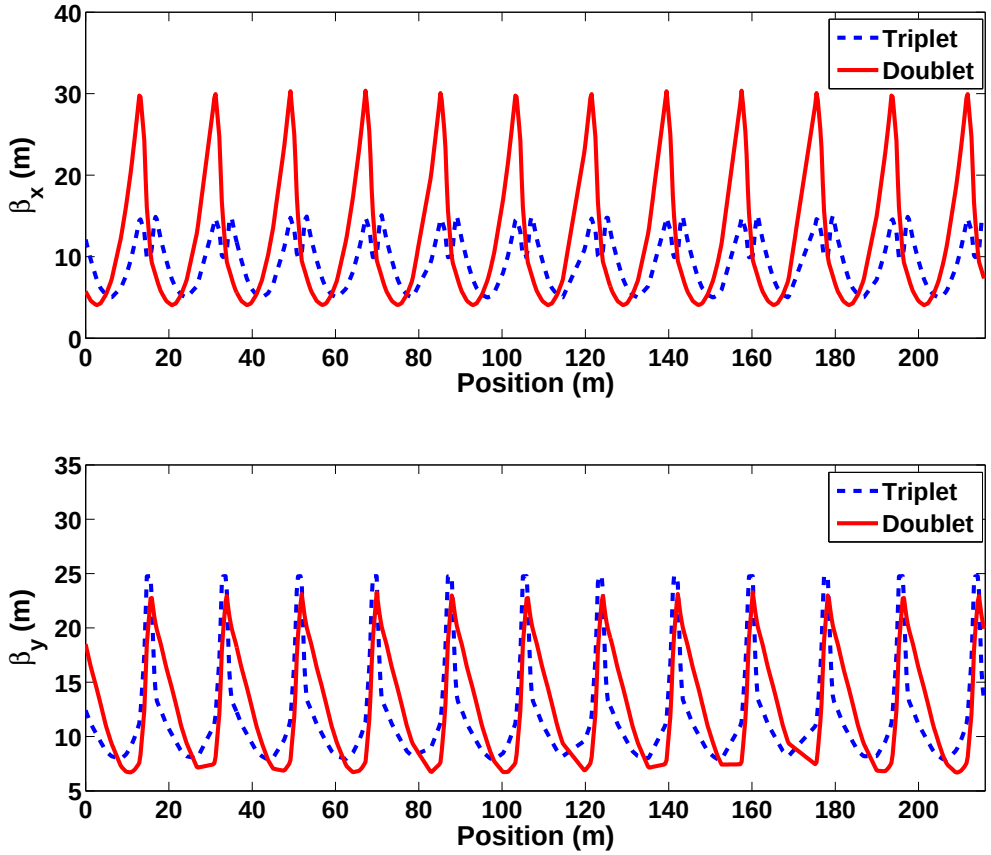

Figure 3.3. Betatron functions along the SIS 18 in the triplet and doublet modes.

Since the 12 PUs around the accelerator ring are identical, we used the same thermal noise power value at all of the PUs, i.e., σ^2, in the simulations. Furthermore, for good shielding no further disturbances were considered to affect the PU signals apart from the thermal noise. Therefore, the simulated noise is uncorrelated between all of the PUs, and with the same power. The covariance matrix of the noise is thus given by

$$\mathbf{R_{zz}} = \sigma^2 \mathbf{I}_{12}, \tag{3.45}$$

where $\mathbf{I}_{12}$ is the identity matrix of dimensions 12×12. This diagonal covariance matrix will not affect the generality of the simulated scenario.

At this point, it is important to mention that the choice of the value for the noise power σ^2 doesn't affect the results since we are interested in the relative noise power reduction achieved by our proposed approaches, and not the absolute noise power at the output of the feedback correction signal estimator. In our simulations, we used the value $\sigma = 1$.

The beam is usually traveling with almost the speed of light in todays particle accelerators, which is faster than the signal propagation in the cables of the TFS. In addition, digital processing delay is required to perform the calculations of the feedback signal. Thus, the correction kick corresponding to a given measurement is applied to the bunches one or more turns later [4]. For this reason, we consider as a demonstrating example the correction kicking on the second turn in all of the simulations. This one turn delay reveals that the machine tune plays a very important role in this context.

3.5.1 Optimal Linear Combiner

We applied the concept of the Optimal Linear Combiner for minimizing the noise power in the estimation of the feedback correction signal, i.e., the beam displacement at the position with 90° betatron phase advance from the kicker position of the TFS at the SIS 18.

The simulation results are shown for the horizontal and vertical directions in the triplet mode, i.e., directly after the injection, and the doublet mode, i.e., at the end of the acceleration cycle, directly before extracting the beam.

The technical parameters for these two directions in both modes are shown in Table 3.1. β_{pu} and α_{pu} are the values of the Twiss parameters at the PUs positions. β_k and α_k are the values of the Twiss parameters at the kicker position. $\Delta\phi_1^\circ$ denotes the phase difference between the kicker position and the position of the closest PU. $\mathbf{\Delta}\phi_{\mathtt{PUs}}^\circ$ denotes the phase difference between each two consecutive PUs.

Table 3.1. Technical parameters

mode	$\beta_{\mathbf{k}}$ (m)	$\beta_{\mathbf{pu}}$ (m)	$\alpha_{\mathbf{k}}$	$\alpha_{\mathbf{pu}}$	$\mathbf{\Delta}\phi_{\mathbf{1}}^\circ$	$\mathbf{\Delta}\phi_{\mathtt{PUs}}^\circ$
Doublet x	26.44	6.67	-2.22	0.67	105.7	129.3
Triplet x	14.06	12.67	-1.36	1.24	103.7	129.3
Doublet y	6.69	20.06	-0.54	1.04	74.5	99.2
Triplet y	10.25	13.41	-0.56	0.49	78.6	99.2

The tune phase for the corresponding direction must be added to this value for kicking on the second turn in our simulations.

The simulation results are depicted in Figure 3.4 and Figure 3.5 for the horizontal and vertical directions in each of the triplet and doublet modes, respectively. As a comparison reference, we consider here the noise power using the closest two PUs to

the kicker, which are the currently used PUs for the old TFS at the SIS 18. In each of these two figures, four curves are depicted, i.e. the noise power reduction by using an increasing number of closest PUs to the kicker and the noise power reduction by using the best combinations of an increasing number of PUs in both operation modes each. The noise power is calculated according to Equation (3.35), after replacing $\mathbf{w}$ with $\hat{\mathbf{w}}_{opt}$. The figures show that the noise power reduction is almost the same in the triplet and doublet modes for each direction. Furthermore, it can be seen from the figures that the noise power can be reduced by about 6 dB for the horizontal direction and about 3 dB for the vertical direction just by using the best combination of two PUs instead of the closest two PUs to the kicker. Moreover, one can notice from the figures that the noise power can be reduced by about 12 dB for the horizontal direction and about 8 dB for the vertical direction by using all the 12 PUs for the TFS in the SIS 18. One can interestingly notice from the figures that the curves for the doublet and the triplet modes are almost identical with the given parameters of the SIS 18. One important reason for that is the identical tune in both modes.

It is also interesting to notice that using more than the best 8 PUs doesn't achieve any noticeable enhancement in all cases. Furthermore, the enhancement by using the farthest PU is not remarkable. The best PU combinations in the case of the SIS 18 were different for the different working points during the acceleration cycle. This makes the realization of the TFS using the best combinations technically very challenging. However, this is easily applicable for synchrotrons with constant lattice functions during acceleration, like the case of the LHC at CERN.

The phase shifting is done in this approach by calculating a weighted sum of the PUs measurements. Therefore, the noise power at the output of this estimator depends on the summation weights. The weights depend on the positions of the PUs and the kicker, and the number of turns the kick is done after. In other words, they depend on the phase differences between the PUs and the kicking positions. For instance, for two PUs at positions with the same β values with one PU located 90° before the kicker and another PU located 360° from the first one, the weights will be 0.5 each. This leads to halving the noise power compared to using only one of these PUs. On the other hand, if the second PU is located 90° from the first one, the weights will be 1 and 0, respectively. This leads to no noise power enhancement compared to using only one PU. This shows that the noise reduction strongly depends on the PUs and kicker locations, and the noise power reduction ratio of $1/M$, with M is the number of PUs, holds only for special PUs-kicker constellations.

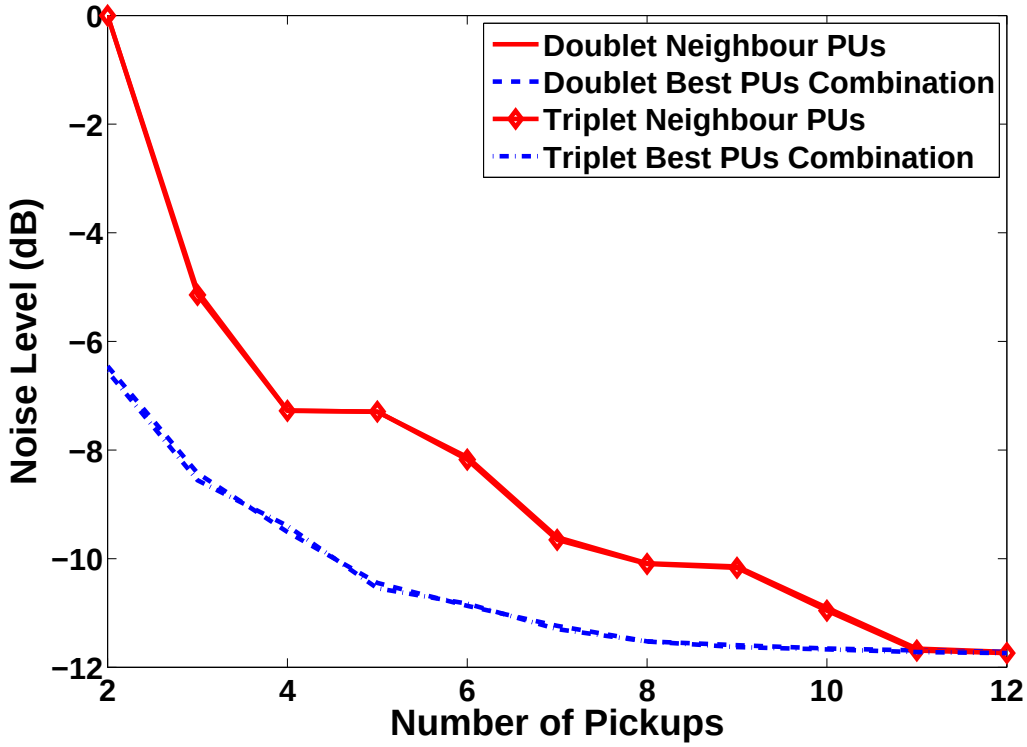

Figure 3.4. Noise reduction for the horizontal direction in the doublet and triplet modes at SIS 18.

3.5.1.1 Correlated Noise

In order to show the performance of our approach with correlated noise, we show in Figure 3.6 the noise power reduction compared to the previous case with uncorrelated noise at the PUs. We consider in this comparison the noise power reduction using an increasing number of closest PUs to the kicker and using the best combinations of an increasing number of PUs in both operation modes in the horizontal direction. In this simulation scenario, we assume disturbances on the PUs from the environment contributing to the PU noise with correlated part between each two neighbouring PUs with cross-correlation $C_{z_i z_{i+1}} = 0.3$. This leads to a noise covariance matrix $\mathbf{R_{zz}}$ with ones along the main diagonal, 0.3 along the diagonals above and below, and zeros elsewhere.

Figure 3.6 reveals that our approach exploits the noise correlation between the PUs in order to reduce its contribution in the estimation of the feedback correction signal. A noise power reduction of around 3dB can be achieved with the correlated noise by using more than three PUs. An enhancement of more than 1dB with the three closest

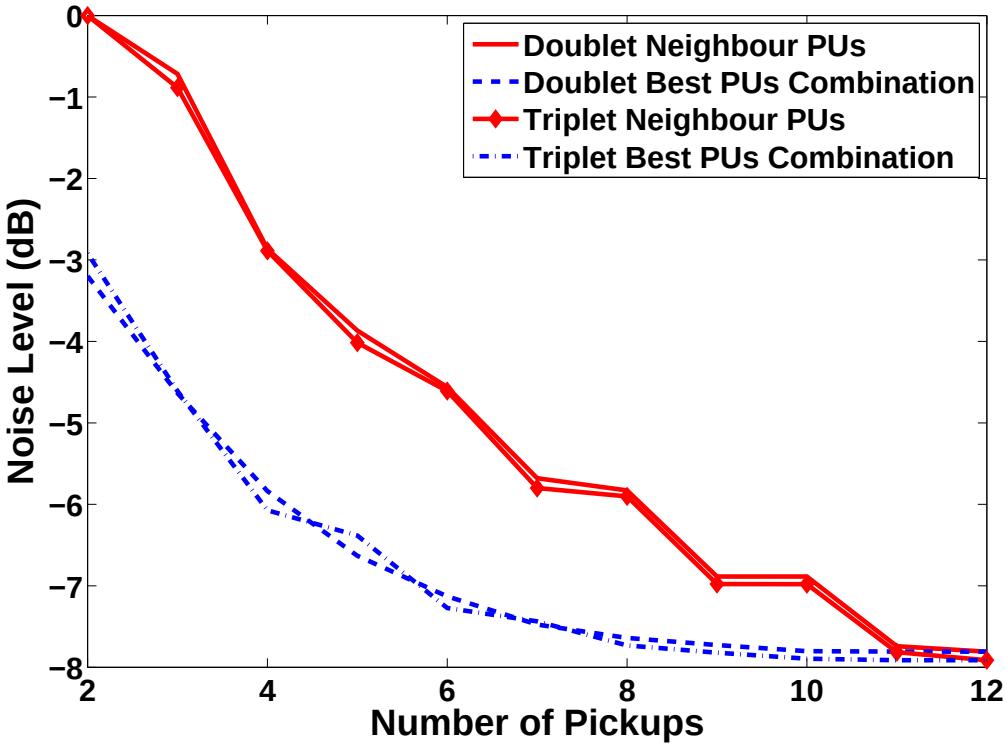

Figure 3.5. Noise reduction for the vertical direction in the doublet and triplet modes at SIS 18.

PUs to the kicker, and 2dB with the best two and three PU combinations is achieved by exploiting the noise correlation.

3.5.2 Optimal Pickups-Kicker Placement

We used the approach of optimal pickups-kicker placement to evaluate the goodness of the current positions of the PUs and the kicker for the TFS at the SIS 18. In order to do that, we used the optimization problem given in Equation (3.44) to find the best positions for the PUs and the kicker. Furthermore, we apply the same optimization problem, but replaced max with min, in order to find the worst positions for the PUs and the kicker.

Thus, comparing the overall SNR (the objective function of the optimization problem) of the current PUs and kicker positions with the ones of the worst and the best possible positions, gives a meaningful indication on how fortunate the current positions are for the TFS.

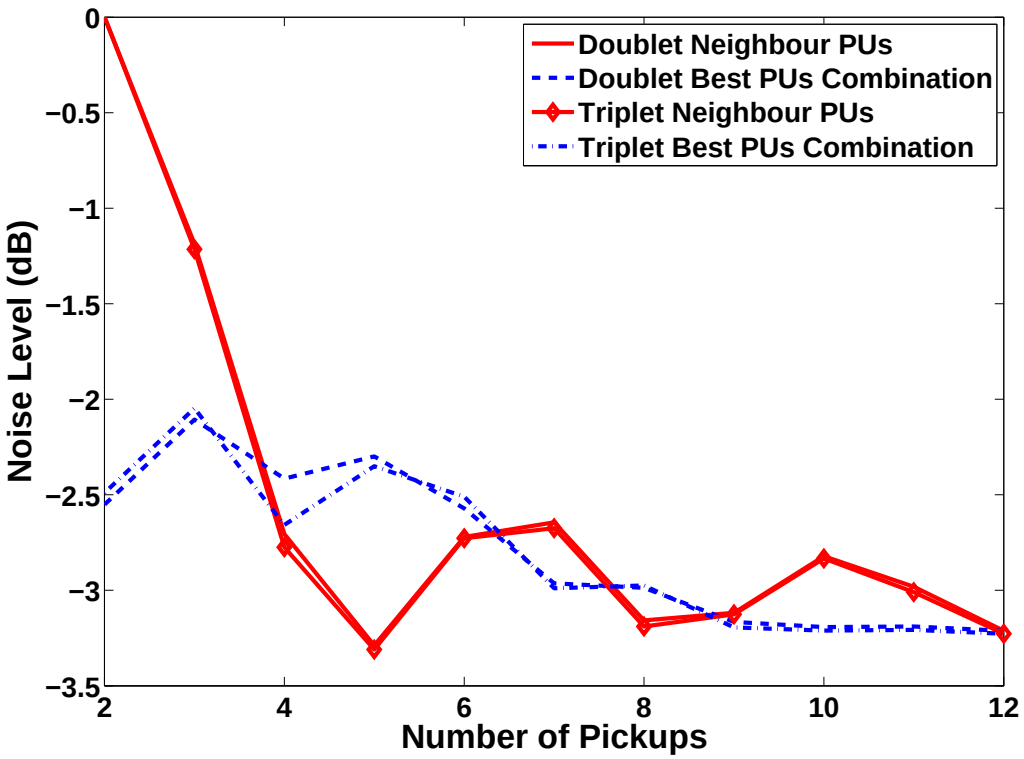

Figure 3.6. Noise reduction for the horizontal direction in the doublet and triplet modes with correlated PU noise compared to white noise at SIS 18.

The optimization problem in Equation (3.44) is multi-dimensional and non-convex in general. Since we cannot find an analytical solution to this problem, it be must be solved via an exhaustive search over all dimensions. In order to achieve the computation in a reasonable time, we have evaluated the positions of the kicker and only the three closest PUs.

Since the accelerator optics change from triplet to doublet mode, we average the SNRs over all possible optics values. That is, we average over the values $\tau_{focusing}$ from 0 to 1. We chose an integration step size of 0.1 for our simulation. The tune values for the horizontal and vertical directions are considered constant during acceleration cycle as mentioned before. The positions of three PUs and the kicker were sought independently along the accelerator ring in steps of 30 cm, and the SNR is calculated and compared for each constellation. Therefore, we have a 5 dimensional nested loop in this computation.

Figure 3.7 shows the overall SNRs in dB for the worst (red bar), current (black bar) and best (blue bar) PUs-kicker constellations. One can notice that the current PUs

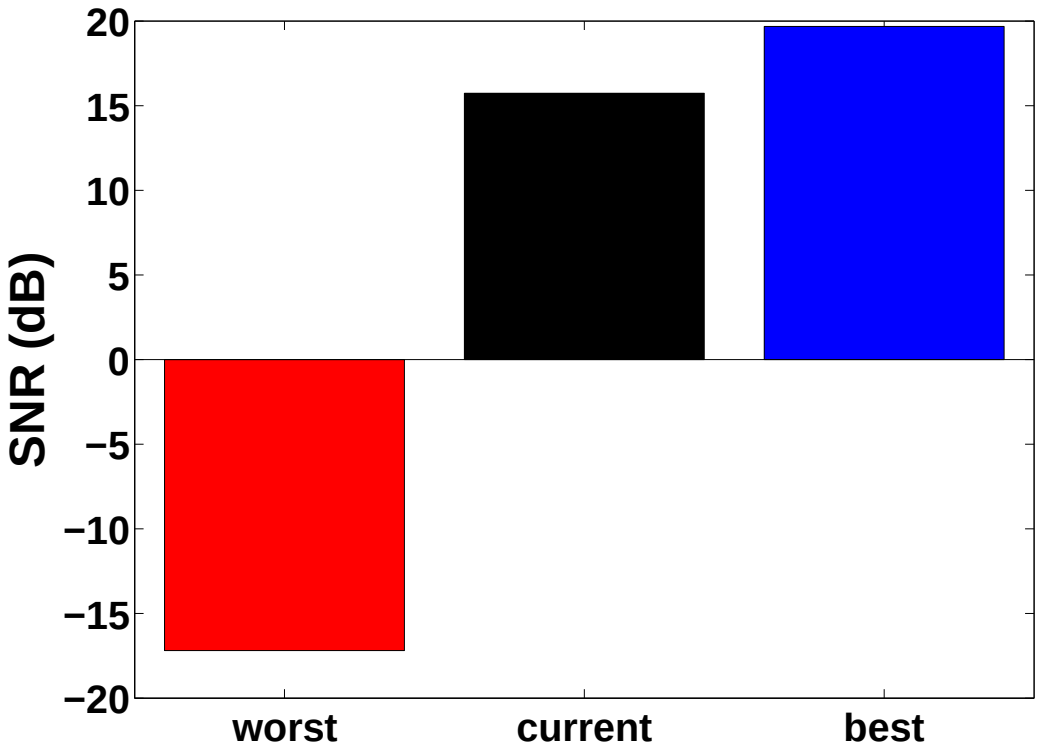

Figure 3.7. SNR comparison.

and the kicker positions obtain much better results (of about 32 dB) than the worst possible constellation. Nevertheless, it is not that close to the best constellation. An enhancement of about 4 dB in the SNR could be reached by shifting the PUs and the kicker toward optimal positions. The PUs and the kicker can be moved slightly from the optimal positions, if they are blocked by magnets or other accelerator components.

The positions of the PUs and the kicker in the three cases evaluated in Figure 3.7 are shown in Table 3.2.

Table 3.2. Pickups-Kicker Positions

	PU_1	PU_2	PU_3	Kicker
Best Position (m)	50.7	87.9	141.9	45.3
Current Position (m)	71.4	89.4	107.4	120.6
Worst Position (m)	45.9	46.2	46.5	62.1

Due to the periodicity in the SIS 18 optics, all the positions given in Table 3.2 can be shifted together in each row by an integer number of periods without affecting the SNR

value. A period of the SIS 18 has a length of a twelfth of the whole ring circumference, i.e., $L_P = 216/12 = 18$ m.

One can notice that the worst PU positions are stacked directly closed to each other, meaning that they own the same betatron phase. The worst kicker position in this case must be such that the betatron motion at the position located 90° before the kicker is almost orthogonal to the PUs signals after one turn delay.

This reveals that the phase of the locations is the most crucial parameter for optimal PUs-kicker placement. Nevertheless, the other Twiss parameters are also important for finding optimal PUs-kicker positions. Furthermore, the noise power and correlation of the PUs gets very important when the PUs have different noise characteristics.

Generally, the sensitivity of the SNR with respect to small shifts of the PUs and kicker positions depends strongly on how flat or how hilly the synchrotron optics parameters are. In other words, it depends on how fast or how slow the optics parameters, especially the phase, change around the optimal PUs and kicker positions. The more flat the SNR dependency on the PUs and kicker locations is, the more flexible is their placing on the optimal locations when theses locations are blocked by magnets or other accelerator components.

3.6 Implementation

The implementation of the TFS according to the previous concept using multiple PUs for minimizing the noise impact on the feedback quality is addressed in this section. The system implementation must be suitable for the currently existing heavy ions synchrotron SIS 18 and later the SIS 100 of the FAIR project at the GSI. Therefore, the implemented TFS must be highly configurable and modular to provide flexibility in the commissioning in both synchrotrons.

In order to fulfill the constraints at the currently existing SIS 18, the TFS must use the measurements of the existing BPMs there. The measured signals are acquired and digitized by certain acquisition devices called Libera Hadron. Since most of the computational resources of the FPGA on the Libera acquisition devices are already exploited for other beam diagnostics purposes, a distributed design of the TFS is adopted such that only a few system resources are required for the design extensions on the Libera

for the TFS. Thus, most of the functionality and data processing computation are performed on the central unit of the TFS, and the Libera devices are responsible for data collection and transfer to the central unit via the defined interface.

An ML605 board from the company Xilinx with a Virtex 6 FPGA possessing a lot of logic resources has been provided for the implementation of the central unit of the TFS to perform the intensive computation tasks in real time. This central unit collects data from Libera devices connected to the distributed BPMs around the accelerator ring and calculates the feedback correction signal driving the kicker via the power amplifiers. The ML605 FPGA board is depicted in Figure 3.8.

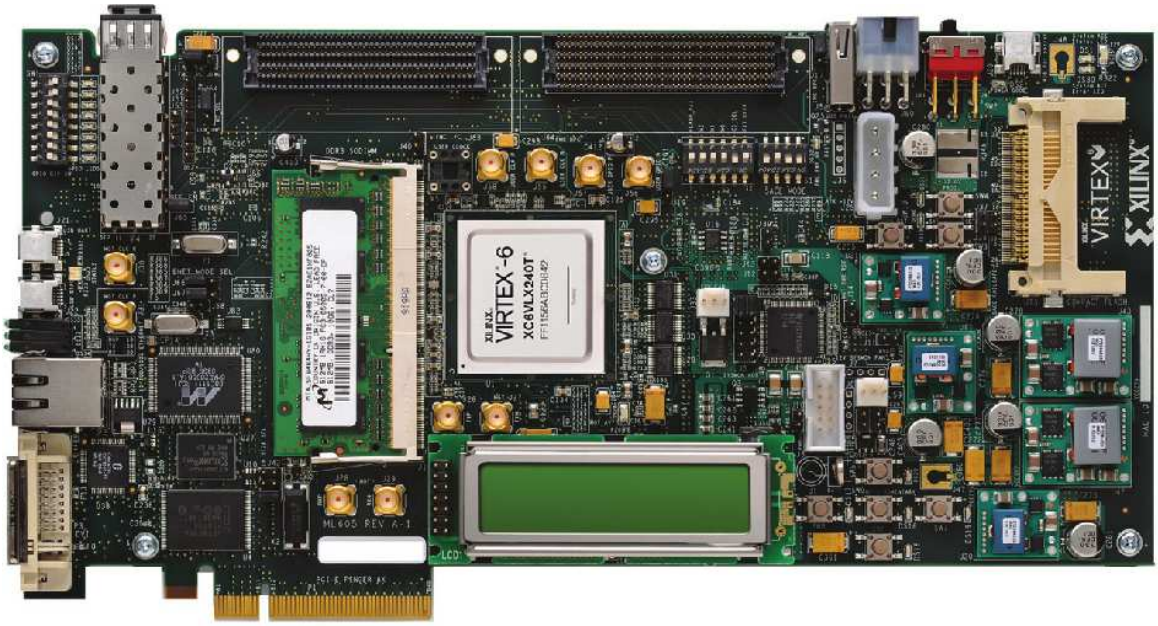

Figure 3.8. ML605 board [64].

The Libera devices are stacked together in racks in a room located about 200 m far from the room of the power amplifiers of the kicker. Therefore, we have decided to use an optical communication channel for the data transfer over this distance with high data rate. In order to reduce the cost of the system, we adopted an efficient implementation that uses less number of optical communication channels between the Libera devices and the central unit of the TFS. This is achieved by combining the data from a group of Libera devices into one channel forming a so called cluster. The data from each cluster gets collected at one Libera device to be the master of the cluster. The other parts of the cluster send their data packets to the master device to be forwarded to the TFS central unit. The master divides the channel time among all the cluster members evenly. This scheme does not introduce much extra delay since the Libera devices are very close to each other.

The possible number of Libera devices in a cluster depends on the speed of the optical channel and the data rate required by each device that depends on the required sampling rate for calculating the feedback correction signal, which depends on the bandwidth of the potential instabilities to be stabilized.

As a communication protocol between the TFS central unit and the masters of the Libera clusters as well as between the members of the clusters and their masters, we have used the Aurora core provided by Xilinx Core Generator, which uses the Multi-Gigabit Transceivers (MGT) built in the FPGA chip as channel lanes. All the clocking and reset logic required for the communication is generated within this core. Aurora is a scalable open protocol, lightweight, link-layer protocol that is used to move data across point-to-point serial links via a transparent interface to the physical layer, i.e., MGTs. It is a very efficient low-latency protocol that uses the least possible amount of logic while offering a rich, highly configurable feature set [65].

3.6.1 Data Transfer and Bandwidth

The Aurora communication module performs a basic error checking logic based on the 8B/10B block encoding. It checks if an incoming word at the receiver is conform with the codebook. This error checking feature introduces extra overhead in the channel usage. Therefore, the actual data transmission rate is 80% of the overall channel rate for the 8B/10B block encoding. In order to maintain a stable communication channel, the aurora protocol reinitialize the channel and reestablish the communication when a longer sequence of erroneous words has been received [65, 66].

For the communication channels between the Libera devices and the central unit of the TFS we operate the Aurora cores with a maximum speed of 2.5 Gbps. The actual data rate with this channel speed is due to the aforementioned overhead for error control 2 Gbps each. With a sampling rate at the Liberas of 25 Mega samples per second, the TFS is able to stabilize the frequency band up to 12.5 MHz. We have set the packet size for each channel to 32 bit. Therefore, the communication rate is 62.5 Mega packets per second. Within these packets the signal samples from the BPMs, the synchronization time stamps, as well as the control and addressing overhead are transmitted.

The Libera devices are equipped with Analog to Digital Converters (ADCs) that can provide a high precision and small quantization noise with 14 bits per sample. Every sample representing the beam position in the horizontal and vertical directions contains $2 * 14 = 28$ bits. A whole packet must be dedicated for such a sample together

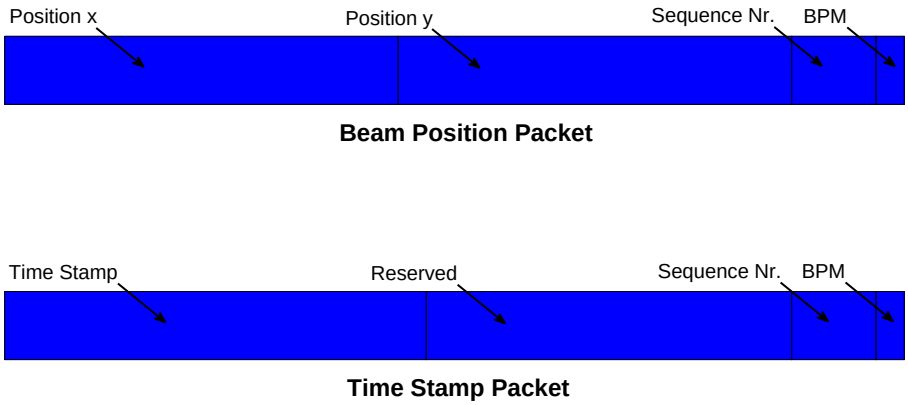

Figure 3.9. Packets structure.

with the corresponding sequence control and addressing overhead. Therefore, 25 Mega packets per second are required for the beam position data in the horizontal and vertical directions from each Libera device. Furthermore, the time stamps with 15 bits width are sent after every 4 position samples in a separate packet together with the sequence control and addressing overhead.

This means that the overall required packet rate fro every Libera device is $5/4 * 25 = 32.25$ Mega packets per second. Thus, the channel communication rate of 62.5 Mega packets per second is enough to serve two Libera devices. In other words, the number of Libera devices per cluster is 2 for the given sampling specifications. In our implementation for the SIS 18 at the GSI, two fiber optical cables have been laid to transfer the signal data from 4 BPMs around the synchrotron ring.

Figure 3.9 shows the packets structure for sending the beam position data at the BPMs and the time stamps. After every four position packets one time stamp packet is sent for each Libera device. The master of the cluster receives the data from the other member and forwards it to the TFS central unit. The last bit in the packets called BPM is dedicated to address between the master and the other member of the Libera clusters. The sequences of position and time stamp packets are marked with sequence numbers in order to make the data transfer scheme robust against lost packets.

3.6.2 Synchronization

In order to achieve the synchronization between the TFS central unit and the distributed Liberas, time stamps are transferred in addition to the position data from the

Liberas to the TFS central unit. These time stamps are calculated in terms of shared reference wave fronts among all the TFS nodes.

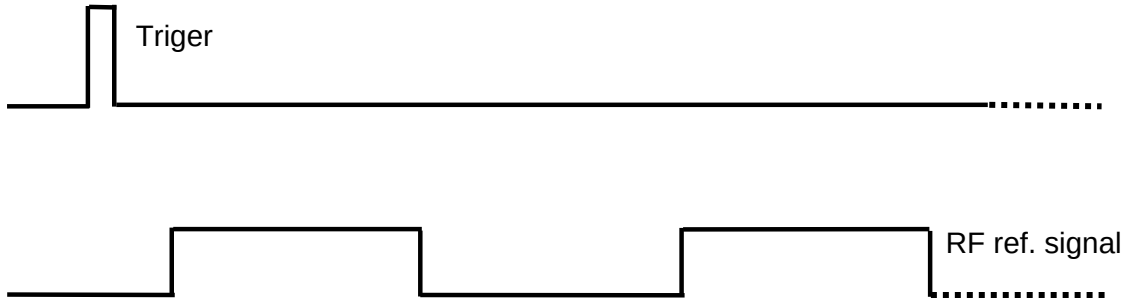

Figure 3.10. TFS synchronization signals.

Specifically, we use an RF signal from a wave generator as a shared reference in our design. In addition to the reference signal, a trigger signal is needed to indicate the start of counting the wave fronts of the reference signal. Figure 3.10 shows the scheme of the synchronization trigger and reference RF signals. A time stamp is composed of wave front number represented in 5 bits of the time stamp, and time shift from this wavefront represented in 10 bits of the time stamp.

3.6.3 System Overview

The TFS is composed of three main subsystems. The first part are the Libera devices for data acquisition of the beam position signals at the PUs. The second part of the TFS is the central unit, which collects the data from the distributed Libera devices, and synchronizes them. This central unit is also responsible for aggregating the PU signals and removing the revolution frequency harmonics by means of adaptive notch filter to calculate the feedback correction signal to be sent to the kicker via the Digital to Analog Converter (DAC). The kicker and its electronics are the third part of the TFS, which is the actuator that closes the feedback loop on the beam.

The important parameters for the feedback, i.e., the revolution frequency and linear combination factors, are delivered to the TFS from the particle accelerator central control via function generators and interface cards. The system configuration is done by an external computer via ethernet connection. Figure 3.11 shows the hardware electronics of the TFS central unit implementation.

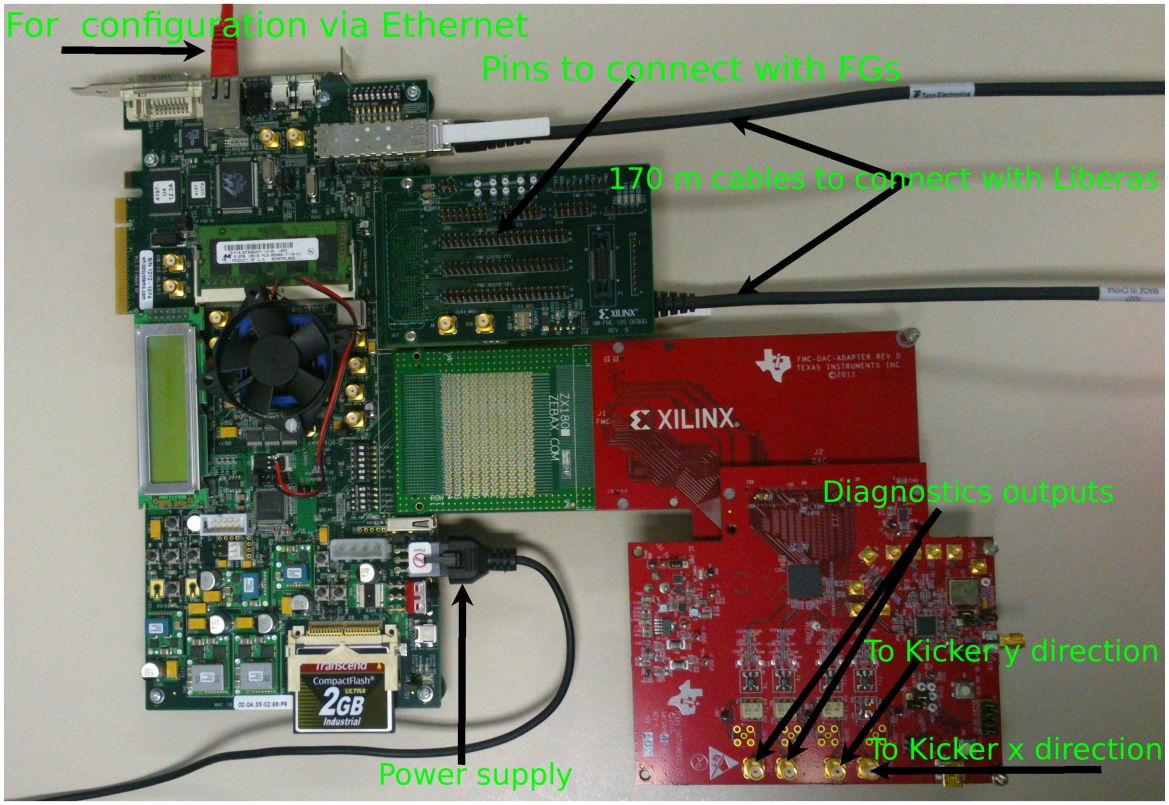

Figure 3.11. TFS central unit hardware overview.

Chapter 4

Transverse Feedback System and Optics Uncertainties

The correction signal of transverse feedback system is usually calculated according to the transfer matrices between the pickups and the kickers. However, errors due to magnetic field imperfections and magnets misalignment lead to deviations in the transfer matrices from their nominal values. Therefore, using the nominal values of the transfer optics with uncertainties leads to feedback quality degradation, and thus beam disturbances.

In this chapter, we address a novel concept for robust feedback system against optics errors or uncertainties. A kicker and multiple pickups are assumed to be used for each transversal direction. We introduce perturbation terms to the transfer matrices between the kicker and the pickups. Subsequently, the Extended Kalman Filter is used to estimate the feedback signal and the perturbation terms using the measurements from the pickups. We assume here that the optics parameters do not change fast such that they stay almost constant over a few turns in order to have enough measurements for the given parameters to be identifiable.

Moreover, we propose a method for measuring the phase advances and amplitude scaling between the positions of the kicker and the BPMs. Directly after applying a kick on the beam by means of the kicker, we record the BPM signals. Consequently, we use the Second-Order Blind Identification (SOBI) algorithm to decompose the recorded noisy signals into independent sources mixture [5,6]. Finally, we determine the required optics parameters by identifying and analyzing the betatron oscillation sourced from the kick based on its mixing and temporal patterns. Results for the heavy ions synchrotron SIS 18 at the GSI are shown the end of this chapter. This approach can be applied as an alternative to the previous approach such that the updated measured parameters can be used in a simple (non-robust) feedback system. The updated measured parameters can of course still be used with a robust feedback system.

4.1 Motivation

Two or more PUs can be used to calculate the feedback correction signal for driving the kicker of the TFS without using an FIR filter in order to avoid extra turns delay,

as already discussed in the previous chapter. At least two PUs at different positions are required for defining the beam trace space since only beam displacements from the ideal trajectory can be measured by the PUs, but not the angles of the beam [3]. Multiple optimally placed PUs can be used to minimize the noise contribution in the feedback correction signal, as we proposed in the previous chapter. This enhances the feedback quality and reduces beam heating by the TFS noise [60, 61].

The proper coefficients of the FIR filter as well as the combination coefficients of multiple PU signals for calculating the feedback correction signal of the TFS are calculated based on the accelerator optics parameters, i.e., the transfer matrices between the kicker and the PUs [4, 60, 61]. Therefore, any deviations in the optics parameters from their known nominal values due to magnetic field imperfections, magnets misalignment, and the aging of the magnets lead to disturbances in the calculated feedback correction signal, and thus feedback quality deterioration when using the nominal optics values. Consequently, the beam will be disturbed and its quality get worse.

In order to cope with this problematic, a novel concept for robust feedback system against optics errors or uncertainties is addressed in this chapter. Furthermore, a method for precise measurement of the optics transfer between the kicker and the PUs to get the actual values and reach better feedback quality is presented as an alternative or a complement of the TFS robustification concept.

4.2 Robust TFS

A feedback system that uses one kicker and multiple pickups for each transversal direction is assumed. We introduce perturbation terms to the transfer matrices between the PUs and the kicker for each of the beam oscillation transversal directions. Subsequently, the Extended Kalman Filter is employed to estimate the feedback correction signal as well as the perturbation terms by means of the measured data from the distributed PUs [67].

We address a bunch-by-bunch feedback system, which deals with the signals of different bunches as parallel channels. The signals from the PUs, which correspond to the transversal beam displacements, are delayed accordingly, such that they correspond to the same bunch in every time sample. The delay terms are fixed portions of the revolution time that usually gets estimated online, e.g., via the Schottky spectrum, with enough accuracy for the required bandwidth of the TFS. Therefore, we do not consider the robustification of the TFS against the uncertainties in these delay terms.

The driving signal at the kicker is the output of the digital processing of the delayed PUs signals. As we already mentioned in the previous chapter, the driving signal of the kicker, i.e., the feedback correction signal, must be an estimation of the beam displacement at the position s_{k90} with 90° phase advance before the kicker location. The block diagram of the TFS model is depicted in Figure 3.2.

4.2.1 System Model

Let $\tilde{\mathbf{x}}(n) = [\tilde{x}_1(n), \cdots, \ \tilde{x}_M(n)]^T$ be the vector of the beam positions (horizontal or vertical) at the M PUs at the n^{th} turn for one of the bunches. Therefore, the measurement vector $\mathbf{x}(n)$ will be, like in the previous chapter, this positions vector distorted by the noise vector $\mathbf{z}(n) = [z_1(n), \cdots, \ z_M(n)]^T \sim N(\mathbf{0}, \ \mathbf{R_{zz}})$ of the PUs. This can be written as

$$\mathbf{x}(n) = \tilde{\mathbf{x}}(n) + \mathbf{z}(n). \tag{4.1}$$

According to Equation (2.13) the beam displacement x and angle x' can be calculated at any position around the accelerator ring by knowing them at some specific position via a transfer matrix dependency. Therefore, we define

$$\mathbf{x_K}(n) = [x_K(n), \ x'_K(n)]^T \tag{4.2}$$

to be the beam status vector at the n^{th} turn, where $x_K(n)$ is the beam position at the kicker location, and $x'_K(n)$ is the beam angle at this place.

The beam status vector at turn $n+1$ can be found in dependence of the beam status vector at turn n according to the accelerator optics model. It will be the multiplication of the complete turn transfer matrix $\mathbf{M_{KK}}(n)$ by the kicked beam status vector at turn n superposed with the kick. Furthermore, small disturbances are added to this model. Thus,

$$\mathbf{x_K}(n+1) = \mathbf{M_{KK}}(n) \cdot \mathbf{x_K}(n) + \mathbf{D_K}(n+1) + \mathbf{n_p}(n+1), \tag{4.3}$$

where

$$\mathbf{D_K}(n+1) = [0, \ \Delta x'_{DK}(n+1)]^T, \tag{4.4}$$

is the kick applied on the beam by the kicker at turn n, and $\mathbf{n_p}(n) = [n_{p1}(n), \ n_{p2}(n)]^T \sim N(\mathbf{0}, \ \mathbf{R_{nn}})$ denotes the disturbances in the beam position and angle due to the model uncertainties, non-linear errors in the lattice of the synchrotron, and external interfering sources.

The measurement vector $\mathbf{x}(n)$ in Equation (4.1) can be written in dependence of the beam status vector at the n^{th} turn as follows

$$\mathbf{x}(n) = \mathbf{M_{MS}}(n) \cdot \mathbf{x_K}(n) + \mathbf{z}(n), \tag{4.5}$$

where the measurement matrix $\mathbf{M_{MS}}(n)$ is given by

$$\mathbf{M_{MS}}(n) = \mathbf{I}_M \otimes [1,\ 0] \cdot \begin{bmatrix} \mathbf{M_{PK1}}(n) \\ \vdots \\ \mathbf{M_{PKM}}(n) \end{bmatrix}, \tag{4.6}$$

where $\mathbf{I}_M$ denotes the identity matrix of dimension M, and $\mathbf{M_{PK1}}(n), \cdots, \mathbf{M_{PKM}}(n)$ denote the transfer matrices given in Equation (2.14) from the kicker to the M PUs respectively. The phase differences in the formulas of the transfer matrices must be plugged in accordingly by adding multiples of the tune when kicking after some turns delay after the measured samples. The model of beam status propagation is depicted in Figure 4.1.

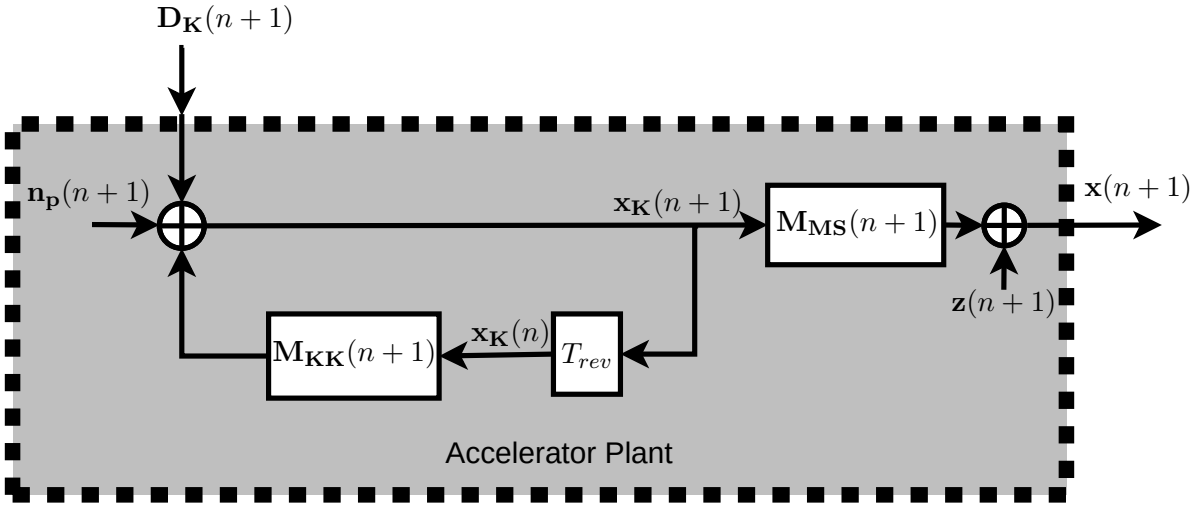

Figure 4.1. Beam status propagation model in synchrotron.

If the accelerator optics are known for every turn, the transfer matrix $\mathbf{M_{KK}}(n)$ and the measurement matrix $\mathbf{M_{MS}}(n)$ will be known exactly. Since the kick in Equation (4.4) is the output of the TFS, and therefore known, the beam status vector $\mathbf{x_K}(n)$ is the only unknown to be estimated for complete identification of the system. Therefore, the Kalman Filter will be the optimal estimator of the beam status vector under the assumption of Gaussian noises, since the system dynamic model in Equation (4.3) and the measurement model in Equation (4.5) are linear.

The Kalman Filter is an estimator for the so called linear-quadratic problem, which is the problem of estimating the instantaneous state of a linear dynamic system perturbed by Gaussian noise using measurements that are linearly related to the state but

corrupted by noise. The resulting estimator is statistically optimal with respect to any quadratic function of estimation error [68, 69].

However, deviations in the optics from the nominal values driven by the accelerator control exist always due to many reasons as mentioned before. This leads to the fact that the complete turn transfer matrix and the measurement matrix are not known exactly. Therefore, complete system identification for more precise estimation of the beam status vector and more efficient feedback process requires the estimation of these matrices as well.

4.2.2 Robustification

In our approach for robust TFS against lattice uncertainties, we consider the matrices as superposition of known parts, which are the nominal values provided by the accelerator control, and unkown parts to be estimated, i.e.,

$$\mathbf{M_{KK}}(n) = \mathbf{M^{nom}_{KK}}(n) + \mathbf{M^{P}_{KK}}(n), \tag{4.7}$$

$$\mathbf{M_{MS}}(n) = \mathbf{M^{nom}_{MS}}(n) + \mathbf{M^{P}_{MS}}(n), \tag{4.8}$$

where $\mathbf{M^{nom}_{KK}}(n)$ and $\mathbf{M^{nom}_{MS}}(n)$ contain the nominal values. $\mathbf{M^{P}_{KK}}(n)$ and $\mathbf{M^{P}_{MS}}(n)$ denote the uncertainty matrices that we considered as a part of the system status variables, which must be estimated. Therefore, the extended system status vector can be written like

$$\mathbf{X}_{Ex}(n) = [\mathbf{x_K}(n)^T,\ Vec(\mathbf{M^{P}_{KK}}(n))^T,\ Vec(\mathbf{M^{P}_{MS}}(n))^T]^T, \tag{4.9}$$

where $Vec(\cdot)$ denotes the vectorization operator of a matrix, which stacks the columns of the matrix into a vector.

The evolution of the system state vector can thus be stated according to a nonlinear function, i.e.,

$$\mathbf{X}_{Ex}(n+1) = f_{\mathbf{D_K}(n+1)}(\mathbf{X}_{Ex}(n)) + \mathbf{N_P}, \tag{4.10}$$

where

$$f_{\mathbf{D_K}(n+1)}(\mathbf{X}_{Ex}(n)) = f(\mathbf{X}_{Ex}(n)) + [\mathbf{D_K}(n+1)^T,\ 0, \cdots,\ 0]^T. \tag{4.11}$$

The beam status propagates like in Equation (4.3), and the uncertainty matrices propagate unchanged, i.e.,

$$f\begin{pmatrix} \mathbf{x_K}(n) \\ Vec(\mathbf{M^{P}_{KK}}(n)) \\ Vec(\mathbf{M^{P}_{MS}}(n) \end{pmatrix} = \begin{pmatrix} (\mathbf{M^{nom}_{KK}}(n) + \mathbf{M^{P}_{KK}}(n))\mathbf{x_K}(n) \\ Vec(\mathbf{M^{P}_{KK}}(n)) \\ Vec(\mathbf{M^{P}_{MS}}(n) \end{pmatrix}. \tag{4.12}$$

The measurement model can be formulated as

$$\mathbf{x}(n) = h(\mathbf{X}_{Ex}(n)) + \mathbf{z}(n), \tag{4.13}$$

where

$$h(\mathbf{X}_{Ex}(n)) = (\mathbf{M}^{\mathbf{nom}}_{\mathbf{MS}}(n) + \mathbf{M}^{\mathbf{P}}_{\mathbf{MS}}(n)) \cdot \mathbf{x}_{\mathbf{K}}(n). \tag{4.14}$$

The TFS must implement an observer of the system parameters jointly based on the measured data at the PUs. The beam correction signal will be the estimated beam displacement with 90° phase advance. The model of the extended beam status propagation with the observer for the TFS $f_{\mathbf{M}^{\mathbf{nom}}_{\mathbf{KK}},\mathbf{M}^{\mathbf{nom}}_{\mathbf{MS}}}(\cdot)$ is depicted in Figure 4.2.

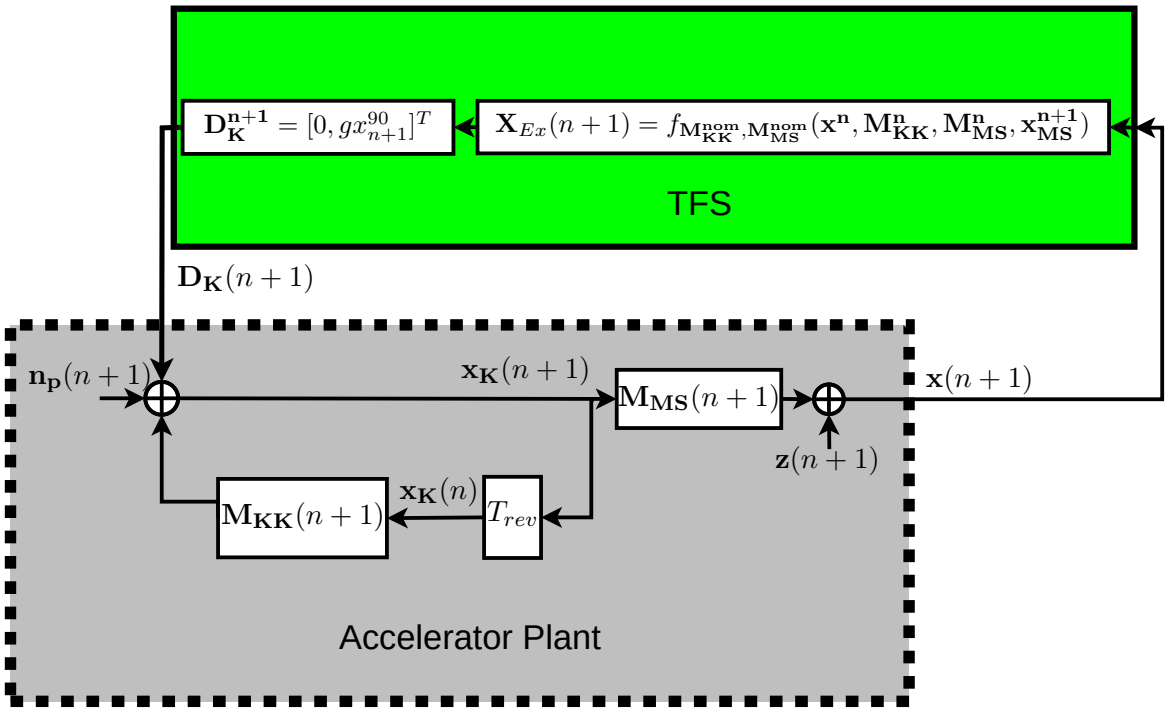

Figure 4.2. Extended status vector propagation model in synchrotron and TFS observer.

4.2.3 Observability

Before we start with the design of the observer for the TFS, we first study the observability of the system model stated in Equation (4.10) and Equation (4.13).

Define

$$\Theta = \{h(f_{\mathbf{D_K}(j)} \circ \cdots \circ f_{\mathbf{D_K}(1)}(\cdot)) \mid \forall j \geq 0\}. \tag{4.15}$$

In [70], it has been proven that the criterion for the system to be locally observable around $\mathbf{X}_{Ex}(0)$ is that

$$dim\left(\left.\frac{\partial\Theta(\mathbf{X}_{Ex})}{\partial\mathbf{X}_{Ex}}\right|_{\mathbf{X}_{Ex}(0)}\right) = n, \tag{4.16}$$

where $n = dim(\mathbf{X}_{Ex})$, i.e., the number of extended system status parameters.

For constant optics and errors over the time, and therefore constant complete turn transfer matrix and measurement matrix, we show in the following how to check whether the observability of the whole system is given according to the aforementioned criterion.

Usually, even when the accelerator lattice functions change during the acceleration cycle like the case of SIS 18 at the GSI, the changing rate of the accelerator optics is much slower than the beam revolution frequency in the accelerator ring. Therefore, the accelerator optics can be considered constant during a small number of beam revolutions. Thus, it is sufficient to show that the observability criterion is fulfilled for constant accelerator optics over a few number of beam turns.

In order to verify the observability condition in Equation (4.16), we first calculate and stack the Jacobian matrices in $\mathbf{J}_{\Theta}(\mathbf{X}_{Ex}(0))$ for some set of

$$\Theta_j(\mathbf{X}_{Ex}(0)) = h(f_{\mathbf{D_K}(j)} \circ \cdots \circ f_{\mathbf{D_K}(1)}(\mathbf{X}_{Ex}(0))), \ \texttt{with}\ j \in \{1,\ 2, \cdots,\ L\}, \tag{4.17}$$

where

$$L = \left\lceil \frac{n}{M} \right\rceil. \tag{4.18}$$

M denotes the number of the measurements per turn, i.e., number of the PUs. The Jacobian matrices are defined as

$$\mathbf{J}_{\Theta_j}\left(\mathbf{X}_{Ex}(0)\right) = \left.\frac{\partial\Theta_j(\mathbf{X}_{Ex})}{\partial\mathbf{X}_{Ex}}\right|_{\mathbf{X}_{Ex}(0)}. \tag{4.19}$$

Secondly, we calculate the rank of $\mathbf{J}_{\Theta}(\mathbf{X}_{Ex}(0))$. If $rank(\mathbf{J}_{\Theta}(\mathbf{X}_{Ex}(0))) = n$, then the system is locally observable around $\mathbf{X}_{Ex}(0)$, otherwise we extend the matrix $\mathbf{J}_{\Theta}(\mathbf{X}_{Ex}(0))$ by taking bigger number of turns than L. If the rank stays less than the number of extended model parameters in spite of the extensions of the Jacobian matrices, the system is considered unobservable.

Assuming small deviations in the transfer matrices from their nominal values given by the accelerator, it is enough to show that the criterion of the system observability is fulfilled around the zero perturbations of the whole turn matrix $\mathbf{M_{KK}}(n)$ and the

measurement matrix $\mathbf{M_{MS}}(n)$, i.e., around the nominal values with $\mathbf{M^P_{KK}}(0) = \mathbf{0}_{2\times2}$ and $\mathbf{M^P_{MS}}(0) = \mathbf{0}_{M\times2}$, for all possible values of the initial beam status vector $\mathbf{x_K}(0)$ defined in Equation (4.2).

Thus, the observability criterion has to be fulfilled according to Equation (4.16) around all possible values of the status parameters vector of the form

$$\mathbf{X}_{Ex}(0) = \left[\mathbf{x_K}(0)^T,\ Vec(\mathbf{0}_{2\times2})^T,\ Vec(\mathbf{0}_{M\times2})^T\right]^T, \tag{4.20}$$

where we consider the observability of the matrices around their nominal values as mentioned before. $\mathbf{x_K}(0)$ must be swept such that all possible beam displacements and directions are covered, i.e., the rank of the stacked Jacobian matrices over some turns is considered concerning all possible beam initial conditions.

According to Equation (4.11), Equation (4.14), and Equation (4.15), the possible elements of Θ can only have the form

$$\Theta = \left\{ \mathbf{M_{MS}}(j) \left[\prod_{i=1}^{j} \left(\mathbf{M_{KK}}(i)\right) \mathbf{x_K}(0) + \sum_{i=0}^{j} \left(\prod_{k=i+1}^{j} \left(\mathbf{M_{KK}}(k)\right) \mathbf{D_K}(i) \right) \right] \ \middle|\ \forall j \geq 0 \right\}, \tag{4.21}$$

where the measurement matrix $\mathbf{M_{MS}}$ and the whole revolution transfer matrix $\mathbf{M_{KK}}$ are described in Equation (4.7) and Equation (4.8), respectively, and j is assumed to be small enough such that the matrices $\mathbf{M_{MS}}$ and $\mathbf{M_{KK}}$ can be considered constant during j consecutive revolutions. It follows then

$$\Theta = \left\{ \mathbf{M_{MS}} \left[\mathbf{M_{KK}}^j \mathbf{x_K}(0) + \sum_{i=0}^{j} \left(\mathbf{M_{KK}}^{j-i} \mathbf{D_K}(i) \right) \right] \ \middle|\ \forall j \geq 0 \right\}. \tag{4.22}$$

For the simple case when the TFS is turned off, i.e., the TFS gain is set to zero, and the beam is not being kicked, we have

$$\Theta = \left\{ \mathbf{M_{MS}} \mathbf{M_{KK}}^j \mathbf{x_K}(0) \mid \forall j \geq 0 \right\}. \tag{4.23}$$

The functions in Equation (4.23) are linearly dependent on $\mathbf{x_K}(0)$, i.e., in the form $g_1(\mathbf{M_{MS}}, \mathbf{M_{KK}}) x_K(0) + g_2(\mathbf{M_{MS}}, \mathbf{M_{KK}}) x'_K(0)$. Therefore, the derivatives with respect to $\mathbf{X}_{Ex}(0)$ for calculating the Jacobian matrices will have the first two columns independent of $\mathbf{x_K}(0)$, and the rest of the columns linearly dependent on $\mathbf{x_K}(0)$. We have thus

$$\begin{aligned} &\mathbf{J}_\Theta \left(\left[\alpha \mathbf{x_K}(0)^T,\ Vec(\mathbf{M^P_{KK}}(0))^T,\ Vec(\mathbf{M^P_{MS}}(0))^T \right]^T \right) \\ &\quad = \mathbf{J}_\Theta \left(\left[\mathbf{x_K}(0)^T,\ Vec(\mathbf{M^P_{KK}}(0))^T,\ Vec(\mathbf{M^P_{MS}}(0))^T \right]^T \right) \ diag(1, 1, \alpha, \cdots, \alpha). \end{aligned} \tag{4.24}$$

Therefore, the rank of $\mathbf{J}_\Theta(\mathbf{X}_{Ex}(0))$ is not affected by scaling the beam status vector, and thus the number of dimensions of $\mathbf{J}_\Theta\left(\mathbf{X}_{Ex}(0)\right)$ is independent of the magnitude of $\mathbf{x_K}(0)$. That means that it is enough to sweep only the phase of the beam status vector $\mathbf{x_K}(0)$ while keeping constant magnitude and check the rank of the stacked Jacobian matrices in order to show the system observability. In other words, it is enough to sweep the beam status vector over the unitary circle.

In order to calculate the stacked Jacobian matrices $\mathbf{J}_\Theta\left(\mathbf{X}_{Ex}(0)\right)$, we use the following rules according to the results in [71]:

$$\frac{\partial \mathbf{M_{MS}}\mathbf{M_{KK}}^j\mathbf{x_K}}{\partial \mathbf{x_K}} = \mathbf{M_{MS}}\mathbf{M_{KK}}^j, \tag{4.25}$$

$$\frac{\partial (\mathbf{M_{MS}}\mathbf{M_{KK}}^j\mathbf{x_K})_i}{\partial (\mathbf{M_{MS}})_{mn}} = \delta_{im}(\mathbf{M_{KK}}^j\mathbf{x_K})_n, \tag{4.26}$$

$$\frac{\partial (\mathbf{M_{MS}}\mathbf{M_{KK}}^j\mathbf{x_K})_i}{\partial \mathbf{M_{KK}}} = \sum_{r=0}^{j-1} (\mathbf{M_{KK}}^r)^T \left((\mathbf{M_{MS}})_{i\cdot}\right)^T \mathbf{x_K}^T \left(\mathbf{M_{KK}}^{j-r-1}\right)^T, \tag{4.27}$$

where $(\cdot)_i$ denotes the i^{th} element of a vector, $(\cdot)_{i\cdot}$ denotes the i^{th} line of a matrix, $1 \leq i \leq M$, and $1 \leq n \leq 2$.

Since the differentials of the perturbation matrices $\mathbf{M^P_{KK}}$ and $\mathbf{M^P_{MS}}$ are equivalent to the differentials of the matrices $\mathbf{M_{KK}}$ and $\mathbf{M_{MS}}$ around their nominal values, respectively, we calculate the derivatives in Equation (4.26) and Equation (4.27) at the nominal values $\mathbf{M^{nom}_{KK}}$ and $\mathbf{M^{nom}_{MS}}$.

4.2.4 Observer

The optimal observer of a discrete-time controlled process described by a linear difference equation like Equation (4.3) with linear dependency of the measurements on the system status vector to be estimated like Equation (4.5) is the Kalman filter. It is the optimal estimator for the so called linear-quadratic problem [69, 72, 73].

The Kalman filter is not optimal anymore when the propagation of the system state vector as well as the measurement relation is according to a non-linear equation like in our robustification model in Equation (4.10) and Equation (4.13). However, a well known solution is to linearize the state vector propagation model as well as the measurement model around the current estimate. This is the so called Extended Kalman Filter (EKF) [69, 72]. This approach has been successfully applied in many applications in

signal processing. The model linearization is equivalent to taking the first order Taylor series of the model equation. This is done via calculating the partial derivatives of the system state propagation and measurement functions with respect to the system state vector, i.e., the Jacobian matrices for the system state vector propagation function and the measurement function

$$\mathbf{\Phi}_n = \left.\frac{\partial f(\mathbf{X}_{Ex})}{\partial \mathbf{X}_{Ex}}\right|_{\hat{\mathbf{X}}_{Ex}(n)}, \tag{4.28}$$

$$\mathbf{H}_{(n)} = \left.\frac{\partial h(\mathbf{X}_{Ex})}{\partial \mathbf{X}_{Ex}}\right|_{\hat{\mathbf{X}}_{Ex}(n)}, \tag{4.29}$$

where $\hat{\mathbf{X}}_{Ex}(n)$ denotes the a posteriori estimate of the system state vector at the turn n. The process function $f(\mathbf{X}_{Ex})$ and the measurement function $h(\mathbf{X}_{Ex})$ are described in Equation (4.12) and Equation (4.14), respectively.

The EKF is not optimal solution for our problem since it is not linear, it performs however a good sub-optimal approach that works well for systems with no high non-linearity like the case of our model with only second order non-linearity. It works iteratively as follows [69, 72]:

1. **Prediction**

   - Compute the predicted state estimate

$$\hat{\mathbf{X}}^{-}_{Ex}(n+1) = f_{\mathbf{D_K}(n+1)}(\hat{\mathbf{X}}^{+}_{Ex}(n)) \tag{4.30}$$

   - Compute the predicted measurement

$$\begin{aligned}\hat{\mathbf{x}}(n+1) &= h(\hat{\mathbf{X}}^{-}_{Ex}(n+1)) \\ &= \hat{\mathbf{M}}^{-}_{\mathbf{MS}}(n+1) \cdot \hat{\mathbf{x}}^{-}_{\mathbf{K}}(n+1)\end{aligned} \tag{4.31}$$

   - Compute the a priori covariance matrix

$$\mathbf{P}^{-}_{(n+1)} = \mathbf{\Phi}_n \mathbf{P}^{+}_{(n)} \mathbf{\Phi}^{T}_n + \mathbf{R_{NN}}, \tag{4.32}$$

2. **Update**

   - Conditioning the predicted estimate on the measurement

$$\begin{aligned}\hat{\mathbf{X}}^{+}_{Ex}(n+1) = \hat{\mathbf{X}}^{-}_{Ex}(n+1) + \mathbf{K}_{(n+1)} \cdot (\mathbf{x}(n+1) \\ - \hat{\mathbf{x}}(n+1))\end{aligned} \tag{4.33}$$

- Compute the a posteriori covariance matrix

$$\mathbf{P}^{+}_{(n+1)} = [\mathbf{I} - \mathbf{K}_{(n+1)}\mathbf{H}_{(n+1)}]\mathbf{P}^{-}_{(n+1)} \tag{4.34}$$

The Kalman gain at turn $n+1$ is given by

$$\begin{aligned}\mathbf{K}_{(n+1)} &= \mathbf{P}^{-}_{(n+1)} \cdot \mathbf{H}^{T}_{(n+1)} \\ &\cdot [\mathbf{H}_{(n+1)}\mathbf{P}^{-}_{(n+1)}\mathbf{H}^{T}_{(n+1)} + \mathbf{R_{ZZ}}]^{-1},\end{aligned} \tag{4.35}$$

The estimation of the extended state vector is done iteratively at every turn. The extended state vector is first predicted based on the estimate of the state of the previous turn according to the state propagation model. The predicted values are then adjusted according to the measured values at the PUs. For the initialization of the algorithm we can use the nominal values of the transfer an measure matrices, and the output of the estimator discussed in the previous chapter for the beam state vector.

The advantage of the EKF is that, in addition to estimating the system state, it gives an estimate of the precision in the estimated values as given within the covariance matrix $\mathbf{P}$.

4.3 Optics Transfer Determination

In this section, we address a method for measuring the phase advance and amplitude ratio between the beam oscillation at the kicker and the PUs positions. A rigid kick is applied on the beam, and the PU signals are recorded. The Second-Order Blind Identification (SOBI) algorithm [5, 6] is used subsequently to separate different beam oscillation sources from the noisy PU signals. The required optics parameters determination follows then by identifying, analyzing, and fitting the betatron oscillation on horizontal and vertical direction.

4.3.1 System Model

Let the TFS be composed of M PUs and a kicker located at different places around the accelerator ring. In order to make the required optics measurements for the TFS, we first of all perform a rigid initial kick on the beam by means of the kicker. We then start recording the turn-by-turn PU signals directly after the initial kick. The

turn-by-turn PU signal is calculated by averaging the displacement over a whole bunch. This averaging reduces the thermal noise power generated by the PUs.

The recorded beam transversal motion contains components sourced from different phenomena, e.g., betatron oscillation, head-tail modes, and synchrotron oscillation [74].

Suppose we record the PU signals over N turns. Let

$$\mathbf{x}_i = [x_i(1), \cdots, x_i(N)] \in \mathbb{R}^{1\times N} \tag{4.36}$$

denote the signal recorded from the i^{th} PU. This vector is the contribution of the beam transversal motion and the noise from the i^{th} PU, i.e.,

$$\mathbf{x}_i = \bar{\mathbf{x}}_i + \mathbf{z}_i, \tag{4.37}$$

where the vector $\bar{\mathbf{x}}_i$ represents the actual beam transversal offsets over the N turns at the position of the i^{th} PU, and $\mathbf{z}_i$ denotes the disturbing noise vector generated at this PU.

Let

$$\mathbf{X} = [\mathbf{x}_1^T, \cdots, \mathbf{x}_M^T]^T \in \mathbb{R}^{M\times N} \tag{4.38}$$

denote the matrix of the recorded signals over N turns from all the M PUs stacked together.

Assume the beam transversal motion is composed of K components driven by various sources. The recorded signals vector can be then written as

$$\mathbf{X} = \mathcal{A}\mathbf{S} + \mathbf{Z}, \tag{4.39}$$

where $\mathbf{Z}$ denotes the noise terms, which are assumed to be independent zero-mean Gaussian with variance σ^2, and $\mathbf{S} \in \mathcal{R}^{K\times N}$ denotes the source signals. $\mathcal{A} \in \mathcal{R}^{M\times K}$ is the source mixing matrix, which represents the coupling between the sources on the betatron motion.

After kicking a bunch in the transversal direction, it will perform transversal oscillation that contains components from the coherent betatron oscillation with the coherent tune frequency. The initial phase of the recorded oscillation at some PU corresponds to the phase difference between the kicker position and the position of this PU.

Furthermore, decoherence of the transverse bunch oscillation will occur, meaning that the amplitude of the oscillation will decrease over the time. This is a direct result

of the tune spread of the bunch particles due to the momentum spread and machine chromaticity. Recoherence of the transverse oscillation will follow after a while corresponding to the synchrotron period in a linear focusing lattice [75]. Therefore, the bunch transverse oscillation in vertical or horizontal direction can be stated as

$$x(n) = \mathbf{a}(n)\sin(Qn + \phi_0), \tag{4.40}$$

where Q denotes the coherent tune, and ϕ_0 is the initial phase. $\mathbf{a}(n)$ denotes the amplitude function of the transverse oscillation, and it can be written as [75–77]

$$\mathbf{a}(n) = a_0 \exp\left\{-2\left(\frac{\xi Q_0 \delta_p}{Q_s}\sin(\pi Q_s n)\right)^2\right\}, \tag{4.41}$$

where a_0 denotes the initial amplitude that depends on the strength of the rigid kick , ξ the chromaticity, δ_p the RMS momentum spread, and Q_s the tune of the synchrotron oscillation. This amplitude has also an exponentially decreasing trend due to the Landau damping.

Figure 4.3 shows recorded turn-by-turn beam oscillation at the heavy ions synchrotron SIS 18 at the GSI [75]. One can observe that this signal matches to the above described model.

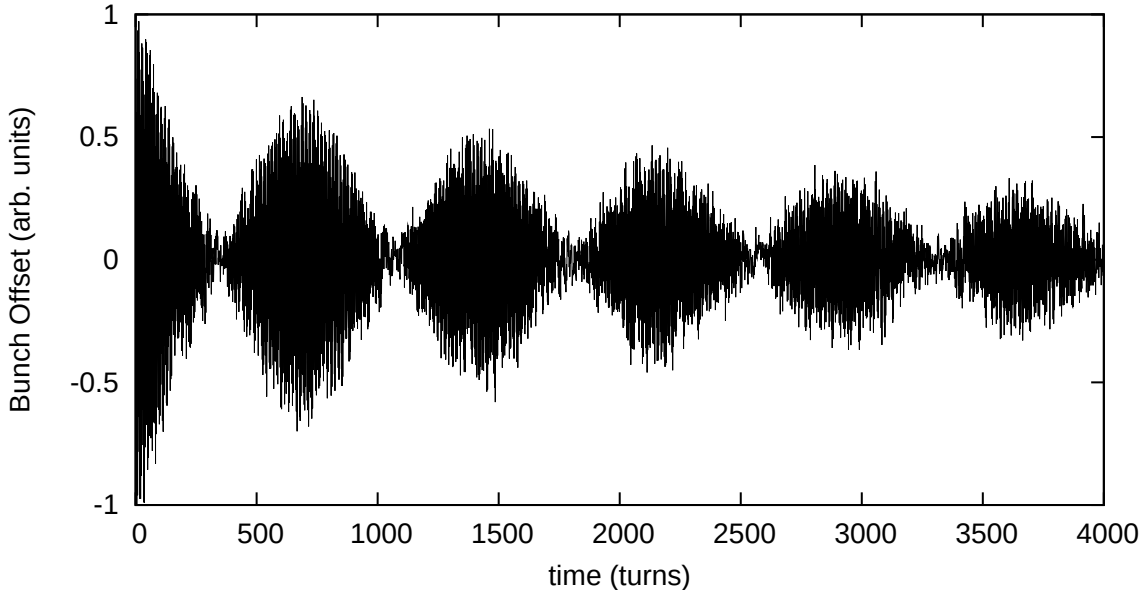

Figure 4.3. Recorded turn-by-turn beam oscillation in the vertical plane at SIS 18 [75].

4.3.2 Source Separation

The model parameters in Equation (4.40) and Equation (4.41) can be estimated with smaller error after removing the contribution of the irrelevant sources. Therefore, the separation of the sources contributing to the beam transversal oscillation according to Equation (4.39) is a very important step for a precise calculation of the parameters of the betatron oscillation.

The SOBI is a source separation technique based on the coherence of the source signals, which estimates the mixing matrix and separates the sources. This technique is considered to be more robust in poor signal to noise ratios due to utilizing second-order statistics, i.e., spatial covariance matrices of the measurements [5, 78].

The covariance matrix of the source signals is defined as

$$\mathbf{C_{SS}}(\tau) = E\{\mathbf{S}(t)\mathbf{S}(t+\tau)^T\}, \tag{4.42}$$

which is diagonal when the sources are independent.

From Equation (4.39) one can see that

$$\mathbf{C_{XX}}(\tau) = \mathcal{A}\mathbf{C_{SS}}(\tau)\mathcal{A}^T + \delta(\tau)\sigma^2\mathbf{I}, \tag{4.43}$$

where $\delta(\cdot)$ denotes the Dirac function. This means that the mixing matrix $\mathcal{A}$ is a diagonalizer of the measurements covariance matrix $\mathbf{C_{XX}}(\tau)$ for $\tau \neq 0$. This is a very important property to perform the source separation.

The SOBI algorithm can be performed to determine the mixing matrix $\mathcal{A}$ and the sources $\mathbf{S}$ as in the following steps [5, 6]:

1. Perform eigenvalue decomposition on $\mathbf{C_{XX}}(0)$
2. Put the K largest eigenvalues into the diagonal matrix Λ_S, and the corresponding eigenvectors into the matrix U_S. These eigenvalues represent the source signals, and the smallest ones represent the white noise
3. Define
$$\mathbf{V} = \Lambda_S^{-\frac{1}{2}} U_S^T, \tag{4.44}$$
and
$$\mathbf{\Psi} = \mathbf{V}\mathbf{X} \tag{4.45}$$

4. Estimate the covariance matrices $\mathbf{C}_{\mathbf{\Psi\Psi}}(\tau_k)$ for some delay time values τ_k, and calculate
$$\bar{\mathbf{C}}_{\mathbf{\Psi\Psi}}(\tau_k) = \frac{\mathbf{C}_{\mathbf{\Psi\Psi}}(\tau_k) + \mathbf{C}_{\mathbf{\Psi\Psi}}(\tau_k)^T}{2} \tag{4.46}$$

5. Find a matrix $\mathbf{W}$ which jointly diagonalizes all of the $\bar{\mathbf{C}}_{\mathbf{\Psi\Psi}}(\tau_k)$ for the selected time lags, i.e.,
$$\bar{\mathbf{C}}_{\mathbf{\Psi\Psi}}(\tau_k) = \mathbf{WDW}^T. \tag{4.47}$$

6. The mixing matrix is thus given by
$$\mathcal{A} = \mathbf{V}^{-1}\mathbf{W}, \tag{4.48}$$
and the corresponding source signals are
$$\mathbf{S} = \mathbf{W}^T\mathbf{VX}, \tag{4.49}$$
where $\mathbf{V}^{-1} = \mathbf{U}_S\mathbf{\Lambda}_S^{\frac{1}{2}}$.

Using the results of the SOBI algorithm, the phase and amplitude transfer between the kicker position and the PUs can be determined in the vertical and horizontal direction.

4.3.3 Optics Transfer Determination

After the source signals and the corresponding mixing matrices have been determined, the components of the betatron oscillation in some direction, e.g., horizontal direction, can be identified by its tune frequency, which must be closed to the nominal value. This betatron oscillation must have two components with orthogonal phases since the PU signals include this oscillation with different phases.

The betatron oscillation should follow the model described in Equation (4.40) and Equation (4.41) in beam offset and angle. Therefore, the beam oscillation following the kick will occur according to the decoherence/recoherence model with a maximum amplitude proportional to the kick, and zero initial phase since the oscillation is supposed to start from zero offset, assuming a stable beam. Thus, the phase transfer between the kicker position and the PUs is equal to the initial phases of the betatron oscillation recorded at each PU. The amplitude transfer is then the ratio of the maximum amplitude for each PU and the kick.

Within the extracted components of the betatron oscillation some portion of the noise is superimposed. Therefore, a nonlinear fitting approach is used to determine the initial

phase and the amplitude parameters in the two betatron components. Let $\hat{\alpha}_1$ and $\hat{\alpha}_2$ denote the estimated initial amplitudes of these components, and $\hat{\varphi}_1$ and $\hat{\varphi}_2$ denote the estimated phases. The amplitude ratio of the betatron oscillation between the position of the kicker and PU_i can be written as

$$T_{\beta_i} = \frac{\sqrt{\hat{\alpha}_1^2(\mathcal{A}_{ib_1})^2 + \hat{\alpha}_2^2(\mathcal{A}_{ib_2})^2}}{\beta_K D_K}, \tag{4.50}$$

and the phase transfer

$$\Delta\Phi_i = \arctan(\frac{\hat{\alpha}_1(\mathcal{A}_{ib_1})}{\hat{\alpha}_2(\mathcal{A}_{ib_2})}) + \hat{\varphi}_1, \tag{4.51}$$

where $(\mathcal{A}_{ib_j})$ denotes the element within the mixing matrix corresponding to the signal of PU_i and betatron component $j \in \{1, 2\}$, and D_K represents the kick strength. β_K is the value of the beta function at the kicker position, which is assumed to be known precisely from a previous measurement campaign.

The value of β_K appears only in the formula of the amplitude transfer in Equation (4.50) as a scaling factor of all parameters. Therefore, the errors in measuring β_K affect the estimate of the feedback correction signal using our approach of the MVUE only by a scaling factor without changing the right phase, which is very crucial for correctly damping feedback.

Since the two betatron components for some transversal direction resulting from the SOBI algorithm are orthogonal, the following must hold

$$\hat{\varphi}_2 \approx \hat{\varphi}_1 + \frac{\pi}{2}. \tag{4.52}$$

This can be exploited to enhance the phase estimation from the nonlinear fitting. In this case, both phases can be estimated from each component and averaged over the two estimates.

4.4 Results

In this section, we show simulation results of the above addressed approaches in this chapter for the heavy ions Synchrotron SIS 18 at the GSI. In the SIS 18, there are 12 beam position PUs for the horizontal and vertical directions, which are located periodically along the synchrotron ring. There is also one kicker for each transversal direction.

As already discussed in the previous chapter, the transversal focusing optics change continuously in this synchrotron from the so called triplet mode to the doublet mode during the acceleration cycle. This leads to non-constant betatron functions during operation.

4.4.1 Robust TFS

We show in this section simulation results for the triplet mode in the horizontal direction for using the two closest PUs to the kicker. The nominal values of the twiss parameters for the PUs and the kicker are shown in Table 3.1. The nominal tune for the horizontal direction is $Q_x^{nom} = 4.31$. The phase difference between the kicker and the first PU has a nominal value $\mathbf{\Delta}\phi_{\mathbf{1}}^{\mathbf{nom}} = 103.7°$, and the phase difference between the two PUs is $\mathbf{\Delta}\phi_{\mathtt{PUs}}^{\mathbf{nom}} = 129.3°$ nominally.

Using the values in Table 3.1 and substituting in Equation (2.14) we find the nominal whole turn transfer matrix as

$$\mathbf{M_{KK}^{nom}} = \begin{pmatrix} -1.6326 & 13.0727 \\ -0.1884 & 0.8964 \end{pmatrix}. \tag{4.53}$$

Assuming feedback in the second turn, the measurement matrix is given as

$$\mathbf{M_{MS}^{nom}} = \begin{pmatrix} -1.5208 & 7.7126 \\ 0.5724 & 3.5444 \end{pmatrix}. \tag{4.54}$$

In order to check the observability of the system model stated in Equation (4.10) and Equation (4.13) around nominal values of whole turn transfer matrix and the measurement matrix, we calculate the rank of the stacked Jacobian matrices of Θ given in Equation (4.22) for $0 \leq j \leq 4$. As already discussed in a previous section, it is enough to sweep the initial beam state vector around the unitary circle, i,e, $\mathbf{x_K}(0) = [\cos(\phi),\ \sin(\phi)]^T,\ \ \phi \in [0, 360[$ `(deg.)`, in order to show the observability of the given system for any possible beam offset and angle.

Figure 4.4 depicts the determinant of the stacked Jacobian matrix for the considered number of turns with noisy TFS kicks. The determinant values are far from 0, which shows that the stacked Jacobian matrix is far from being singular for any possible initial beam offset and angle. Therefore, the robust system formulation is observable, and we show results for our suggested observer in the following.

We assume an actual tune of $Q_x = 4.15$ for the horizontal direction. This corresponds to about 60° deviation from the nominal tune value. The deviations in the considered actual values of the phase advances between the kicker and the first PU as well as between the two PUs from the nominal values are assumed to be 30%. The nominal and actual values of the Twiss parameters for the PUs and the kicker are shown in Table 4.1.

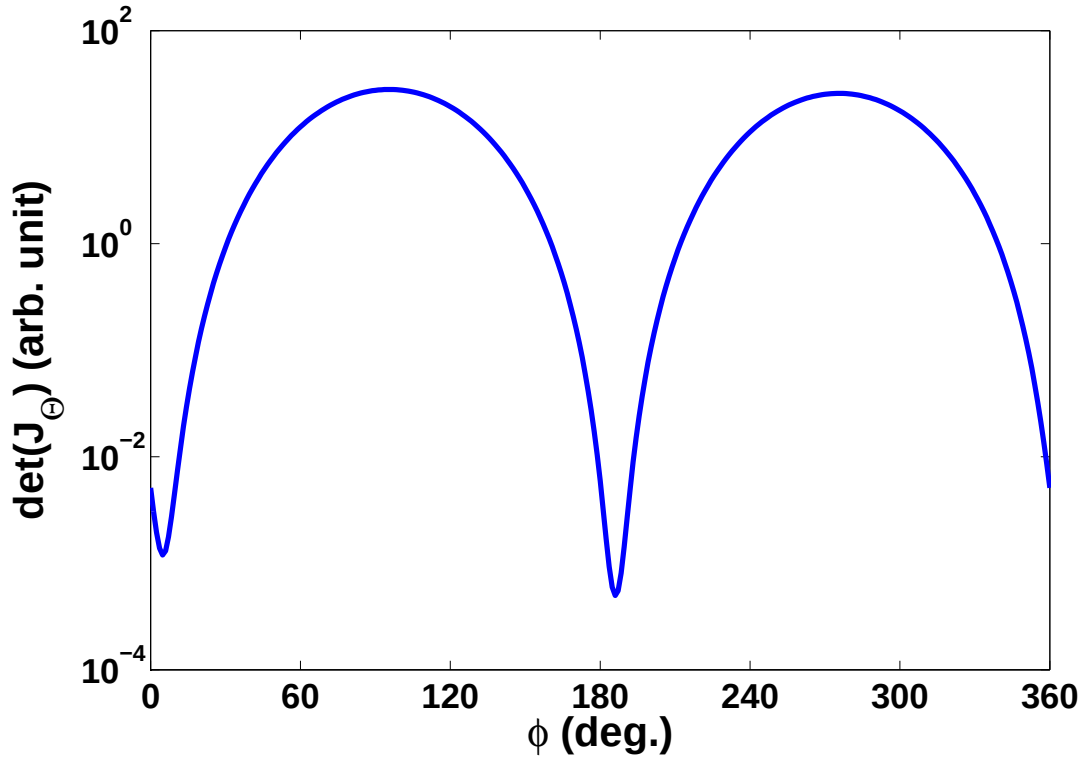

Figure 4.4. Determinant of the Jacobian matrix.

Table 4.1. Nominal and actual Twiss Parameters

Accuracy	$\beta_{\mathbf{k}}$	$\beta_{\mathbf{pu}}$	$\alpha_{\mathbf{k}}$	$\alpha_{\mathbf{pu}}$
Nominal	14.06	12.67	-1.36	1.24
Actual	9.84	16.47	-0.95	1.74

We show results for bunch oscillation with an initial bunch offset from the ideal trajectory of 2 `cm` and zero beam angle, i.e., the initial status vector is $\mathbf{x}(0) = [2\ \texttt{cm},\ 0\ \texttt{rad}]^T$. This leads to beam oscillation with the amplitude of the beam offset of 5.9 cm at the kicker location. The bunch movement has been generated using the actual optics parameters. We consider model disturbances $\mathbf{n_p} \sim N(\mathbf{0},\ \mathbf{R_{nn}})$, where $\mathbf{R_{nn}} = 10^{-7} \cdot diag(0.73,\ 0.028)$, which corresponds to standard deviations in the beam offset and angle of 1% of the ideal beam oscillation without disturbances. The measurements are disturbed by additive white Gaussian noise with zero mean and standard deviation of $\sigma_z = 0.5$ `cm`.

Figure 4.5 shows the Root Mean Squared Error (RMSE) in the beam offset estimation at the kicker location for three different estimators. The blue curve (EKF) corresponds to the RMSE of our addressed robust approach that applies the Extended Kalman Filter, where the black curve (Vector Sum) corresponds to the RMSE of the vector

summation approach addressed in [3] considering the nominal optics parameters of the SIS 18 as a comparison reference. The red curve (KF) corresponds to the RMSE of the approach of applying the linear Kalman Filter using the nominal values of the synchrotron optics parameters as another comparison reference.

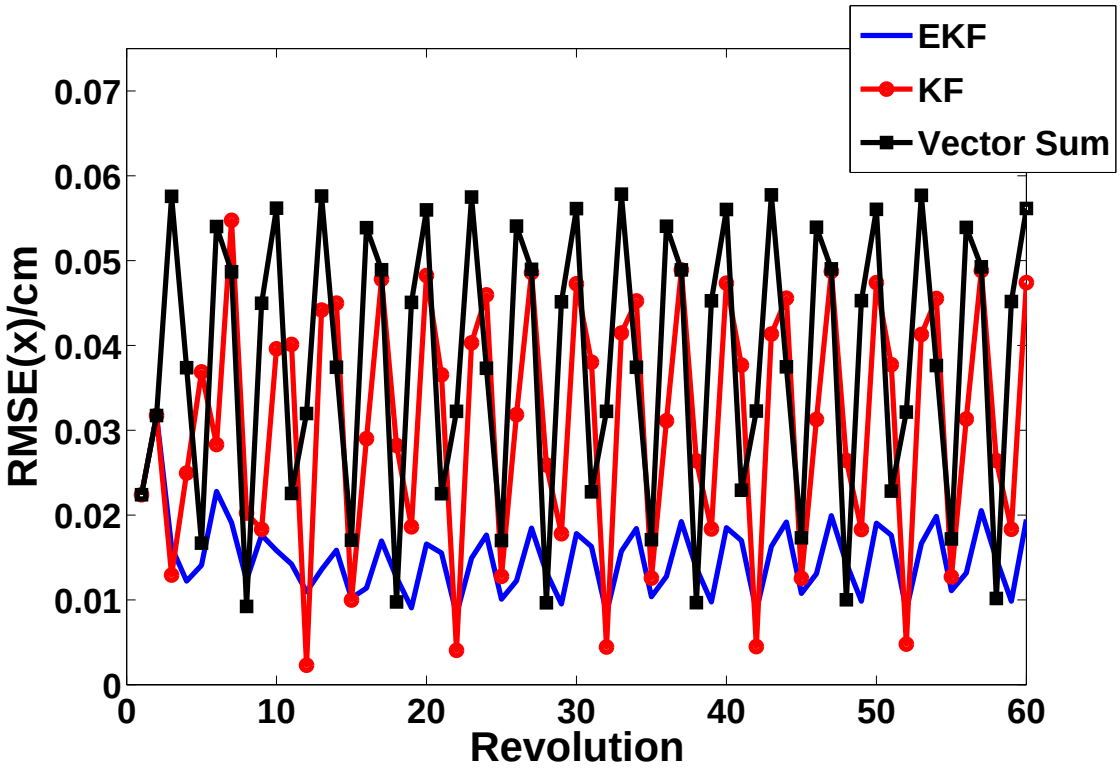

Figure 4.5. RMSE of beam offset estimation at the kicker location.

The curves of Figure 4.5 show that the average value over time of the RMSE in the beam offset estimation at the kicker location using our addressed robust approach is about one third of the corresponding value for the vector summation approach, and less than a half of the corresponding value using the approach of applying the linear Kalman Filter with nominal optics parameters. The exemplary time domain signals of the actual beam offset oscillation and its estimates depicted in Figure 4.6 show that the matching between the actual beam oscillation signal and the estimated signal using our robust approach is much better than using the other reference approaches. This leads to enhancing the quality of the feedback correction signal using our addressed robust approach in comparison to the other two reference approaches. This is very crucial for the beam quality, since it reduces the beam emittance growth, and therefore increases the collider luminosity.

Moreover, it is very important to mention that using our new robust approach leads to the enhancements with the price of more computational cost in the calculation of

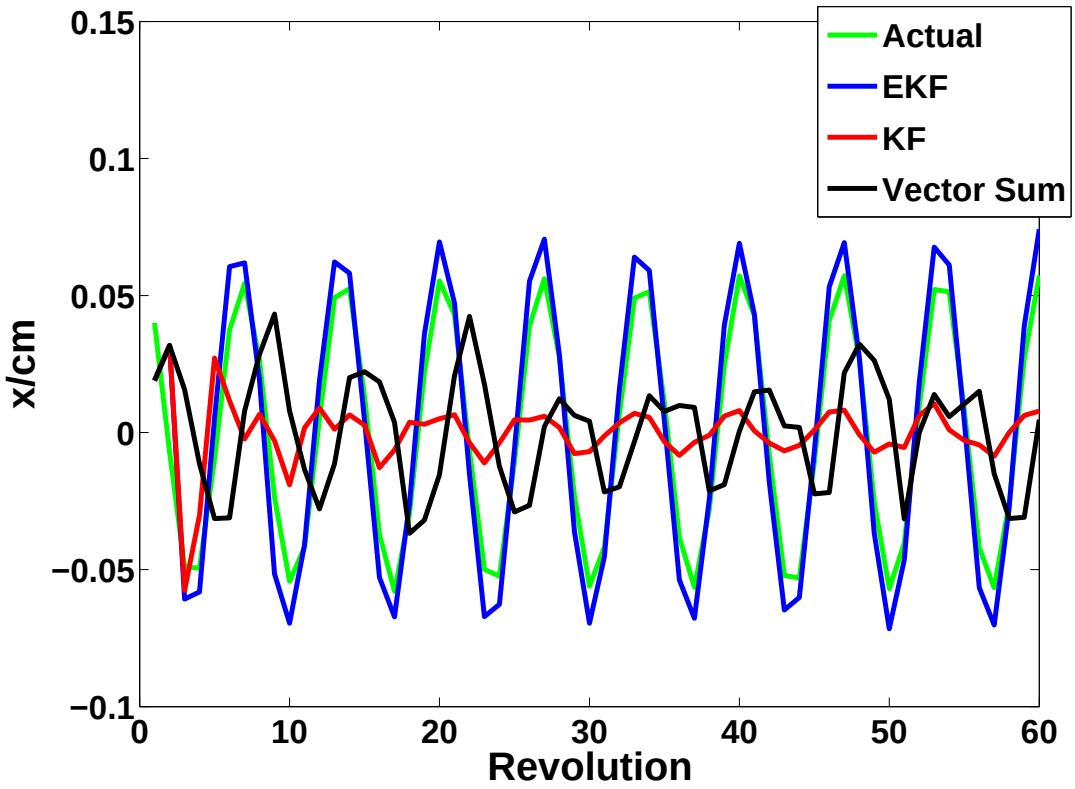

Figure 4.6. Beam offset oscillation and its estimates.

the feedback correction signal, and implementation complexity. This computational cost comes mainly from the matrix inversion operation in the EKF algorithm. This depends on the number of involved PUs. The rounding errors depending on the implemented number precision and their impact on the performance must be also carefully investigated. Furthermore, the noise covariance matrices must be estimated and set carefully in order to guarantee a stable behavior of the EKF.

4.4.2 Optics Transfer Determination

In this section, we show simulation results of the above addressed approach for the precise optics determination between the kicker and the PUs at the heavy ions Synchrotron SIS 18 at the GSI.

We have generated a betatron oscillation emerging from a rigid kick on the beam in the horizontal direction in the triplet mode according to the model described in Equation (4.40) and Equation (4.41) with the tune $Q_x = 4.29$. The corresponding

signals were generated at the 12 PUs according to the betatron parameters of the SIS 18 listed in Table 3.1. A small coupling part from the vertical and the longitudinal oscillations, as well as Gaussian measurement noise with standard deviation of 25% of highest signal amplitude were added. Using the above described method we were able to determine the phase advances with about 2° error, and the amplitude scaling with a less than 5% error.

Chapter 5

Non-Linear Optics Components Detection and Measurement

The knowledge of the linear and non-linear magnets errors in circular accelerator optics is very crucial for controlling and compensating resonances and their consequent beam losses and beam quality deterioration. This is indispensable, especially for high beam intensity machines. Fortunately, the relationship between the beam offset oscillation signals recorded at the BPMs is a manifestation of the accelerator optics, and can therefore be exploited in the determination of the optics linear and non-linear components.

In this chapter, we propose a novel method for detecting and estimating the optics lattice non-linear components located in-between the locations of two BPMs by analyzing the beam offset oscillation signals of a BPMs-triple containing these two BPMs. Depending on the non-linear components in-between the locations of the BPMs-triple, the relationship between the beam offsets follows a multivariate polynomial accordingly. After calculating the covariance matrix of the polynomial terms, the Generalized Total Least Squares method is used to find the model parameters, and thus the non-linear components. A bootstrap technique is used to detect the existing polynomial model orders by means of multiple hypothesis testing, and determine confidence intervals for the model parameters. Results for synthetic and real data recorded at the heavy ions synchrotron SIS 18 at the GSI are shown.

5.1 Motivation

In high energy particle accelerators, magnetic fields are usually employed for beam focusing and deflection since the corresponding Lorentz force gets stronger for higher velocities, and electric fields are used for beam acceleration. Synchrotrons use cavities to generate the accelerating electric fields synchronized in phase and frequency with the beam, and electric magnets to generate the focusing and deflecting magnetic fields with proper strengths depending on the beam energy.

Constant magnetic fields, i.e., with zero gradient, generated by dipole magnets with proper strength are usually used for beam deflection in synchrotrons. Linear magnetic

fields, i.e., with constant gradient, generated by quadrupole magnets are usually used for beam focusing. Periodic sequences of focusing/defocusing quadrupole magnets with drift tubes in-between called FODO cells are usually used for focusing in horizontal and vertical directions. This is called the strong focusing. Furthermore, other non-linear magnetic fields generated by sextupole or octupole magnets can be applied on purpose, e.g., for chromaticity compensation or slow beam extraction.

In addtion to the required magnetic fields, the magnets can generate unwanted spurious linear and non-linear magnetic fields [7] due to fabrication imperfection of the magnets and the aging of the magnets materials. These error fields in the magnets excite undesired resonances leading together with the space charge tune spread to beam quality deterioration, long term beam losses, and reducing the dynamic aperture [8,9]. Therefore, these magnets errors and their impact on the beam must be studied and evaluated thoroughly in order to control and compensate their distorting contribution on the accelerated beam for a better machine operation, such that the demand for higher beam intensity can be fulfilled. Thus, the detection and measurement of the linear and non-linear error components in circular accelerator optics is indispensable, especially for high intensity machines.

The utilization of the non-linear chromaticity measurement for determining the non-linear optics model by exploiting the nonlinear dependence of the tune on the relative momentum offset has been presented in [26, 27, 79]. In [8, 9, 25], The Non-Linear Tune Response Matrix (NTRM) technique has been proposed to be used for diagnosing non-linear magnetic field components. These methods are however very costly and require long measurement campaigns apart from having difficulties in estimating non-linear components with mixed orders.

In this chapter, we address a novel Lightweight approach for determining optics linear and non-linear components in a circular particle accelerator without demanding heavy measurement campaigns. The relationship between the beam offset oscillation signals recorded at the BPMs is a manifestation of the accelerator optics, and can be therefore exploited in order to determine the optics linear and non-linear components. A pencil like beam is preferred with this approach in order to get rid of finite beam size effects on the BPM signals. Such a beam can be reached by an optimized one turn injection [25]. We estimate the lattice non-linear components located in-between the locations of two BPMs by analyzing the beam offset oscillation signals of a BPMs-triple containing these two BPMs. The Generalized Total Least Squares method is applied on the recorded BPM signals after a proper preprocessing for parameter estimation, and a bootstrap technique is used to to detect the existing model orders and determine confidence intervals for the model parameters.

5.2 System Model

Three coordinate axes are defined for each position along the synchrotron ring, which determine the different beam offsets from the ideal closed orbit as in the previous chapters: x denotes the horizontal and y the vertical offset of a the bunch or bunch slice. The longitudinal coordinate is denoted by s.

Multiple BPMs for acquiring horizontal and vertical beam offsets are usually placed at different positions along the accelerator ring. The BPM signals must be delayed accordingly, i.e., synchronized, such that they correspond to the same beam segment or bunch at every sample.

Let $x_i(t)$ and $y_i(t)$ be the signals at BPM_i located at the position s_i along the accelerator ring at time t, where $i \in \{1,\ 2, \cdots,\ M\}$. These signals correspond to the actual beam horizontal and vertical offsets $\tilde{x}_i(t)$ and $\tilde{y}_i(t)$ at s_i perturbed by noise terms $z_{xi}(t)$ and $z_{yi}(t)$, respectively. This means

$$\begin{pmatrix} x_i(t) \\ y_i(t) \end{pmatrix} = \begin{pmatrix} \tilde{x}_i(t) \\ \tilde{y}_i(t) \end{pmatrix} + \begin{pmatrix} z_{xi}(t) \\ z_{yi}(t) \end{pmatrix}. \tag{5.1}$$

The basic focusing optics is ideally composed of linear FODO cells. Furthermore, other non-linear components are existing along the accelerator ring. These non-linear components could be put on purpose, like chromaticity compensating sextupoles, or dipole, sextupole, or octupole magnet non-linear errors with an integrated strength located at some position. In Fig. 5.1, the optics model is depicted for some exemplary section of an accelerator ring with three BPMs. Focusing and defocusing magnets as well as a non-linear component named as $\mathrm{N_i}$ are shown. Multiple non-linear components with different orders could also exist in this model.

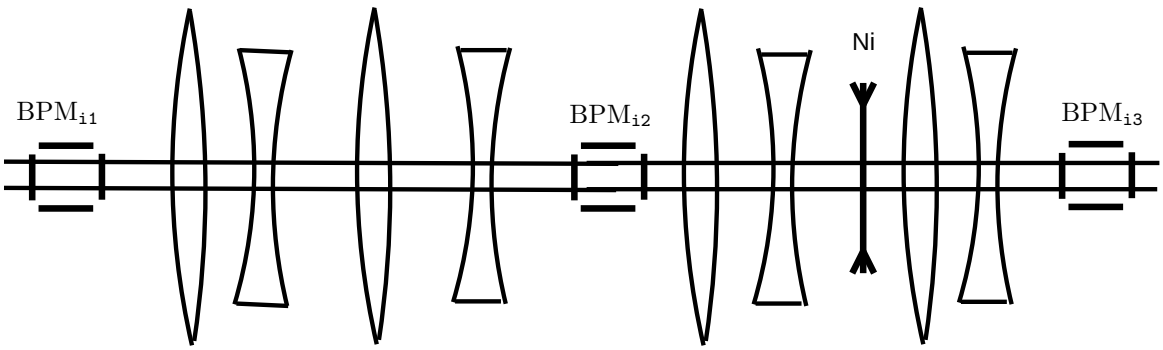

Figure 5.1. Optics model.

For the sake of simplicity, we assume that the non-linear components exist between $\mathrm{BPM}_{\mathtt{i2}}$ and $\mathrm{BPM}_{\mathtt{i3}}$, and not between $\mathrm{BPM}_{\mathtt{i1}}$ and $\mathrm{BPM}_{\mathtt{i2}}$. This constelllation can be found in any particle accelerator, if there are no non-linear components between at least two BPMs. In this case, one could take a BPM triple containing these two BPMs, and our assumption would not affect the applicability of our approach. Such BPMs could be for instance bounding a section without magnets errors, or without magnets at all, i,e, a drift tube.

Under this assumption, the beam offset and angle directly before the location of the non-linear components can be written in linear dependence on the beam offsets at $\mathrm{BPM}_{\mathtt{i1}}$ and $\mathrm{BPM}_{\mathtt{i2}}$, i.e.,

$$\begin{pmatrix} x_{Ni}(t) \\ x_{Ni}(t)' \\ y_{Ni}(t) \\ y_{Ni}(t)' \end{pmatrix} = \mathbf{M}_i \begin{pmatrix} \tilde{x}_{i1}(t) \\ \tilde{x}_{i2}(t) \\ \tilde{y}_{i1}(t) \\ \tilde{y}_{i2}(t) \end{pmatrix} \tag{5.2}$$

where $x_{Ni}(t)$, $y_{Ni}(t)$, $x_{Ni}(t)'$, and $y_{Ni}(t)'$ denote the beam horizontal and vertical offsets, and horizontal and vertical angles, respectively. The matrix $\mathbf{M}_i$ can contain coupling terms between the horizontal and vertical direction depending on the skewing of the linear magnets.

Since the beam offsets at the location of $\mathrm{BPM}_{\mathtt{i3}}$ can be written as a multivariate polynomial function of the beam status, i.e., horizontal and vertical offsets and angles, directly before the non-linear components, one can write it as a multivariate polynomial of the beam offsets at the locations of $\mathrm{BPM}_{\mathtt{i1}}$ and $\mathrm{BPM}_{\mathtt{i2}}$ depending on the orders and the number of the non-linear components. Therefore,

$$\begin{pmatrix} \tilde{x}_{i3}(t) \\ \tilde{y}_{i3}(t) \end{pmatrix} = f(\tilde{x}_{i1}(t), \tilde{x}_{i2}(t), \tilde{y}_{i1}(t), \tilde{y}_{i2}(t)), \tag{5.3}$$

where $f(.)$ is a multivariate polynomial of an order that depends on the non-linear components. Hence, one can write for some order N

$$\tilde{x}_{i3}(t) = \sum_{i+j+k+l \leq N} \alpha_{ijkl} \tilde{x}_{i1}(t)^i \tilde{x}_{i2}(t)^j \tilde{y}_{i1}(t)^k \tilde{y}_{i2}(t)^l \tag{5.4a}$$

$$\tilde{y}_{i3}(t) = \sum_{i+j+k+l \leq N} \lambda_{ijkl} \tilde{x}_{i1}(t)^i \tilde{x}_{i2}(t)^j \tilde{y}_{i1}(t)^k \tilde{y}_{i2}(t)^l, \tag{5.4b}$$

where the parameters α_{ijkl} and λ_{ijkl} of this model are a direct manifestation of the linear and non-linear optics lattice components of the accelerator section located between $\mathrm{BPM}_{\mathtt{i1}}$ and $\mathrm{BPM}_{\mathtt{i3}}$.

5.3 Parameter Estimation

The model parameters of the relationship between the beam offset oscillations at different BPM locations in Equation (5.4) that depend on the optics linear and non-linear components between the locations of these BPMs can be estimated via fitting the model to the noisy measured data at the BPMs.

The dependency of the measurements at the BPMs on the model parameters described in Equation (5.1) and Equation (5.4) represents an errors-in-variables regression system. Such a model can be solved using a Generalized Total Least Squares (GTLS) approach.

After collecting measurements over K samples from each BPM, the GTLS problem can be stated as

$$\mathbf{Y} \approx \mathbf{X}\beta, \tag{5.5}$$

where

$$\mathbf{Y} = \begin{pmatrix} x_{i3}(1) & y_{i3}(1) \\ \vdots & \vdots \\ x_{i3}(K) & y_{i3}(K) \end{pmatrix} \in \mathbb{R}^{K\times 2}, \tag{5.6}$$

and

$$\mathbf{X} = \begin{pmatrix} X_1(1) & \cdots & X_T(1) \\ \vdots & \vdots & \vdots \\ X_1(K) & \cdots & X_T(K) \end{pmatrix} \in \mathbb{R}^{K\times T}, \tag{5.7}$$

where $X_1(1), \cdots, X_T(i)$ denote the multivariate polynomial terms $x_{i1}(t)^i x_{i2}(t)^j y_{i1}(t)^k y_{i2}(t)^l,\ i+j+k+l \leq N$ constructed from the measured values at the BPMs. $\beta \in \mathbb{R}^{T\times 2}$ denotes the matrix of the corresponding stacked model parameters such that α_{ijkl} constitute the first column and λ_{ijkl} constitute the second column.

With different polynomial coefficients in the horizontal and vertical directions at $\mathrm{BPM}_{\mathtt{i3}}$, the formulated GTLS in Equation (5.5) can be splitted into two problems that can be solved separately for each direction.

The matrices $\mathbf{X}$ and $\mathbf{Y}$ contain the values of the corresponding terms with the actual beam offsets at the locations of the BPMs and noise perturbation terms, i.e.,

$$\mathbf{X} = \tilde{\mathbf{X}} + \mathbf{Z}_{\mathbf{X}}, \tag{5.8}$$

$$\mathbf{Y} = \tilde{\mathbf{Y}} + \mathbf{Z}_{\mathbf{Y}}. \tag{5.9}$$

Define

$$\mathbf{Z} = vec([\mathbf{Z_X},\ \mathbf{Z_Y}]), \tag{5.10}$$

the condition for the Total Least Squares (TLS) estimator of the true parameters stacked in the matrix β to be consistent, i.e., $\beta_{\texttt{TLS}} \rightarrow \beta_{\texttt{true}}$ in probability as $K \rightarrow \infty$, is that the vector $\mathbf{Z}$ has a zero mean with a covariance matrix that is multiple of the identity matrix [80, 81].

Since this condition is not fulfilled in our estimation problem in Equation (5.5) due to the given structure of $\mathbf{X}$, The GTLS method must be applied, or pre-processing (pre-whitening) must be undertaken on the data before the TLS estimator can be applied. The first step in this algorithm is to calculate the covariance matrix $\mathbf{R_{ZZ}}$ of $\mathbf{Z}$ in Equation (5.10).

5.3.1 Noise Covariance Matrix

In order to find a consistent estimates of the model parameters, the covariance matrix of the noise in the polynomial terms $X_{ijkl} = x_{i1}(t)^i x_{i2}(t)^j y_{i1}(t)^k y_{i2}(t)^l$, $i+j+k+l \leq N$ must be first calculated. The elements of the covariance matrix can be calculated for all possible polynomial terms starting with the lower order terms, and follow up with increasing orders using the results of the previous lower orders.

We show in the following the calculation steps of the covariance matrix elements for up to the second order polynomial terms, i.e., with the existence of sextupolar magnetic field, as a demonstrating example. This corresponds to model polynomials of the form

$$\begin{aligned} p(\tilde{x}_i, \tilde{x}_j, \tilde{y}_i, \tilde{y}_j) =& a_1\tilde{x}_i + a_2\tilde{x}_j + a_3\tilde{y}_i + a_4\tilde{y}_j + a_5\tilde{x}_i^2 + a_6\tilde{x}_j^2 + \\ & a_7\tilde{x}_i\tilde{x}_j + a_8\tilde{y}_i^2 + a_9\tilde{y}_j^2 + a_{10}\tilde{y}_i\tilde{y}_j. \end{aligned} \tag{5.11}$$

This leads to a noise covariance matrix with 10 dimensions, and thus 55 elements to be calculated due to the symmetry.

We define $C_{Z_{X_{i_1 j_1 k_1 l_1}} Z_{X_{i_2 j_2 k_2 l_2}}}$ to be the cross-covariance of the noise terms in $X_{i_1 j_1 k_1 l_1}$ and $X_{i_2 j_2 k_2 l_2}$. From Equation (5.1) one can see that

$$C_{Z_{x_i} Z_{y_j}} = \mathrm{E}(z_{xi} z_{yj}) = 0 \ \ \forall i, j, \tag{5.12}$$

$$C_{Z_{x_i} Z_{x_j}} = \mathrm{E}(z_{xi} z_{xj}) = C_{Z_{y_i} Z_{y_j}} = \mathrm{E}(z_{yi} z_{yj}) = 0 \ \ \forall i \neq j, \tag{5.13}$$

and

$$C_{Z_{x_i} Z_{x_j}} = \mathrm{E}(z_{xi} z_{xj}) = C_{Z_{y_i} Z_{y_j}} = \mathrm{E}(z_{yi} z_{yj}) = \sigma^2 \ \ \forall i = j. \tag{5.14}$$

Furthermore, we have

$$x_i{}^2 = (\tilde{x}_i + z_{xi})^2 = \tilde{x}_i^2 + \underbrace{2\tilde{x}_i z_{xi} + z_{xi}{}^2}_{\text{noise part}}, \tag{5.15}$$

$$y_i{}^2 = (\tilde{y}_i + z_{yi})^2 = \tilde{y}_i^2 + \underbrace{2\tilde{y}_i z_{yi} + z_{yi}{}^2}_{\text{noise part}}, \tag{5.16}$$

$$x_i x_j = (\tilde{x}_i + z_{xi})(\tilde{x}_j + z_{xj}) = \tilde{x}_i\tilde{x}_j + \underbrace{\tilde{x}_i z_{xj} + \tilde{x}_j z_{xi} + z_{xi}z_{xj}}_{\text{noise part}}, \tag{5.17}$$

$$y_i y_j = (\tilde{y}_i + z_{yi})(\tilde{y}_j + z_{yj}) = \tilde{y}_i\tilde{y}_j + \underbrace{\tilde{y}_i z_{yj} + \tilde{y}_j z_{yi} + z_{yi}z_{yj}}_{\text{noise part}}, \tag{5.18}$$

and

$$x_i y_j = (\tilde{x}_i + z_{xi})(\tilde{y}_j + z_{yj}) = \tilde{x}_i\tilde{y}_j + \underbrace{\tilde{x}_i z_{yj} + \tilde{y}_j z_{xi} + z_{xi}z_{yj}}_{\text{noise part}}. \tag{5.19}$$

Therefore, we have

$$C_{Z_{x_i}{}^2 Z_{y_j}{}^2} = C_{Z_{x_i}{}^2 Z_{y_j}} = C_{Z_{x_i} Z_{y_j}{}^2} = C_{Z_{x_i}{}^2 Z_{x_j}} = C_{Z_{y_i}{}^2 Z_{y_j}} = C_{Z_{x_i x_j} Z_{y_i}{}^2} = 0 \ \ \forall i, j, \tag{5.20}$$

$$C_{Z_{x_i x_j} Z_{x_i}} = C_{Z_{x_i x_j} Z_{y_i}} = 0 \ \ \forall i, j, \tag{5.21}$$

$$C_{Z_{x_i}{}^2 Z_{x_j}{}^2} = C_{Z_{y_i}{}^2 Z_{y_j}{}^2} = 0 \ \ \forall i \neq j, \tag{5.22}$$

$$C_{Z_{x_i}{}^2 Z_{x_i}{}^2} = \mathrm{E}\left\{(2\tilde{x}_i z_{xi} + z_{xi}{}^2 - \mathrm{E}\{2\tilde{x}_i z_{xi} + z_{xi}{}^2\})^2\right\} = \sigma^2\left(4\mathrm{E}\{\tilde{x}_i^2\} + 2\sigma^2\right), \tag{5.23}$$

$$C_{Z_{y_i}{}^2 Z_{y_i}{}^2} = \mathrm{E}\left\{(2\tilde{y}_i z_{yi} + z_{yi}{}^2 - \mathrm{E}\{2\tilde{y}_i z_{yi} + z_{yi}{}^2\})^2\right\} = \sigma^2\left(4\mathrm{E}\{\tilde{y}_i^2\} + 2\sigma^2\right), \tag{5.24}$$

$$\begin{aligned} C_{Z_{x_i x_j} Z_{x_i}{}^2} &= \mathrm{E}\left\{(2\tilde{x}_i z_{xi} + z_{xi}{}^2 - \sigma^2)(\tilde{x}_i z_{xj} + \tilde{x}_j z_{xi} + z_{xi}z_{xj})\right\} \\ &= 2\sigma^2\mathrm{E}\left\{\tilde{x}_i\tilde{x}_j\right\} \ \ \forall i, j, \end{aligned} \tag{5.25}$$

$$\begin{aligned} C_{Z_{y_i y_j} Z_{y_i}{}^2} &= \mathrm{E}\left\{(2\tilde{y}_i z_{yi} + z_{yi}{}^2 - \sigma^2)(\tilde{y}_i z_{yj} + \tilde{y}_j z_{yi} + z_{yi}z_{yj})\right\} \\ &= 2\sigma^2\mathrm{E}\left\{\tilde{y}_i\tilde{y}_j\right\} \ \ \forall i, j, \end{aligned} \tag{5.26}$$

$$\begin{aligned} C_{Z_{x_i x_j} Z_{x_i x_j}} &= \mathrm{E}\left\{(\tilde{x}_i z_{xj} + \tilde{x}_j z_{xi} + z_{xi}z_{xj})(\tilde{x}_i z_{xj} + \tilde{x}_j z_{xi} + z_{xi}z_{xj})\right\} \\ &= \sigma^2\left(\mathrm{E}\left\{\tilde{x}_i^2\right\} + \mathrm{E}\left\{\tilde{x}_j^2\right\} + \sigma^2\right) \ \ \forall i, j, \end{aligned} \tag{5.27}$$

and

$$\begin{aligned} C_{Z_{y_i y_j} Z_{y_i y_j}} &= \mathrm{E}\left\{(\tilde{y}_i z_{yj} + \tilde{y}_j z_{yi} + z_{yi}z_{yj})(\tilde{y}_i z_{yj} + \tilde{y}_j z_{yi} + z_{yi}z_{yj})\right\} \\ &= \sigma^2\left(\mathrm{E}\left\{\tilde{y}_i^2\right\} + \mathrm{E}\left\{\tilde{y}_j^2\right\} + \sigma^2\right) \ \ \forall i, j, \end{aligned} \tag{5.28}$$

where the estimates of $\mathrm{E}\{\tilde{x}_i^2\}$, $\mathrm{E}\{\tilde{y}_i^2\}$, $\mathrm{E}\{\tilde{x}_i\tilde{x}_j\}$, and $\mathrm{E}\{\tilde{y}_i\tilde{y}_j\}$ that depend on the actual beam offsets can be according to Equation (5.15), Equation (5.16), Equation (5.17), and Equation (5.18) calculated as

$$\mathrm{E}\{\tilde{x}_i^2\} = E\{x_i^2\} - \sigma^2 \approx \sum_{k=1}^{K} x_i(k)^2 - \sigma^2, \tag{5.29}$$

$$\mathrm{E}\{\tilde{y}_i^2\} = E\{y_i^2\} - \sigma^2 \approx \sum_{k=1}^{K} y_i(k)^2 - \sigma^2, \tag{5.30}$$

$$\mathrm{E}\{\tilde{x}_i\tilde{x}_j\} = \mathrm{E}\{x_i x_j\} \approx \sum_{k=1}^{K} x_i(k)x_j(k), \tag{5.31}$$

$$\mathrm{E}\{\tilde{y}_i\tilde{y}_j\} = \mathrm{E}\{y_i y_j\} \approx \sum_{k=1}^{K} y_i(k)y_j(k), \tag{5.32}$$

Thus, all the elements of the noise covariance matrix $\mathbf{R_{ZZ}}$ for the model polynomial terms up to the second order are stated in the above equations. The other corresponding elements of the noise covariance matrix for higher order polynomial terms can be calculated in a similar way as above.

5.3.2 Total Least Squares Estimation

After calculating the noise covariance matrix, the model parameters in the matrix $\beta_{\mathtt{TLS,p}}$ can be estimated by means of the TLS approach. Define

$$\mathbf{C_p} = [\mathbf{X_p}\ \mathbf{Y}], \tag{5.33}$$

where

$$\mathbf{X_p} = \mathbf{X}\ \mathbf{R_{ZZ}}^{-\frac{1}{2}}. \tag{5.34}$$

Let $\mathbf{C_p} = \mathbf{U\Sigma V}^T$ be the singular value decomposition of of $\mathbf{C_p}$ defined in Equation (5.33), where $\mathbf{\Sigma} = \mathtt{diag}(\sigma_1, \cdots, \sigma_{T+2})$ with $\sigma_1 \geq \cdots \geq \sigma_{T+2}$ are the singular values of $\mathbf{C}_p$. The TLS solution with the preprocessed data can be written as follows [80, 81]

$$\hat{\beta}_{\mathtt{TLS,p}} = -\mathbf{V}_{(1:T,T+1:T+2)}\mathbf{V}_{(T+1:T+2,T+1:T+2)}{}^{-1}. \tag{5.35}$$

The corresponding TLS residuals estimate is given by

$$\mathbf{\Delta C}_{\mathtt{TLS,p}} = [\Delta\mathbf{X_p}\ \Delta\mathbf{Y}] = -\mathbf{U}diag(0, \cdots, 0, \sigma_{T+1}, \sigma_{T+2})\mathbf{V}^T. \tag{5.36}$$

Thus, the estimate of the actual parameters is given by

$$\hat{\beta}_{\mathtt{TLS}} = \mathbf{R}_{\mathbf{ZZ}}^{-\frac{1}{2}}\ \hat{\beta}_{\mathtt{TLS,p}}. \tag{5.37}$$

Assuming known linear optics along the path of interest of the particle accelerator optics, i.e., between $\mathrm{BPM}_{\mathtt{i1}}$ and $\mathrm{BPM}_{\mathtt{i3}}$, the strength and location of the non-linear components can be determined through exhaustive search to fit the estimated parameters.

5.4 Optics Error Order Detection

The task of determining the existing orders in the optics model in Equation (5.4) that depend on the optics linear and non-linear components is very fundamental. Without the knowledge of the existing polynomial orders, the measured beam offset data will fit better with increasing number of model polynomial terms, i.e., $X_{ijkl} = x_{i1}(t)^i x_{i2}(t)^j y_{i1}(t)^k y_{i2}(t)^l$. This leads however to the so called over-fitting and deteriorating the estimation of the true optics model parameters, since the noise part in the measured data get fitted in the TLS parameter estimation when assuming a higher model complexity than the reality.

Define the hypothesis

$$\mathtt{H}_m:\ \ \alpha_{i_m j_m k_m l_m} = 0\ \ \mathtt{or}\ \ \lambda_{i_m j_m k_m l_m} = 0,\ \ m \leq M, \tag{5.38}$$

this is called the null hypothesis that states that the corresponding multivariate polynomial term does not exist with in the optics model equation. The complement of this hypothesis is then given by

$$\mathtt{H}'_m:\ \ \alpha_{i_m j_m k_m l_m} \neq 0\ \ \mathtt{or}\ \ \lambda_{i_m j_m k_m l_m} \neq 0,\ \ m \leq M. \tag{5.39}$$

The problem of optics model selection can be therefore stated as selecting or rejecting the hypotheses $\mathtt{H}_m$ over all possible polynomial terms of interest. Thus, all pairs of hypotheses $\mathtt{H}_m$ and their complements $\mathtt{H}'_m$ must be evaluated against each other. The individual tests of the hypotheses pairs can be made conservative in order to cope with the multiplicity dilemma and control the Family Wise Error (FWE), which is generally defined as the probability of rejecting any true null hypothesis. This procedure is called Simultaneous Test Procedure (STP) [82, 83].

The STP has been applied to several applications of statistical signal processing. The implementation of STP in multiband spectrum sensing for cognitive radio has been addressed in [84]. In [85], STP procedure has been applied to source enumeration. The determination of optimal sensor location has been addressed in [86] using STP. The application of STP in distributed detection has been addressed in [87, 88].

A very important concept in the hypothesis testing is the p-value, which is defined as the probability that the test statistic can have its observed value or greater when there is no causal basis, i.e., when the null hypothesis is true. The null hypothesis is usually rejected when the corresponding p-value for the observed test statistic is less than some significance level, e.g., 0.005 [89]. The problem when having multiple testing is that the multiplicity adjusted p-value can be much greater than the p-value of the single pair hypothesis testing problem [83]. Therefore, there are many multiple testing procedures that solve the multiplicity problem by making the tests of the individual hypotheses pairs more conservative [83, 84]. Thus, with the STP procedures an overall model control is provided instead of controlling the individual optics polynomial terms.

5.4.1 Adjusted P-Value

Usually it is possible to calculate an adjusted p-value for each test of every null hypothesis $\mathtt{H}_m$ versus its complement $\mathtt{H}'_m$ that counts for multiplicity. The adjusted p-value is set such that the decision to reject the null hypothesis is obtained with FWE = α. The mathematical definition of an adjusted p-value for some hypotheses pair testing, $\tilde{p}_m$, can be stated as [83]

$$\tilde{p}_m = inf\{\alpha \mid \mathtt{H}_m \texttt{ is rejected at FWE = } \alpha\}. \tag{5.40}$$

This is the smallest significance level for rejecting the hypothesis $\mathtt{H}_m$ with a multiple (simultaneous) test procedure.

The adjusted p-value is always greater than the observed value. If the joint distribution of the p-values for the hypotheses pairs is known, one can calculate a single step adjusted p-value as [83]

$$\tilde{p}_m = Pr(\min_{n \leq M} P_n \leq p_m \mid \mathtt{H}_0^C), \tag{5.41}$$

where $\mathtt{H}_0^C$ represents the case when all the null hypotheses $\mathtt{H}_m$, $m \leq M$ are true. This is the so called FWEC in contrast to the FWEP that is calculated under partial set of null hypotheses.

In [90], another approach has been addressed to solve the multiplicity problem via controlling the False Discovery Rate (FDR), which is defined as the proportion of falsely rejected null hypotheses among all rejected null hypotheses. This kind of multiple testing is less conservative than the FWE controlling testing, and has thus more testing power.

For evaluating the performance of the model selection procedure, there are several metrics. The Familywise Miss Detection (FWM) is defined as the probability of declaring at least one truly existing polynomial term as non-existing, i.e., accepting at least one null hypothesis when its complement hypothesis is true. The False Alarm Ratio (FAR) is defined as the ratio of falsely rejected true null hypotheses among all true null hypotheses.

5.4.2 False Discovery Rate Controlling Adjusted P-Value

Benjamini and Hochberg have developed a new multiple testing procedure that controls the FDR [82, 90]. In general, when some complement hypotheses are true, i.e., their corresponding polynomial terms exist in the optics model, the FDR is smaller or equal to the FWE [84]. This means that controlling the FWE leads to controlling the FDR. Therefore, controlling the FDR is less conservative than controlling the FWE. Thus, the test procedures that control the FDR have more power.

The Benjamini-Hochberg Procedure (BHP) starts with ordering the p-values $p_{i_1} \leq \cdots \leq p_{i_m} \leq \cdots \leq p_{i_M}$ for the null hypotheses $\mathtt{H}_{i_1}, \cdots, \mathtt{H}_{i_m}, \cdots, \mathtt{H}_{i_M}$. Subsequently, it calculates the maximal index such that

$$m_{max} = \max\left(1 \leq m \leq M : \; p_{i_m} \leq \frac{m\alpha}{M}\right). \tag{5.42}$$

Thus, the null hypotheses $\mathtt{H}_{i_1}, \cdots, \mathtt{H}_{i_{mmax}}$ must be rejected, and their complement hypotheses declared true, where the rest are accepted null hypotheses.

This BHP controls the FDR at level α when all null hypotheses are true. This gives in general more testing power than the methods controlling the FWE. The testing power of the BHP can however be very low, when many null hypotheses are not true. Therefore, an Adaptive Benjamini-Hochberg Procedure (A-BHP) has been addressed in order to improve the testing power when some null hypotheses are false [82, 90]. This algorithm is composed of two main steps. The first step is to estimates the current configuration of true/false hypotheses, and thus the number of the true null

hypotheses. Then, it proceeds with the original simultaneous testing of the BHP using the estimated number of the true null hypotheses M_0.

The estimate of the number of true null hypotheses can be written as [82, 90, 91]

$$\hat{M}_0 = \min\left[\left\lceil \frac{1}{S_{m_0+1}} \right\rceil, M\right], \tag{5.43}$$

where

$$S_m = \frac{1 - p_{i_m}}{M + 1 - m}, \tag{5.44}$$

with m_0 is the first index starting from $m = 1$ and up that fulfills $S_{m+1} < S_m$. Thus, the A-BHP can be summarized as in Algorithm 1 [82, 90, 91]

Algorithm 1: Adaptive Benjamini-Hochberg Procedure

1 Calculate the p-values for the hypotheses $\mathtt{H}_m$, $1 \leq m \leq M$;
2 Order the p-values $p_{i_1} \leq \cdots \leq p_{i_m} \leq \cdots \leq p_{i_M}$ for the null hypotheses $\mathtt{H}_{i_1}, \cdots, \mathtt{H}_{i_m}, \cdots, \mathtt{H}_{i_M}$;
3 If the condition $p_{i_m} \geq \frac{m\alpha}{M}$ is fulfilled by all p-values, all null hypotheses are accepted. Otherwise, continue with the following steps;
4 Estimate the number of true null hypotheses $\hat{M}_0$ according to Equation (5.43);
5 Starting with p_{i_M} and down, find the first index m_f that does not fulfill the condition $p_{i_{m_f}} > \frac{m_f\alpha}{\hat{M}_0}$;
6 Reject all hypotheses $\mathtt{H}_{i_1}, \cdots, \mathtt{H}_{i_{m_f}}$, i.e., their corresponding polynomial terms exist within the optics model, and accept the rest;

5.4.3 Familywise Error Rate Controlling Adjusted P-Value

The simplest single step adjusted p-value approach without knowing the joint distribution of the p-values is the Bonferroni method, which rejects the hypothesis $\mathtt{H}_m$ and accept its complement $\mathtt{H}'_m$ when the p-value p_m is less than the significance level α/M, where $\mathtt{FWE} = \alpha$. This leads to the Bonferroni conservative single step adjusted p-value of [83, 92]

$$\tilde{p}_m = \min(Mp_m, 1). \tag{5.45}$$

Another related single step adjusted p-value method is the Sidak method, which rejects the hypothesis $\mathtt{H}_m$ when the observed p-value p_m is less than $1-(1-\alpha)^{1/M}$. This leads to the Sidak adjusted p-value that can be calculated based on the total number M of hypotheses pairs as [82, 83]

$$\tilde{p}_m = 1 - (1 - p_m)^M. \tag{5.46}$$

The Sidak adjusted p-value leads to an exact value of the FWE assuming all null hypotheses $\mathtt{H}_m$, $m \leq M$ are true when the p-values are independently and uniformly distributed [83,93]. Nevertheless, the aforementioned Bonferroni and Sidak single step adjusted p-value methods become very conservative when the p-values of the hypotheses pairs are highly correlated with each others. In the extreme case when the p-values of the hypotheses pairs are perfectly correlated, i.e., completely depend on each other, the single step adjusted p-value in Equation (5.41) becomes [83]

$$\begin{aligned} \tilde{p}_m &= Pr(\min_{n \leq M} P_n \leq p_m \mid \mathtt{H}_0^C) \\ &= Pr(P_m \leq p_m \mid \mathtt{H}_0^C) = p_m. \end{aligned} \tag{5.47}$$

This gives a much smaller real adjusted p-value than the results of the Bonferroni and Sidak single step methods.

The adjusted p-values with the single step methods are basically calculated based on the minimum p-value distribution. These methods are able to keep the FWE controlled, but this is done with the price of less power of detecting the true complement hypotheses, which is defined as the probability of detecting true complement hypotheses. Intuitively, the minimum p-value distribution should be applied only on the minimum observed p-value. Thus, the power of detecting true complement hypotheses can be enhanced while keeping the FWE controlled [83].

5.4.3.1 Step-Down Adjusted P-Value

The step-down methods use the distribution of the minimum p-value to adjust only the minimum observed p-value. Subsequently, the minimum of the observed p-value of the remaining set of p-values is adjusted using the distribution of the minimum p-value of the remaining set. The p-values are thus adjusted according to always decreasing sets of p-values, which increase the power of detecting the true complement hypotheses [83,94,95].

The sequentially rejective algorithm by Holm based on the Bonferroni inequality starts with ordering the p-values $p_{i_1} \leq \cdots \leq p_{i_m} \leq \cdots \leq p_{i_M}$ for the null hypotheses $\mathtt{H}_{i_1}, \cdots, \mathtt{H}_{i_m}, \cdots, \mathtt{H}_{i_M}$. When the first null hypothesis $\mathtt{H}_{i_1}$ with the smallest p-value p_{i_1} has to be accepted, then all other null hypotheses have to be accepted as well. Otherwise, $\mathtt{H}_{i_1}$ is rejected, i.e., its complement hypothesis is accepted, and we continue with the same test for the subset of remaining $M-1$ hypotheses. If $\mathtt{H}_{i_2}$ has to be rejected based on its adjusted p-value within the smaller subset, we continue the test procedure with the smaller subset of remaining $M-2$ hypotheses, and so on and

so forth until all hypotheses pairs has been tested. This procedure is equivalent to adjusting the p-values for the single hypotheses pairs as following [83, 96–98]

$$\begin{aligned}
\tilde{p}_{i_1} &= \min\left(Mp_{i_1}, 1\right) \\
&\vdots \\
\tilde{p}_{i_m} &= \min\left(\max(\tilde{p}_{i_{m-1}}, (M-m+1)p_{i_m}), 1\right) \\
&\vdots \\
\tilde{p}_{i_M} &= \min\left(\max(\tilde{p}_{i_{M-1}}, p_{i_M}), 1\right).
\end{aligned} \tag{5.48}$$

The min function is to ensure that the adjusted p-values are less or equal to 1, where the max function is to ensure that the order of the adjusted p-values is the same as of the original observed p-values. The Sidak adjustment of the p-values within the subsets of the hypotheses can also be applied in the Equations (5.48) instead of the Bonferroni adjustment in order to get more powerful tests.

The previous Holm's algorithm stays conservative with the Bonferroni and the Sidak p-value adjustments within the subsets of hypotheses since the resulting adjusted p-values can still be too large. The p-value adjustments can be made less conservative, and thus the power of the test get increased by applying the original definition of the single step adjusted p-values in Equation (5.41) instead of the Bonferroni and the Sidak adjustments. Thus, the sequentially step-down adjusted p-values can be calculated more precisely as [83]

$$\begin{aligned}
\tilde{p}_{i_1} &= Pr(\min_{1\leq n\leq M} P_{i_n} \leq p_{i_1} \mid \mathtt{H}_0^C) \\
&\vdots \\
\tilde{p}_{i_m} &= \max\left(\tilde{p}_{i_{m-1}}, Pr(\min_{m\leq n\leq M} P_{i_n} \leq p_{(m)} \mid \mathtt{H}_0^C)\right) \\
&\vdots \\
\tilde{p}_{i_M} &= \max\left(\tilde{p}_{i_{M-1}}, Pr(P_{i_M} \leq p_{i_M} \mid \mathtt{H}_0^C)\right).
\end{aligned} \tag{5.49}$$

The max function is still applied here in order to ensure that the order of the adjusted p-values is the same as of the original observed p-values. Since the min is taken over always smaller sets of p-values, the resulting step-down adjusted p-values in Equations (5.49) are always smaller than the single step adjusted p-values in Equation (5.41). This is the reason for increasing the power of the tests using the step-down adjusted p-values.

5.4.4 Adjusted P-Value for Restricted Combinations

The hypotheses $\mathtt{H}_m$ with $1 \leq m \leq M$ can be dependent on each other, e.g., restricted with some combinations such that the truth or falsehood of some hypotheses implies the truth or falsehood of some others. In such a case, the aforementioned step-down adjusted p-values will still be able to protect the FWE. Nevertheless, they are then considered conservative as they do not incorporate the logical dependencies and restrictions of the hypotheses that can lead to smaller adjustment of the p-values, and thus increasing the power of the test procedure. This will happen also when controlling the FDR.

In our addressed optics model, the existence of some terms of the multivariate polynomial implies the existence of some other terms. This means that rejecting or accepting some hypothesis implies rejecting or accepting another set of hypotheses. For instance, the existence of coupling terms of the horizontal direction with the vertical direction that can be stemmed from magnets skewness or higher order magnetic field errors implies the existence of coupling terms of the vertical direction with the horizontal direction, and vice versa.

In [99], a procedure that incorporates combinations constraints has been addressed based on the Bonferroni adjustment. This procedure has been made less conservative to gain more power of the test using the Sidak adjustment in [100]. The dependence structures for the restricted combinations has been incorporated in [83] using a resampling method of the original distributions in order to have more precise calculated p-values based on the definition in Equation (5.41). The adjusted p-values restricted hypotheses combinations can be stated as [83]

$$\begin{aligned}
\tilde{p}_{i_1} &= Pr(\min_{1\leq n\leq M} P_{i_n} \leq p_{i_1} \mid \mathtt{H}_0^C) \\
&\vdots \\
\tilde{p}_{i_m} &= \max\left(\tilde{p}_{(m-1)}, \max_{K\in S_m}[Pr(\min_{n\in K} P_{(n)} \leq p_{(m)} \mid \mathtt{H}_0^C)]\right) \\
&\vdots \\
\tilde{p}_{i_M} &= \max\left(\tilde{p}_{i_{M-1}}, Pr(P_{i_M} \leq p_{i_M} \mid \mathtt{H}_0^C)\right),
\end{aligned} \tag{5.50}$$

where S_m, $1 \leq m \leq M$ are defined as the groups of sets of hypotheses including $\mathtt{H}_m$ that can be true at the stage m of the test, when all previously tested hypotheses are

false, i.e.,

$$\begin{aligned} S_1 &= S \\ &\vdots \\ S_m &= \left\{ K \subset S \mid r_m \in K, \ \texttt{and} \ (\underset{n\in K}{\cap} \mathtt{H}_n) \bigcap (\underset{1\le l\le m-1}{\cap} \mathtt{H}'_{r_l}) \neq \emptyset \right\} \\ &\vdots \\ S_M &= \{\{r_M\}\}, \end{aligned} \tag{5.51}$$

with $S = \{1, \cdots, m, \cdots, M\}$. If the resulting set from Equation (5.51) for some value m is empty, we take $S_m = \{\{r_m\}\}$ [83].

In this work, we address the restricted hypotheses combinations by considering the test statistics Tb_r for the collections B_r, $1 \le r \le R$ of hypotheses that can be either true or false together. A collection B_r can be for instance the hypotheses corresponding to the polynomial terms of the $x - y$ and $y - x$ couplings, or the polynomial terms of second order resulting from a sextupolar element. We define the test statistics as

$$Tb_r = \sum_{m\in B_r} \hat{\beta}^2_{\mathtt{H}_m}, \tag{5.52}$$

where $\hat{\beta}_{\mathtt{H}_m}$ denotes the estimated polynomial coefficient corresponding to the hypothesis $\mathtt{H}_m$.

The single tests are performed such that all the null hypotheses $\mathtt{H}_m$, $m \in B_r$ are declared to be false together, and their complements are accepted if

$$Tb_r \ge t_r. \tag{5.53}$$

Otherwise, they are accepted, and the corresponding polynomial terms are declared as not included in the optics model polynomial.

The decision thresholds for the single tests t_r are set such that their corresponding p-values are less than the given significance level α, i.e.,

$$p_r \le \alpha. \tag{5.54}$$

The aforementioned multiple testing procedures that control the FWE, as well as the FDR must be applied in the case of restricted combinations on the p-values of the R hypotheses collections B_r defined as

$$p_r = Pr(Tb_r \ge Tb_{r,ob} \mid \texttt{all} \ \mathtt{H}_m, \ m \in B_r \ \texttt{are true}), \ 1 \le r \le R, \tag{5.55}$$

where $Tb_{r,ob}$ denote the observed values of the test statistics defined in Equation (5.52).

5.4.5 Bootstrap Adjusted P-Value

The calculation of the p-values for the single hypotheses pairs, as well as the multiplicity adjusted p-values requires the knowledge of the probability distributions for the estimated optics polynomial model parameters. For this purpose, the asymptotic distributions of the TLS parameter estimates using enough number of measured samples can ideally be considered. Under some mild conditions, the TLS estimator has asymptotically a zero mean multivariate normal distribution [101]. The covariance matrix of the resulting asymptotic distribution has a known form in the literature, if the moments up to the fourth order of the rows of the errors matrix are of the same form of a normal distribution [101, 102]. The covariance matrix formula in this case depends on the true values of the parameters in β, which could be replaced here with their consistent TLS estimates.

In our application however, the moments up to the fourth order of the rows of the errors matrix are not of the same form of a normal distribution. The formula for the covariance matrix of the asymptotic distribution gets therefore complicated, and it is not feasible to be calculated. Thus, generic techniques such as bootstrap techniques remain as possible ways to estimate the probability distributions for the estimates of optics model parameters.

The bootstrap is a computer intensive method for statistical inference using the available data without knowing the population distribution. Let $\mathbf{C} = [\mathbf{X}\ \mathbf{Y}]$. The non-parametric bootstrap procedure to find the empirical distribution of a parameter $\hat{\beta}_{ij} = (\beta_{\text{TLS}})_{(ij)}$ is given as in Algorithm 2 [102–104].

Algorithm 2: Non-parametric bootstrap

1 Calculate $\hat{\beta}_{ij}$ based on $\mathbf{C}$;
2 **for** $k = 1$ **to** K^* **do**
3 Construct $\mathbf{C}^{*(k)} \in \mathcal{R}^{K\times(T+2)}$ by resampling with replacement from the rows of $\mathbf{C}$;
4 Recalculate $\hat{\beta}_{ij}^{*(k)}$ based on $\mathbf{C}^{*(k)}$;
5 Calculate the histogram of the values $\hat{\beta}_{ij}^{*(k)}$;

Thus, the bootstrap probability of $\hat{\beta}_{ij}$ to be in the interval $[a, b]$ is

$$Pr^*(a \leq \hat{\beta}_{ij} \leq b) = \frac{\#(a \leq \hat{\beta}_{ij}^{*(k)} \leq b)}{K^*}, \tag{5.56}$$

where $\#(a \leq \hat{\beta}_{ij}^{*(k)} \leq b)$ denotes the number of bootstrap realizations $\hat{\beta}_{ij}^{*(k)}$ that lie in the interval $[a, b]$.

The asymptotic consistency of the non-parametric bootstrap procedure for the TLS estimator has been already shown in [102].

Let's consider as an example an accelerator section with 3 BPMs containing a sextupolar magnet error in vertical direction with a magnetic field of the form $\overrightarrow{B}_y = k(x^2 - y^2)\overrightarrow{e}_y$. Furthermore, we consider skewed magnets such that lead coupling between the horizontal and vertical beam oscillations. Thus, the beam offset relation polynomial for the horizontal beam oscillation of this scenario at BPM_3 can be written with respect to the beam offsets at the other BPMs of the given section in the form

$$x_3 = \lambda_1 x_1 + \lambda_2 x_2 + \lambda_3 {x_1}^2 + \lambda_4 {x_2}^2 + \lambda_5 x_1 x_2 + \lambda_6 {y_1}^2 + \lambda_7 {y_2}^2 + \lambda_8 y_1 y_2 + \lambda_9 y_1 + \lambda_{10} x_y. \quad (5.57)$$

Figure 5.2 shows the real distribution of the model parameters estimated by Monte-Carlo simulations (solid lines), and the bootstrap distribution of the estimation of the model parameters. One can notice from the figure that the bootstrap distributions of the estimation of the model parameters match very well to the corresponding Monte-Carlo distributions.

Since the p-values and the thresholds of the test statistics are calculated under the true null hypotheses, the distributions of the test statistics under the null hypotheses must be reconstructed. The bootstrap distribution of the test statistic Tb_r for the collection B_r, $1 \leq r \leq R$ under the null hypotheses can be constructed as in Algorithm 3, which is similar to the algorithm stated in Table 3.3 in [103].

Thus, the bootstrap p-value for the collection B_r can be calculated using the result of Algorithm 3 as the proportion of bootstrap test statistic values that are greater than the observed value of the test statistic for the original data set, i.e.,

$$p_r = \frac{\#(Tb_r^{*(k)} \geq Tb_{r,ob})}{K^*}, \quad (5.58)$$

where $Tb_{r,ob}$ denotes the observed value of the test statistic.

5.5 Confidence Intervals

After selecting the proper optics model and the existing multivariate polynomial terms, the parameters of the selected model can be estimated with better quality since over-fitting is avoided with estimating the true model. A very important aspect of the parameter estimates is their reliability. Since the parameter estimation is applied

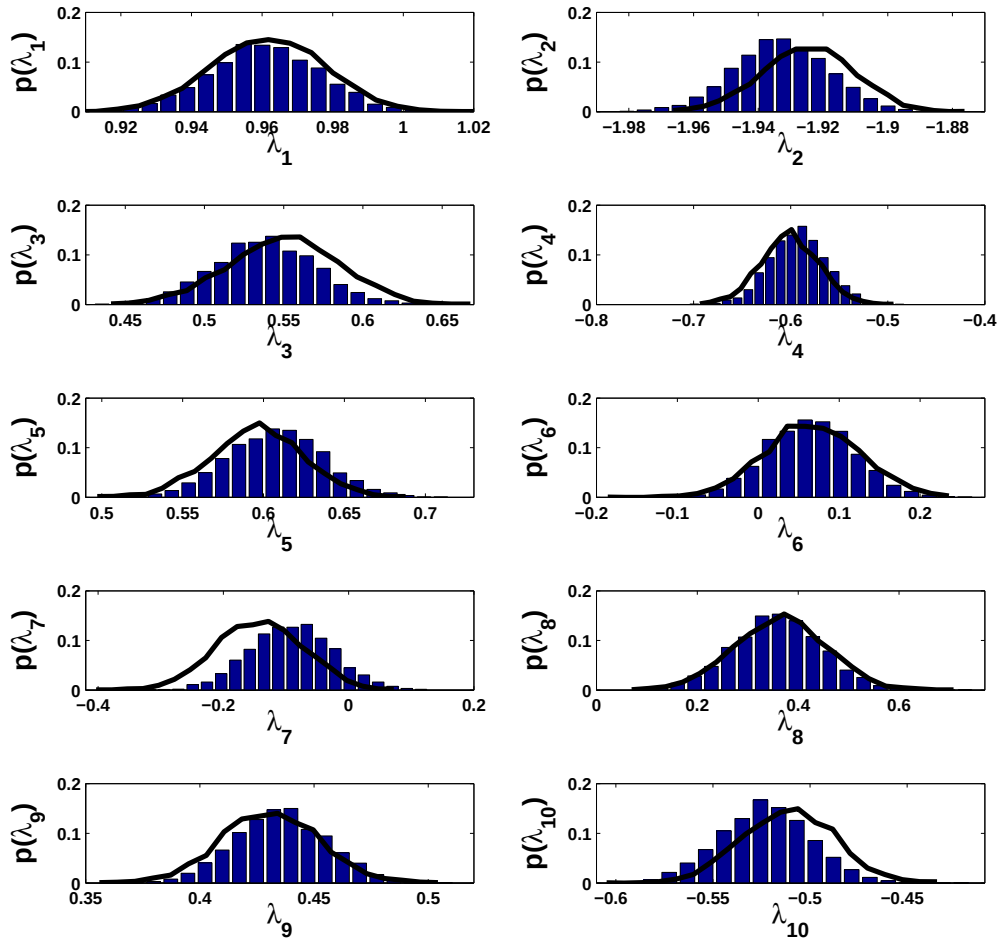

Figure 5.2. Bootstrap and Monte-Carlo estimated parameter distributions.

on noisy measurements of the beam offsets, the resulting estimates will be noisy as well. Therefore, one is interested in knowing how far the estimates are affected by the measurement noise.

Confidence intervals, which give interval estimates of the parameters, are very good indication of the parameter estimates reliability. They establish some statistical confidence for the parameters of interest [103]. A confidence interval of some parameter consists of two bounds, where the true value of the parameter lies between these bounds with a specified probability.

Similar to the hypotheses testing, the asymptotic distribution of the estimates can ideally be used to determine confidence intervals. However, the formula for the covari-

Algorithm 3: Bootstrap under null hypotheses

1 Calculate $\mathbf{C_p}$ according to Equation (5.33);
2 Calculate the residuals $\mathbf{\Delta C}_{\mathtt{TLS,p}}$ according to Equation (5.36);
3 Calculate the centered residuals by subtracting the mean value, i.e., $\mathbf{\Delta}\hat{\mathbf{C}}_{\mathtt{TLS,p}} = \mathbf{\Delta C}_{\mathtt{TLS,p}} - \mathbf{\Delta}\bar{\mathbf{C}}_{\mathtt{TLS,p}}$;
4 Calculate $\hat{\mathbf{C}}_{\mathbf{p}} = [\hat{\mathbf{X}}_{\mathbf{p}}\ \hat{\mathbf{Y}}] = \mathbf{C_p} - \mathbf{\Delta C}_{\mathtt{TLS,p}}$;
5 Calculate $\hat{\beta}^r_{\mathtt{TLS,p}} = \mathbf{R}^{\frac{1}{2}}_{\mathbf{ZZ}}\hat{\beta}^r_{\mathtt{TLS}}$, where $\hat{\beta}^r_{\mathtt{TLS}}$ denotes the parameter estimates from Equation (5.37) with setting the corresponding parameters of the collection B_r to zero;
6 **for** $k = 1$ **to** K^* **do**
7 Construct $\mathbf{\Delta}\hat{\mathbf{C}}^{*(k)}_{\mathtt{TLS,p}} = [\Delta\mathbf{X_p}^{*(k)}\ \Delta\mathbf{Y}^{*(k)}] \in \mathcal{R}^{K\times(T+2)}$ by resampling with replacement from the rows of $\mathbf{\Delta}\hat{\mathbf{C}}_{\mathtt{TLS,p}}$;
8 Calculate $\mathbf{Y}^{*(k)} = \hat{\beta}^r_{\mathtt{TLS,p}}\hat{\mathbf{X}}_{\mathbf{p}} + \Delta\mathbf{Y}^{*(k)}$;
9 Calculate $\mathbf{X_p}^{*(k)} = \hat{\mathbf{X}}_{\mathbf{p}} + \Delta\mathbf{X_p}^{*(k)}$;
10 Calculate $\hat{\beta}^{*(k)}_{\mathtt{TLS,p}}$ by applying the TLS estimator on $\mathbf{C}^{*(k)}_{\mathtt{TLS,p}} = [\mathbf{X_p}^{*(k)}\ \mathbf{Y}^{*(k)}]$;
11 Calculate $\hat{\beta}^{*(k)}_{\mathtt{TLS}} = \mathbf{R}^{-\frac{1}{2}}_{\mathbf{ZZ}}\hat{\beta}^{*(k)}_{\mathtt{TLS,p}}$;
12 Calculate the test statistic$Tb^{*(k)}_r$ for $\hat{\beta}^{*(k)}_{\mathtt{TLS}}$ according to Equation (5.52);
13 Calculate the histogram of the values $Tb^{*(k)}_r$;

ance matrix of the asymptotic distribution is complicated, and cannot be calculated as already mentioned before. Thus, bootstrap techniques remain as possible ways to calculate confidence intervals for the model parameters.

5.5.1 Bootstrap Confidence Intervals

Let $\mathbf{C} = [\mathbf{X}\ \mathbf{Y}]$. The non-parametric bootstrap procedure to find the empirical confidence interval with confidence probability $1-\alpha$ of a parameter $\hat{\beta}_{ij} = (\beta_{\mathtt{TLS}})_{(ij)}$ is given in Algorithm 4 [102–104].

The strength of the bootstrap comes from its ability for statistical inference even in complicated situations, as well as its higher accuracy compared to the normal approximation approach [104]. Higher order accuracy of the bootstrap can be achieved by dealing the studentized distribution of the estimators [103, 104]. This bootstrap technique is called percentile-t bootstrap, and can be performed as in Algorithm 5 [103,104].

Furthermore, the bootstrap technique can be performed on the parametric model of the data in a similar way as in Algorithm 3. In this case, the residuals and the es-

Algorithm 4: Non-parametric bootstrap confidence interval

Calculate $\hat{\beta}_{ij}$ based on $\mathbf{C}$;
for $k = 1$ **to** K^* **do**
    construct $\mathbf{C}^{*(k)} \in \mathcal{R}^{K\times(T+2)}$ by resampling with replacement from the rows of $\mathbf{C}$;
    recalculate $\hat{\beta}_{ij}^{*(k)}$ based on $\mathbf{C}^{*(k)}$;
sort the items $\hat{\beta}_{ij}^{*(k)}$ into an increasing order such that $\hat{\beta}_{ij}^{*(1)} \leq \cdots \leq \hat{\beta}_{ij}^{*(K)}$;
Calculate $q_1 = \lfloor K^* \frac{\alpha}{2} \rfloor$;
Calculate $q_2 = K^* - q_1 + 1$;
The desired confidence interval is $(\hat{\beta}_{ij}^{*(q_1)}, \hat{\beta}_{ij}^{*(q_2)})$;

Algorithm 5: Percentile-t bootstrap confidence interval

Calculate $\hat{\beta}_{ij}$ based on $\mathbf{C}$;
calculate $\sigma_{\hat{\beta}_{ij}}$ using bootstrap;
for $k = 1$ **to** K^* **do**
    construct $\mathbf{C}^{*(k)} \in \mathcal{R}^{K\times(T+2)}$ by resampling with replacement from the rows of $\mathbf{C}$;
    recalculate $\hat{\beta}_{ij}^{*(k)}$ based on $\mathbf{C}^{*(k)}$;
    calculate $\sigma_{\hat{\beta}_{ij}^{*(k)}}$ using nested bootstrap;
    calculate $\beta_{\gamma}^{*(k)} = \frac{\hat{\beta}_{ij}^{*(k)} - \hat{\beta}_{ij}}{\sigma_{\hat{\beta}_{ij}^{*(k)}}}$;
sort the items $\beta_{\gamma}^{*(k)}$ into an increasing order such that $\beta_{\gamma}^{*(1)} \leq \cdots \leq \beta_{\gamma}^{*(K)}$;
Calculate $q_1 = \lfloor K^* \frac{\alpha}{2} \rfloor$;
Calculate $q_2 = K^* - q_1 + 1$;
The percentile-t confidence interval is $(\hat{\beta}_{ij} - \sigma_{\hat{\beta}_{ij}}\beta_{\gamma}^{*(q_2)}, \hat{\beta}_{ij} - \sigma_{\hat{\beta}_{ij}}\beta_{\gamma}^{*(q_1)})$;

timated beam offset data for the TLS estimator could be calculated using Equation (5.36) similar to [105]. Subsequently, one could add the corresponding resamples with replacement from the residuals to the estimated beam offsets, and proceed with constructing new matrices $\mathbf{X}$ and $\mathbf{Y}$ as defined in Equation (5.7) and Equation (5.6) and solving the model described in Equation (5.5). The confidence interval can be thus calculated by repeating the previous steps many times.

5.6 Results

An accelerator section with 3 BPMs containing a sextupolar magnet error in vertical direction with a magnetic field of the form $\overrightarrow{B}_y = k(x^2 - y^2)\overrightarrow{e}_y$ is considered in

our results. We first generate simulated measurements of the beam oscillations with sextupolar magnet error in vertical direction without linear coupling between the horizontal and vertical beam oscillations.

Furthermore, we consider real measurements taken at the heavy ions synchrotron SIS 18 at the GSI in Darmstadt. The chromaticity correcting sextupolar magnets were turned on while taking the measurements. One of the sextupolar magnets was located between BPM_2 and BPM_3, and no one between BPM_1 and BPM_2.

5.6.1 Simulated Data

An accelerator section with 3 BPMs containing a sextupolar magnet error with a magnetic field of the form in vertical direction $\overrightarrow{B}_y = k(x^2 - y^2)\overrightarrow{e}_y$ is considered. Thus, the beam offset relation polynomial for the horizontal beam oscillation of this scenario at BPM_3 can be written with respect to the beam offsets at the other BPMs of the given section in the form

$$x_3 = \lambda_1 x_1 + \lambda_2 x_2 + \lambda_3 {x_1}^2 + \lambda_4 {x_2}^2 + \lambda_5 x_1 x_2 + \lambda_6 {y_1}^2 + \lambda_7 {y_2}^2 + \lambda_8 y_1 y_2 + \lambda_9 y_1 + \lambda_{10} x_y, \quad (5.59)$$

where

$$\lambda_9 = \lambda_{10} = 0. \quad (5.60)$$

The parameters of the beam offset relation polynomial for the horizontal beam oscillation are listed in Table 5.1.

Table 5.1. Optics model polynomial coefficients.

Coef.	λ_1	λ_2	λ_3	λ_4	λ_5	λ_6	λ_7	λ_8
Value	1	-2	0.18	-0.21	0.21	0.03	-0.03	0.12

We have generated data for a one bunch beam oscillating over 1500 turns considering the model polynomial with horizontal and vertical tunes of 0.29 and 0.19, respectively. We considered the oscillations at the BPM_1 and BPM_2 with amplitudes of 1. The measurement additive noise standard deviation was 0.15 in our simulations, which is a realistic value.

Two hypotheses collections are considered in this simulated example. The first collection is composed of the hypotheses corresponding to the second order terms with the

coefficients $\{\lambda_3,\ \lambda_4, \cdots,\ \lambda_8\}$. Thus, the corresponding test statistic can be calculated as

$$Tb_1 = \sum_{m=3}^{8} \hat{\lambda}_m^2. \tag{5.61}$$

The second collection is composed of the hypotheses corresponding to the coupling terms with the coefficients $\{\lambda_9,\ \lambda_{10}\}$. Thus, the corresponding test statistic can be calculated as

$$Tb_2 = \sum_{m=9}^{10} \hat{\lambda}_m^2. \tag{5.62}$$

Figure 5.3 and Figure 5.4 show the bootstrap (bars), as well as the Monte-Carlo estimated (solid lines) distributions of the test statistics for the second order terms and coupling terms under the corresponding null hypotheses, respectively. The figures show a very good matching between the Monte-Carlo estimated, and the bootstrap distributions.

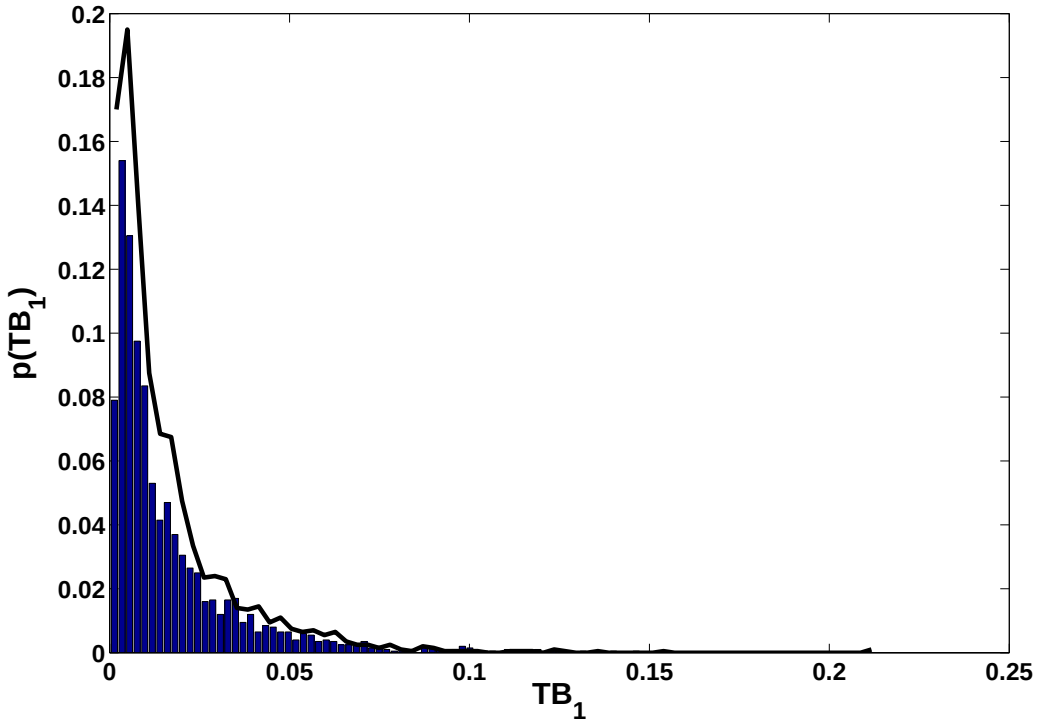

Figure 5.3. Bootstrap and Monte-Carlo estimated distribution of the second order terms test statistic.

These bootstrap distributions are used to calculate the p-values. For adjusting the multiple testing p-values, we applied the Adaptive Benjamini-Hochberg Procedure in

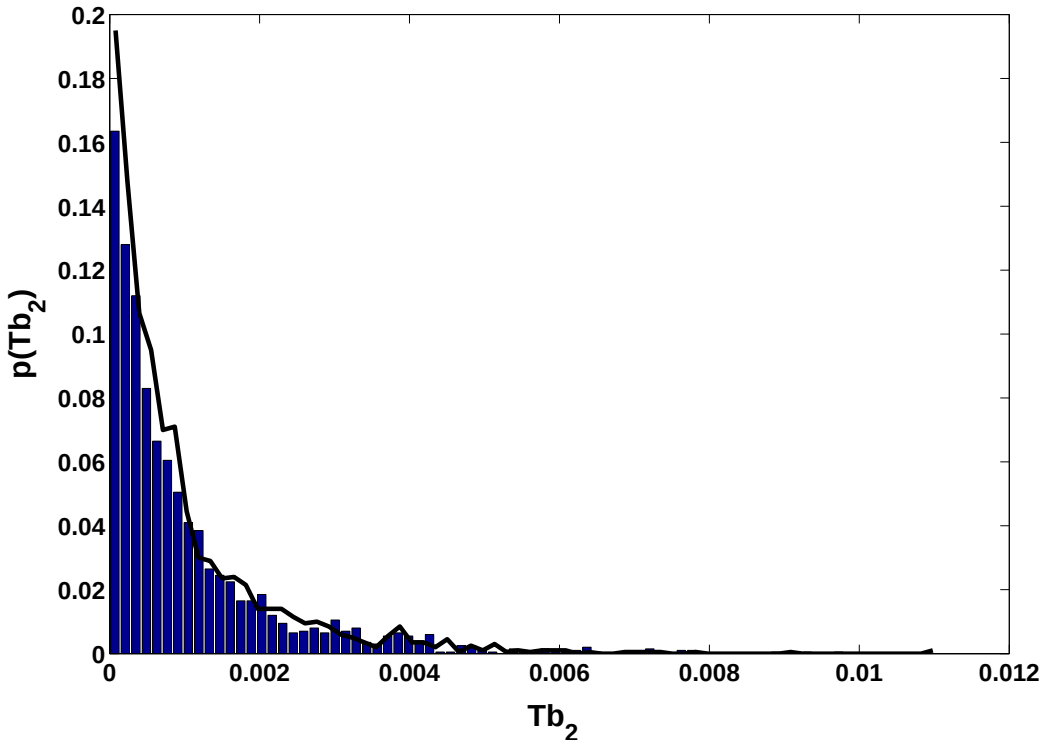

Figure 5.4. Bootstrap and Monte-Carlo estimated distribution of the coupling terms test statistic.

Algorithm 1 since it is less conservative than the FWE controlling algorithms, which gives more testing power.

Figure 5.5 depicts the familywise miss detection (FWM) for different values of the significance level α. The false alarm ratio (FAR) in terms of the significance level is depicted in Figure 5.6. The parameter estimation was based on 1000 data points for each realization. As one can notice from the figures, there is a trade-off between the FWM and the FAR, which is an expected result. Both error factor are very important for better optics errors determination. Therefore, a proper significance level must be chosen such that both of the FWM and the FAR have reasonable values. For the given scenario, the value of the significance level $\alpha = 0.03$ is a good choice since it holds both of the FWM and the FAR less than 5%.

The GTLS parameter estimation gets more precise for higher amplitudes of the beam oscillation signals, even with the same SNR values. The reason for this is that higher amplitudes lead to larger intervals covered by the measurements, which gives a better potential to fit the model. In the extreme case when the amplitudes are very small, the measured data will correspond to almost only one point, and become not enough

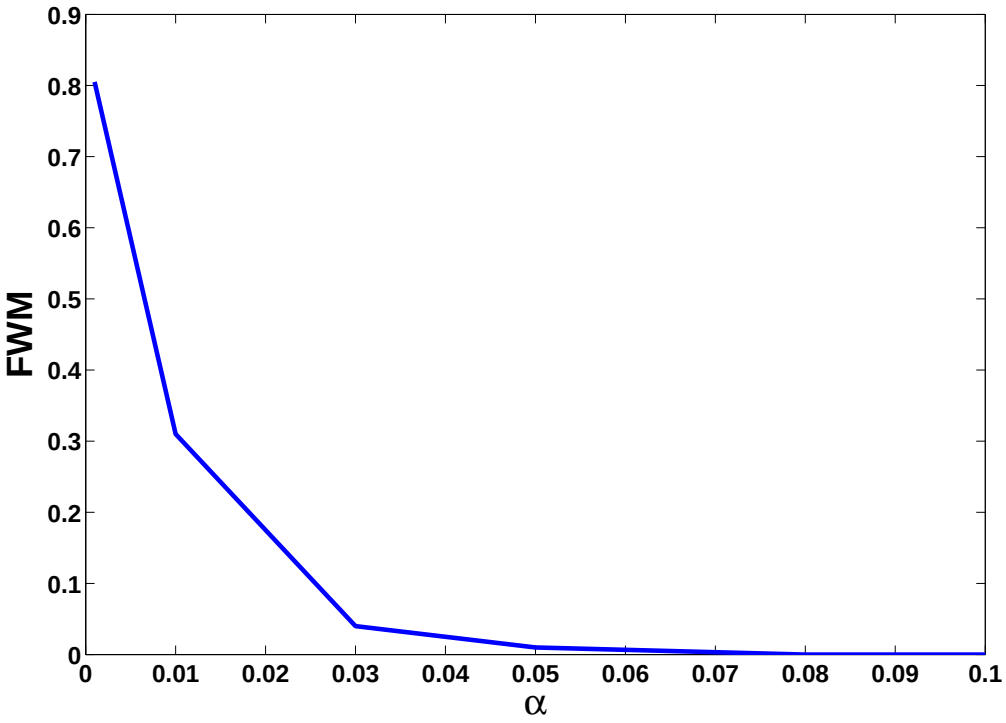

Figure 5.5. Familywise miss detection in terms of the significance level.

to fit the model even with higher number of measurements that only lead to reducing the impact of the noise, but does not give extra information about the model to be fitted.

In Figure 5.7, we show the 95% confidence interval estimates for the model parameters using non-parametric bootstrap described in Algorithm 4. The measurement noise standard deviation was taken 0.6, and the oscillation signal amplitudes 4, which keeps the same SNR value as in the previous simulations.

The coverage rates of the true model parameter values of the 95% and 97% confidence intervals have been estimated using 1000 independent realizations. The resulting coverage rates listed in Table 5.2 show a very good agreement with the given nominal confidence probabilities.

The results in Fig. 5.7 can be used to determine the strength and location of the sextupolar magnet error using an exhaustive search optimization due to the non-convexity. The parameters with a tighter confidence intervals can be given more weights in the search objective function since they are less affected by the measurement noise, more reliable, and have higher accuracy.

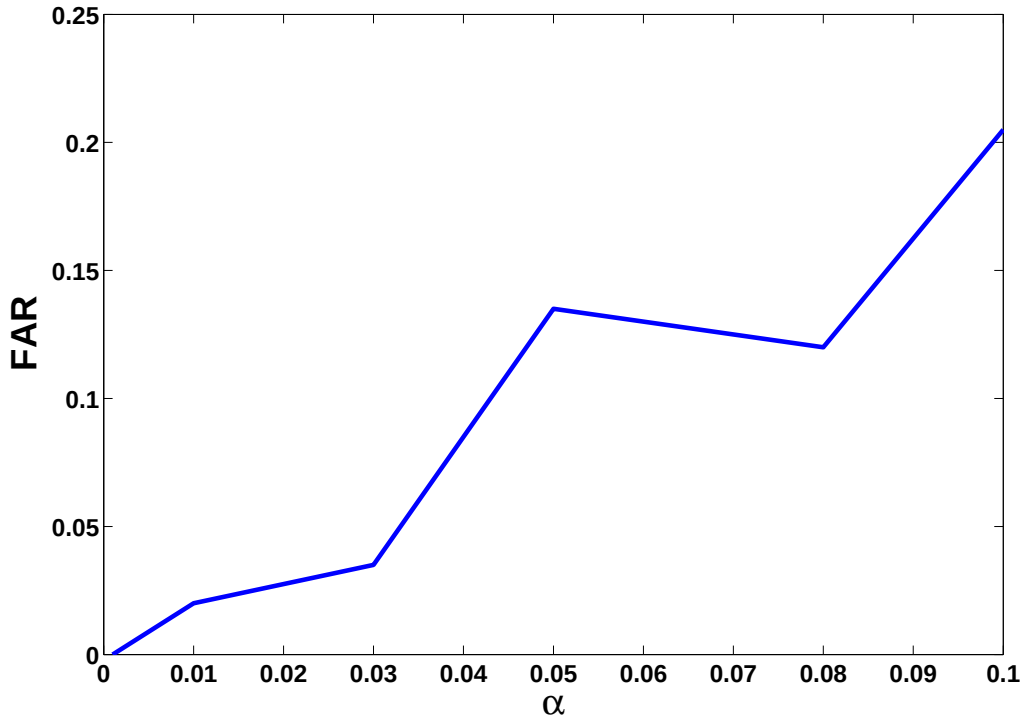

Figure 5.6. False alarm ratio in terms of the significance level.

Table 5.2. Confidence intervals coverage.

Coef.	λ_1	λ_2	λ_3	λ_4	λ_5	λ_6	λ_7	λ_8
True Value	1	-2	0.18	-0.21	0.21	0.03	-0.03	0.12
Coverage of 95% COnfidence Interval	96.3%	94.3%	97.0%	96.9%	95.2%	96.3%	96.1%	95.9%
Coverage of 97% Confidence Interval	98.3%	96.4%	97.5%	97.4%	97.4%	97.6%	97.7%	97.8%

5.6.2 Real Data

We apply here our approaches for the model selection and parameter estimation on real measurements taken at the heavy ions synchrotron SIS 18 at the GSI in Darmstadt. Thanks to the department of the beam diagnostics at the GSI for providing the measured data. The chromaticity correcting sextupolar magnets were turned on while taking the measurements. One of the sextupolar magnets was located between BPM_2 and BPM_3, and no one between BPM_1 and BPM_2.

Like with the simulated data, we applied our bootstrap hypotheses testing approach under the null hypotheses described in Algorithm 3 on the hypotheses collection corresponding to the second order terms with the coefficients $\{\lambda_3,\ \lambda_4, \cdots,\ \lambda_8\}$, as well

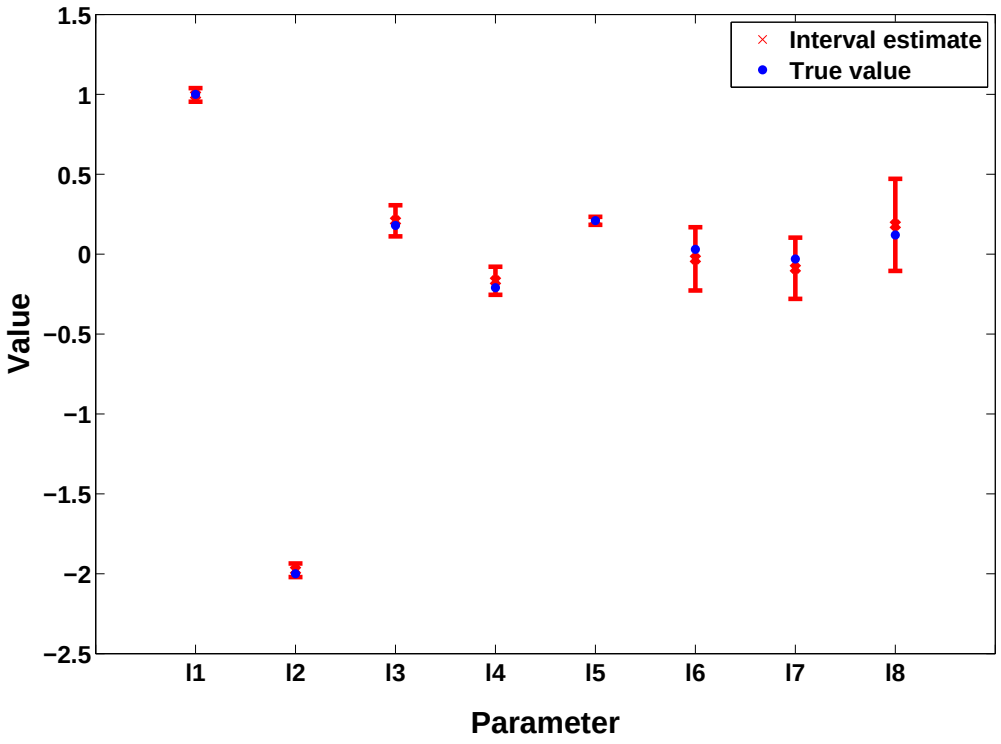

Figure 5.7. Bootstrap interval estimates for simulated data.

as the collection of the hypotheses corresponding to the coupling terms with the coefficients $\{\lambda_9,\ \lambda_{10}\}$. For the significance level $\alpha = 0.05$, our algorithm has decided for second order terms, as well as coupling between the horizontal and vertical beam oscillations, which corresponds to the truth since the sextupolar magnets were turned on. The bootstrap 90% confidence intervals for the model parameters are depicted in Figure 5.8. We notice that the confidence intervals for the parameters of the second order terms with the vertical coordinates are very large. The reason for this is that the beam was excited in the horizontal direction, and has thus too small vertical oscillation. This leads to higher uncertainty in the estimation of the related parameters.

The true values of the parameters depend on the linear optics, the strength of the chromaticity correcting sextupolar magnets, as well as the unknown optics errors. The measured data has been provided with the information that high chromaticity correction was applied, meaning that the sextupolar magnets strength was relatively high. Unfortunately, no exact values of the magnets strength was provided. This means that comparing the estimates with true values must be left for a future work that requires dedicated measurements, ideally with optimized (pencil like) beams.

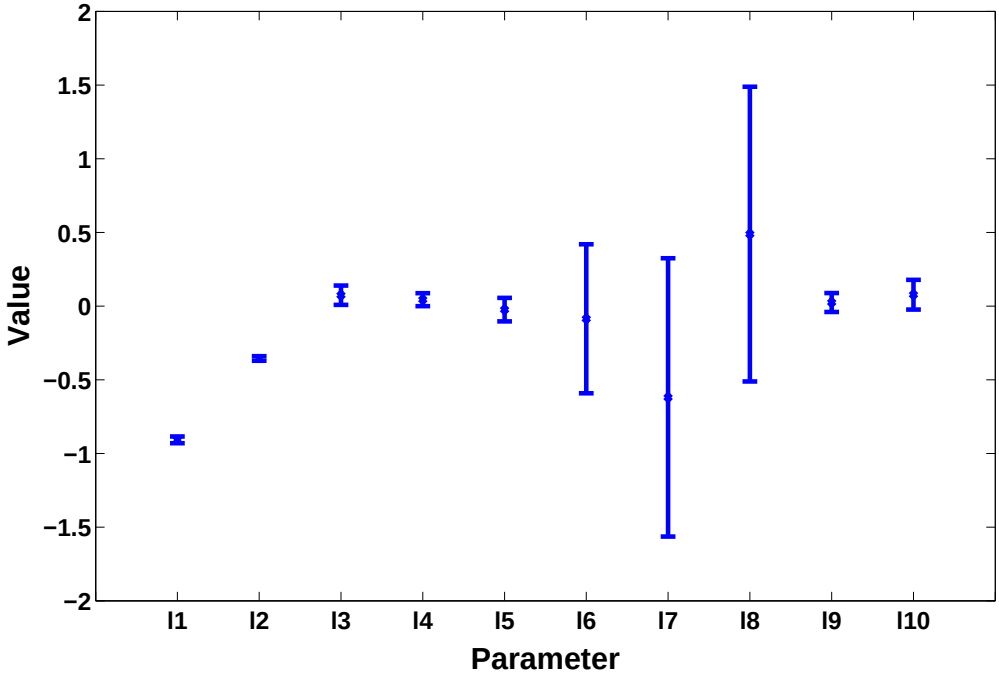

Figure 5.8. Bootstrap interval estimates for real data.

Chapter 6
Conclusions and Outlook

In this thesis, advanced signal processing techniques have been addressed for coherent transversal beam oscillations in synchrotrons. We started on the one hand with the normal accelerator operation, where the beam oscillations are a negative effect that leads to operation quality deterioration, and needs hence to be mitigated. On the other hand, we considered the beam coherent transversal oscillations as a useful diagnostics source during diagnostics operation of particle accelerators. In this Chapter, the conclusions of this thesis and suggested directions for future research with this topic are drawn.

6.1 Conclusions

For the normal operation of particle accelerators, we declared the beam transversal oscillations as undesired since they lead to beam quality deterioration and emittance blow up caused by the decoherence of the oscillating beam. The emittance blow up reduces the luminosity of the beam, and thus the collision quality [1, 2]. Therefore, beam oscillations must be suppressed in order to maintain high beam quality during acceleration. A powerful way to mitigate coherent instabilities is to employ a feedback system.

In order to cope with the noise generated at the TFS PUs, we have proposed a novel concept to use multiple PUs for estimating the beam displacement at the position with 90° phase advance before the kicker. The estimated values should be the driving feedback signal. The signals from the different PUs are delayed such that they correspond to the same bunch. Subsequently, a weighted sum of the delayed signals is suggested as an estimator of the feedback correction signal. The weighting coefficients are calculated in order to achieve an unbiased estimator, i.e., the output corresponds to the actual beam displacement at the position with 90° phase advance before the kicker for non-noisy PU signals. Furthermore, the estimator must provide the minimal noise power at the output among all linear unbiased estimators. This proposed concept is applied in our new approach to find optimal places for the PUs and the kicker around the accelerator ring such that the noise effect on the feedback quality is minimized. A new TFS design for the heavy ions synchrotrons SIS 18 and SIS 100 at the GSI has been developed and implemented using FPGA.

Our simulation results have shown significant enhancements in the SNR by applying this technique on the heavy ions synchrotron SIS 18 at the GSI. However, we should have in mind the implementation challenges of this technique, where multiple PU signals must be synchronized and processed in parallel. Our new approach to find optimal places for the PUs and the kicker around the accelerator ring has been used to evaluate the positions of the current PUs and the kicker at the SIS 18. The simulation results for the kicker and the three closest PUs have shown that the current positions are good, but still not optimal.

Furthermore, we address a novel concept for robust feedback system against optics errors or uncertainties. A kicker and multiple pickups are assumed to be used for each transversal direction. We introduced perturbation terms to the transfer matrices between the kicker and the pickups. Subsequently, the Extended Kalman Filter was used to estimate the feedback correction signal and the perturbation terms using the measurements from the pickups. The observability of the system model has been shown for the SIS 18 at the GSI. The simulation results have shown significant reduction in the estimation error with optics uncertainties compared to non-robust approaches.

Moreover, we proposed a method for measuring the phase advances and amplitude scaling between the positions of the kicker and the BPMs. Directly after applying a kick on the beam by means of the kicker, we record the BPM signals. Subsequently, we use the Second-Order Blind Identification (SOBI) algorithm to decompose the recorded noised signals into independent sources mixture [5, 6]. Finally, we determine the required optics parameters by identifying and analyzing the betatron oscillation sourced from the kick based on its mixing and temporal patterns. For a simulated scenario with the physical parameters of the SIS 18, we could reach very high precision in the estimation of the TFS required parameters.

For the diagnostics operation of particle accelerators, beam transversal oscillations can be excited deliberately. We proposed in this thesis a novel method for detecting and estimating the optics lattice non-linear components located in-between the locations of two BPMs by analyzing the beam offset oscillation signals of a BPMs-triple containing these two BPMs. Depending on the non-linear components in-between the locations of the BPMs-triple, the relationship between the beam offsets follows a multivariate polynomial accordingly. After calculating the covariance matrix of the polynomial terms, the Generalized Total Least Squares method was used to find the model parameters, and thus the non-linear components. Bootstrap techniques were used to detect the existing polynomial model orders by means of multiple hypothesis testing, and determine confidence intervals for the model parameters. We have shown a very good matching between the real and bootstrap distributions by means of Monte-Carlo simulations.

Furthermore, we have shown that choosing a proper significance value is crucial for better model selection, and thus better optics model estimation. Our simulation results have shown a good performance of our model selection approaches, and very good coverage of the confidence intervals.

6.2 Outlook

In the future, further research with theoretical and simulation studies of the TFS and its performance can be conducted while taking the space charge effects in particle accelerators with very high beam intensities into consideration. The emittance blow-up and luminosity can be evaluated for different scenarios of the space charge, TFS gains, and SNRs.

Furthermore, experimental tests can be performed with implemented TFS using multiple PUs, as well as robust TFS on real accelerated beams in particle accelerators. More intensive investigations can be conducted on the behavior and dynamics of the robust feedback system and its stability. Intensive diagnostics of the beam emittance and profile can be conducted during the operation of the TFS with different scenarios, and beam properties.

Further research can be conducted in developing more signal processing techniques to robustify the functionality of TFS against strong space charge effects and deformations of the beams during acceleration.

Concerning the diagnostics operation, further experiments and measurement campaigns can be conducted to test our addressed approaches for determining non-linear accelerator optics components and errors. The resulting model orders and the confidence intervals for the corresponding model parameters should be utilized in the search for the locations and strengths or integrated strengths of the optics non-linear components around the accelerator ring. The strength and location search can be done via minimizing some cost functions, which must be related to the estimated confidence intervals, as well as the differences between the estimated model parameters, and the multivariate polynomial coefficients resulting from each given location, orientation, and strength of nonlinear magnetic components. Deep theoretical performance analysis of the developed methods can be conducted by evaluating their reliability and consistency.

Moreover, different modeling techniques of the accelerator optics, and its way of manifestation on the beam transversal, and even longitudinal oscillations at different locations can be developed and investigated.

List of Acronyms

TFS	Transverse Feedback System
RTFS	Robust Transverse Feedback System
PU	Pickup
BPM	Beam Position Monitor
FG	Function Generator
LF	Low Frequency
HF	High Frequency
BOSS	Beam Offset Signal Suppressor
BTF	Beam Transfer Function
GSI	GSI Helmholzzentrum für Schwerionenforschung GmbH (Helmholz Center for Heavy Ions Research)
CERN	Conseil Européen pour la Recherche Nucléaire (European Organization for Nuclear Research)
HOM	Higher Order Mode
WF	Wake Field
RWI	Resistive Wall Impedance
FODO	Focusing/Defocusing with drift distance in-between
SIS	Schwerionensynchrotron (Heavy Ions Synchrotron)
LHC	Large Hadron Collider
DSP	Digital Signal Processor
MVUE	Minimum Variance Unbiased Estimator
BLUE	Best Linear Unbiased Estimator
MLE	Maximum Likelihood Estimator
LS	Least Squares

TLS	Total Least Squares
GTLS	Generalized Total Least Squares
FWE	Family Wise Error
FER	Familywise Error Rate
FWM	Familywise Missdetection
FAR	False Alarm Ratio
FDR	False Discovery Rate
STP	Simultaneous Test Procedure
BHP	Benjamini-Hochberg Procedure
A-BHP	Adaptive Benjamini-Hochberg Procedure
CI	Confidence Interval
FPGA	Field-Programmable Gate Array
MGT	Multi-Gigabit Transceiver
ADC	Analog to Digital Converter
DAC	Digital to Analog Converter
Gbps	Giga bit per Second
SFP	Small Form-factor Pluggable
RF	Radio Frequency
MMSE	Minimum Mean Square Error
MSE	Mean Square Error
RMSE	Root Mean Square Error
VS	Vector Summation
KF	Kalman Filter
EKF	Extended Kalman Filter
SOBI	Second Order Blind Identification

SNR	Signal-to-Noise Ratio
SVD	Singular Value Decomposition
FIR	Finite Impulse Response
IIR	Infinite Impulse Response
CO	Closed Orbit
ORM	Orbit Response Matrix
NTRM	Non-linear Tune Response Matrix
FAIR	Facility for Antiproton and Ion Research

List of Symbols

$\vec{E}$	Electric Field
$\vec{B}$	Magnetic Field
s	Longitudal Coordinate
x	Horizontal Coordinate
y	Vertical Coordinate
κ_x	Focusing Strength in Horizontal Direction
κ_y	Focusing Strength in Vertical Direction
p	Particle Momentum
$\beta(s)$	Betatron Function
$\alpha(s)$	Betatron Alpha Function
$\gamma(s)$	Betatron Gamma Function
$\Psi(s)$	Betatron Phase
$\beta_x(s)$	Betatron Function in Horizontal Direction
$\alpha_x(s)$	Betatron Alpha Function in Horizontal Direction
$\gamma_x(s)$	Betatron Gamma Function in Horizontal Direction
$\Psi_x(s)$	Betatron Phase in Horizontal Direction
$\beta_y(s)$	Betatron Function in Vertical Direction
$\alpha_y(s)$	Betatron Alpha Function in Vertical Direction
$\gamma_y(s)$	Betatron Gamma Function in Vertical Direction
$\Psi_y(s)$	Betatron Phase in Vertical Direction
β_{pu}	Betatron Function at the PUs Positions
α_{pu}	Betatron Alpha Function at the PUs Positions
γ_{pu}	Betatron Gamma Function at the PUs Positions
β_k	Betatron Function at the Kicker Position
α_k	Betatron Alpha Function at the Kicker Position
γ_k	Betatron Gamma Function at the Kicker Position
$\Delta\phi_1$	Phase Difference between the Kicker and the Closest PU
$\mathbf{\Delta}\phi_{\mathtt{PUs}}$	Phase Difference between Two Consecutive PUs
M	Number of PUs
ϵ	Emittance
Q	Tune
Q_x	Horizontal Tune
Q_y	Vertical Tune

q	Fractional Tune
q_x	Fractional Horizontal Tune
q_y	Fractional Vertical Tune
a	Radius of Vaccum Chamber
$W_\perp(z)$	Transverse Wake Function
$Z_\perp(\omega)$	Fourier Transform of the Transverse Wake Function
c	Speed of Light in Vacuum
$Z_\perp^{RW}$	Resistive Wall Impedance
Z_0	impedance of free space
σ	Conductivity of the Vaccum Tube Wall Material
f	Frequency
f_0	Revolution Frequency
D	Natural Damping
D_{fb}	Feedback Damping
$F(t)$	Force of Coupling with Other Particles
τ_G	Growth Time
$\mathbf{R_{zz}}$	Noise Covariance Matrix
$\tilde{x}_i$	Beam Offset at PU_i
s_{k90}	Location with 90° before the Kicker
x_{k90}	Beam Offset at the Location s_{k90}
$\mathbf{a}_{opt}$	Optimal Weights Vector
$\mathbf{b_r}$	Real Part of the Phasors of the PU Signals
$\mathbf{b_i}$	Imaginary Part of the Phasors of the PU Signals
$\mathcal{L}$	Lagrange Function
$\nabla_{\mathbf{a},\lambda_r,\lambda_i}\mathcal{L}$	Gradiant of the Lagrange Function
λ_r	The Real Parts Lagrange Multiplier
λ_i	The Imaginary Parts Lagrange Multiplier
P_N	Noise Power
$P_{N\mathtt{min}}$	Optimal Noise Power
N_D	Number of Dimensions
P_{Sig}	Signal Power
$\mathtt{SNR}_{x/y}$	SNR in Horizontal/Vertical Direction
$\mathcal{F}$	Ensemble of Unoccupied Locations around the Accelerator Ring
$\tau_{focusing}$	Index of Changing Optics
$w(\tau)$	Weighted Averaging Window

L_P	Accelerator Ring Circumference
$x_K(n)$	Beam Offset at the Kicker Location at the n^{th} Turn
$x'_K(n)$	Beam Angle at the Kicker Location at the n^{th} Turn
$\mathbf{x_K}(n)$	Beam Status Vector at the Kicker Location at the n^{th} Turn
$\mathbf{M_{KK}}$	Complete Turn Transfer Matrix
$\mathbf{M_{MS}}$	Measurement Matrix
$\mathbf{D_K}$	The Kick Vector
$\mathbf{n_p}$	Model Noise
$\mathbf{z}$	Measurement Noise
$\mathbf{M_{PKi}}$	Transfer Matrix from the Kicker to PU_i
$\mathbf{M_{KK}^{nom}}$	Nominal Complete Turn Transfer Matrix
$\mathbf{M_{MS}^{nom}}$	Nominal Measurement Matrix
$\mathbf{M_{KK}^{P}}$	Uncertainty of the Complete Turn Transfer Matrix
$\mathbf{M_{MS}^{P}}$	Uncertainty of the Measurement Matrix
$\mathbf{X}_{Ex}$	Extended Status Vector
$\mathbf{S}$	Source Signals Vector
$\mathcal{A}$	Source Mixing Matrix
ξ	chromaticity
δ_p	RMS Momentum Spread
Q_s	Synchrotron Oscillation Tune
$\mathbf{C_{SS}}(\tau)$	Covariance Matrix of the Source Signals
$\hat{\beta}_{\mathrm{TLS}}$	TLS Parameter Estimate
$\tilde{p}_m$	Adjusted p-Value
Tb_r	Test Statistic for Hypothesis H_r
t_r	Decision Threshold for Hypothesis H_r
$\mathbb{C}$	Set of complex numbers
$\mathbb{R}$	Set of real numbers
$\mathbb{Z}$	Set of integer numbers
$(\cdot)^{\mathrm{T}}$	Transpose of a vector or matrix
$(\cdot)^{\mathrm{H}}$	Conjugate transpose of a vector or matrix
$(\cdot)^*$	Conjugate of a scalar, vector, or matrix
$(\cdot)^+$	Pseudoinverse of a vector or matrix
$(\cdot)^{-1}$	Inverse of a square matrix
$\lvert\cdot\rvert$	Absolute value of a scalar
$\lvert\lvert\cdot\rvert\rvert$	Euclidean norm or 2-norm of a vector

Bibliography

[1] E. Keil, W. Schnell, and P. Strolin, "Feedback damping of horizontal beam transfer errors," Tech. Rep., CERN, October 1969.

[2] V.M. Zhabitsky, "The transverse damping systems for sis100 & sis300," Tech. Rep., GSI and Joint Institute for Nuclear Research, 2006.

[3] R. Rojko, *New Concepts for Transverse Beam Stability in High-Current Heavy-Ion Synchrotrons*, Ph.D. thesis, TU Darmstadt, 2003.

[4] M. Lonza, "Multi-bunch feedback systems," in *Cern Accelerator School*, Sigtuna, SWEDEN, 2007.

[5] A. Belouchrani, K. Abed-Meraim, Jean-Francois Cardoso, and E. Moulines, "A blind source separation technique using second-order statistics," *IEEE Transactions on Signal Processing*, vol. 45, pp. 434–444, 1997.

[6] X. Huang, S. Y. Lee, E. Prebys, and R. Tomlin, "Application of independent component analysis for beam diagnosis," in *Proceedings of the PAC05*, 2005.

[7] S. Y. Lee, *Accelerator Physics*, World Scientific Publishing Company Incorporated, 2012.

[8] G. Franchetti, A. Parfenova, and I. Hofmann, "Measuring localized nonlinear components in a circular accelerator with a nonlinear tune response matrix," *Physical Review Special Topics-Accelerators and Beams*, vol. 11, no. 9, pp. 094001, 2008.

[9] A. Parfenova, G. Franchetti, and I. Hofmann, "Measuring ring nonlinear components via induced linear feeddown," in *EPAC08*, 2008, pp. 3137–3139.

[10] J. Irwin, "Understanding nonlinear effects and losses," Tech. Rep. SLAC-PUB-95-6831, SLAC, 1995.

[11] Gerhard Kraft, "Tumor therapy with heavy charged particles," *Progress in Particle and Nuclear Physics*, vol. 45, pp. S473–S544, 2000.

[12] Phillip Sprangle, Antonio Ting, Eric Esarey, and Amnon Fisher, "Tunable, short pulse hard x-rays from a compact laser synchrotron source," *Journal of applied physics*, vol. 72, no. 11, pp. 5032–5038, 1992.

[13] J. Peterson W. Chou, "The ssc transverse feedback systems," Tech. Rep., Superconducting Super Collider Laboratory, 1993.

[14] M. Kirk, U. Blell, and O. Boine-Frankenheim, "Maschinenexperimente zur transversalen strahlanregung und inbetriebnahme des tfs am sis," Tech. Rep., GSI, 1992.

[15] Frank Zimmermann, "Comparison of calculated with measured dynamic aperture," Tech. Rep., Stanford Linear Accelerator Center, Menlo Park, CA (United States). Funding organisation: USDOE, Washington, DC (United States), 1994.

[16] G. Franchetti and I. Hofmann, "Resonance trapping due to space charge and synchrotron motion, in theory, simulations, and experiments," *Proceedings of the 39th ICFA advanced beam dynamics workshop*, 2007.

[17] A. Bazzani, E. Todesco, G. Turchetti, and G. Servizi, "Cern yellow report 94-02," 1994.

[18] D. Bulfone, V. Forchi, M. Lonza, and L. Zambon, "Bunch-by-bunch control of instabilities with the elettra/sls digital feedback systems," in *Proceedings of ICALEPCS 2003*, 2003.

[19] T. Nakamura et al., "Transverse bunch-by-bunch feedback system for the spring-8 storage ring," in *9th European Particle Accelerator Conference*, Lucerne, Switzerland, 2004.

[20] W.X. Cheng et al., "Single-loop two dimensional transverse feedback for photon factory," in *Proceedings of EPAC2006*, Edinburgh, Scotland, 2006.

[21] H. Hindi et al., "A formal approach to the design of multibunch feedback systems: Lqg controllers," in *Proceedings of EPAC94*, London, UK, 1994.

[22] James Safranek, "Experimental determination of storage ring optics using orbit response measurements," *Nuclear Instruments and Methods in Physics Research Section A: Accelerators, Spectrometers, Detectors and Associated Equipment*, vol. 388, no. 1, pp. 27–36, 1997.

[23] Y. Chung, G. Decker, and K. Evans Jr, "Closed orbit correction using singular value decomposition of the response matrix," in *Particle Accelerator Conference, 1993., Proceedings of the 1993*. IEEE, 1993, pp. 2263–2265.

[24] M. Boge, M. Dehler, T. Schilcher, V. Schlott, and R. Ursic, "Fast closed orbit control in the sls storage ring," in *Particle Accelerator Conference, 1999. Proceedings of the 1999*. IEEE, 1999, vol. 2, pp. 1129–1131.

[25] A. Parfenova and G. Franchetti, "Linear and nonlinear beam optics studies in the sis18," in *PAC09*, 2009, vol. 9, pp. 3826–3828.

[26] R. Tomás, G. Arduini, G. Rumolo, F. Zimmermann, and A. Faus-Golfe, "Improved algorithms to determine the non-linear optics model of the sps from non-linear chromaticity," in *Proceedings of PAC07*. IEEE, 2007, pp. 4231–4233.

[27] G. Arduini, F. Zimmermann, A. Faus-Golfe, and R. Tomas, "2003–2004 nonlinear optics measurements and modeling for the cern sps," in *Proceedings of 2005 Particle Accelerator Conference*. IEEE, 2005, pp. 1171–1173.

[28] K. Wille, *The physics of particle accelerators: an introduction*, Oxford University Press, 2000.

[29] Philip J Bryant and Kjell Johnsen, *The principles of circular accelerators and storage rings*, Cambridge University Press, 2005.

[30] Mario Conte and William W MacKay, *An introduction to the physics of particle accelerators*, vol. 160, World Scientific, 1991.

[31] Richard Clinton Fernow, *Introduction to experimental particle physics*, Cambridge University Press, 1989.

[32] Helmut Wiedemann et al., *Particle accelerator physics*, vol. 314, Springer, 2007.

[33] Donald A Edwards and Mike J Syphers, *An introduction to the physics of high energy accelerators*, John Wiley & Sons, 2008.

[34] B. Franczak, "Sis parameter list," Tech. Rep., GSI, 1987.

[35] Oliver Boine-Frankenheim, "Introduction to accelerator physics," Lecture notes, 2010, TU Darmstadt.

[36] P. J. Bryant, "Beam transfer lines," in *Jyvaeskylae 1992, Proceedings, General accelerator physics*, Geneva, 1992, CERN, vol. 1, pp. 219–238.

[37] E. Wilson, "ransverse beam dynamics," in *Jyvaeskylae 1992, Proceedings, General accelerator physics*, Geneva, 1992, CERN, vol. 1, pp. 131–158.

[38] M. Alhumaidi and A.M. Zoubir, "Optics non-linear components measurement using bpm signals," in *Proceedings of IBIC2013*, Oxford, UK, 2013.

[39] Werner Herr and Bruno Muratori, "Concept of luminosity," in *CERN Accelerator School (CAS): Intermediate Course on Accelerator Physics*, Zeuthen, Germany, 2003, pp. 361–378.

[40] M. Giovannozzi, "Sources of emittance growth," in *Cern Accelerator School (CAS)*, 2011.

[41] J. S. Berg, "Coherent modes for multiple nonrigid bunches in a storage ring," .

[42] P. J. Bryant and K. Johnsen, "The principles of circular accelerators and storage rings," Cambridge Univ. Pr., 1993.

[43] B. Zotter and F. Sacherer, "Transverse instabilities of relativistic particle beams in accelerators and storage rings," International School Of Particle Accelerators, 1977.

[44] L. Palumbo, V.G. Vaccaro, and M. Zobov, "Wake fields and impedance," Tech. Rep., Laboratori Nazinali di Frascati, 1994.

[45] A. Hofmann, "Beam instabilities," in *CERN Accelerator School*. CERN, 1993, pp. 307–330.

[46] A. Hofmann, "Kinetic theory," in *CERN Accelerator School*, 1993, pp. 259–274.

[47] L. Palumbo, V. G. Vaccaro, and M. Zobov, "Wake fields and impedance," 1994, LNF-94-041-P.

[48] H. Wiedemann, "Particle accelerator physics: Basic principles and linear beam dynamics," Springer, 1993.

[49] T. Weiland and R. Wanzenberg, "Wake fields and impedance," 1991, DESY-M-91-06.

[50] G. Rumolo, "Beam instabilities," in *Cern Accelerator School (CAS)*, 2011.

[51] Alexander Wu Chao, *Physics of Collective Beam Instabilities in High Energy Accelerators*, Wiley, 1993.

[52] W. Chou, "Review of beam instability studies for the ssc," in *Proceedings of the Particle Accelerator Conference 1995*, 1995.

[53] U. Niedermayer and O. Boine-Frankenheim, "Analytical and numerical calculations of resistive wall impedances for thin beam pipe structures at low frequencies," *Nuclear Instruments and Methods in Physics Research A*, vol. 687, pp. 51–61, 2012.

[54] L. Wang et al., "Resistive wall instability in the damping rings of the ilc," Tech. Rep., SLAC, 2006.

[55] M. Schuh, F.Gerigk, J.Tueckmantel, and C.P.Welsch, "Higher order mode analysis of the spl cavities," in *Proceedings of IPAC'10*, 2010.

[56] R.A. Bosch and C.S. Hsue, "Suppression of longitudinal coupled-bunch instabilities by a passive higher harmonic cavity," in *Proceedings of the Particle Accelerator Conference 1993*, 1993.

[57] M. Zobov, R. Boni, A. Gallo, A. Ghigo, F. Marcellini, L. Palumbo, M. Serio, B. Spataro, and G. Vignola, "Measures to reduce the impedance of parasitic resonant modes in the daone vacuum chamber," in *14th Advanced ICFA Beam Dynamics Workshop*, 1997.

[58] V. M. Zhabitsky, "The transverse damping systems for sis100 & sis300," Tech. Rep., GSI and Joint Institute for Nuclear Research.

[59] M. Svandrlik, C. J. Bocchetta, A. Fabris, F. Iazzourene, E. Karantzoulis, R. Nagaoka, C. Pasotti, L. Tosi, R. P. Walker, and A. Wrulich, "The cure of multibunch instabilities in elettra," in *Proceedings of the PAC95*, 1995.

[60] M. Alhumaidi and A.M. Zoubir, "Using multiple pickups for transverse feedback systems and optimal pickups-kicker placement for noise power minimization," *Nuclear Instruments and Methods in Physics Research Section A*, vol. 761, pp. 79–85, 2014.

[61] M. Alhumaidi and A. M. Zoubir, "A transverse feedback system using multiple pickups for noise minimization," in *2nd International Particle Accelerator Conference*, San Sebastian, SPAIN, 2011.

[62] Robert M. Gray and Lee D. Davisson, *An Introduction to Statistical Signal Processing*, Cambridge University Press, 2004.

[63] P. J. Bryant and K. Johnsen, *The Principles of Circular Accelerators and Storage Rings*, Cambridge University Press, 1993.

[64] Xilinx, "Virtex-6 fpga ml605 evaluation kit," .

[65] Xilinx, "Aurora link-layer protocol," .

[66] Xilinx, "Logicore tm ip aurora 8b/10b v5.2 user guide," July 2010.

[67] M. Alhumaidi and A.M. Zoubir, "A robust transverse feedback system," in *3rd International Particle Accelerator Conference*, New Orleans, Louisiana, USA, 2012.

[68] Rudolph Emil Kalman, "A new approach to linear filtering and prediction problems," *Journal of Fluids Engineering*, vol. 82, no. 1, pp. 35–45, 1960.

[69] M. S. Grewal and A.P. Andrews, *Kalman Filtering: Theory and Practice Using MATLAB*, John Wiley & Sons, 2001.

[70] Francesca Albertini and Domenico D'Alessandro, "Remarks on the observability of nonlinear discrete time systems," in *System Modelling and Optimization*, pp. 155–162. Springer, 1996.

[71] Kaare Brandt Petersen and Michael Syskind Pedersen, "The matrix cookbook," *Technical University of Denmark*, pp. 7–15, 2008.

[72] Greg Welch and Gary Bishop, "An introduction to the kalman filter," 1995.

[73] Arthur Gelb, *Applied optimal estimation*, MIT press, 1974.

[74] M. Alhumaidi, J. Grieser, and A.M. Zoubir, "Determination of optics transfer between the kicker and bpms for transverse feedback system," in *Proceedings of IPAC2013*, 2013.

[75] Vladimir Kornilov and Oliver Boine-Frankenheim, "Transverse decoherence and coherent spectra in long bunches with space charge," *Physical Review Special Topics-Accelerators and Beams*, vol. 15, no. 11, pp. 114201, 2012.

[76] S.Y. Lee., "Decoherence of kicked beams ii," Tech. Rep., SSCL, 1991.

[77] R.E. Meller, A.W. Chao, J.M. Peterson, S.G. Peggs, and M. Furman, "Decoherence of kicked beams," Tech. Rep. No. SSC-N-360, SSC Report, 1987.

[78] Lieven De Lathauwer and Joséphine Castaing, "Second-order blind identification of underdetermined mixtures," in *Independent Component Analysis and Blind Signal Separation*, pp. 40–47. Springer, 2006.

[79] G. Arduini, R. Tomas, F. Zimmermann, A. Faus-Golfe, and N. Iida, "2002 nonlinear optics measurements and modelling for the cern sps," in *Proceedings of the 2003 Particle Accelerator Conference*. IEEE, 2003, vol. 4, pp. 2240–2242.

[80] Sabine Van Huffel and Joos Vandewalle, "Analysis and properties of the generalized total least squares problem ax≈b when some or all columns in a are subject to error," *SIAM Journal on Matrix Analysis and Applications*, vol. 10, no. 3, pp. 294–315, 1989.

[81] Ivan Markovsky and Sabine Van Huffel, "Overview of total least-squares methods," *Signal processing*, vol. 87, no. 10, pp. 2283–2302, 2007.

[82] Yosef Hochberg and Ajit C. Tamhane, *Multiple comparison procedures*, John Wiley & Sons, Inc., 1987.

[83] Peter H. Westfall and S. Stanley Young, *Resampling-based multiple testing: Examples and methods for p-value adjustment*, vol. 279, John Wiley & Sons, 1993.

[84] Fiky Y. Suratman, *Spectrum Sensing in Cognitive Radio: Bootstrap and Sequential Detection Approaches*, Ph.D. thesis, TU Darmstadt, 2014.

[85] Pei-Jung Chung, Johann F. Böhme, Christoph F. Mecklenbrauker, and Alfred O. Hero, "Detection of the number of signals using the benjamini-hochberg procedure," *Signal Processing, IEEE Transactions on*, vol. 55, no. 6, pp. 2497–2508, 2007.

[86] Abdelhak M. Zoubir and Johann F. Böhme, "Bootstrap multiple tests applied to sensor location," *IEEE Transactions on Signal Processing*, vol. 43, no. 6, pp. 1386–1396, 1995.

[87] Priyadip Ray and Pramod K. Varshney, "False discovery rate based sensor decision rules for the network-wide distributed detection problem," *IEEE Transactions on Aerospace and Electronic Systems*, vol. 47, no. 3, pp. 1785–1799, 2011.

[88] Erhan Baki Ermis and Venkatesh Saligrama, "Distributed detection in sensor networks with limited range multimodal sensors," *IEEE Transactions on Signal Processing*, vol. 58, no. 2, pp. 843–858, 2010.

[89] Gerard V. Dallal, *The little handbook of statistical practice*, Gerard V. Dallal, 1999.

[90] Yoav Benjamini and Yosef Hochberg, "Controlling the false discovery rate: a practical and powerful approach to multiple testing," *Journal of the Royal Statistical Society. Series B (Methodological)*, pp. 289–300, 1995.

[91] Yoav Benjamini and Yosef Hochberg, "On the adaptive control of the false discovery rate in multiple testing with independent statistics," *Journal of Educational and Behavioral Statistics*, vol. 25, no. 1, pp. 60–83, 2000.

[92] Sanat K. Sarkar, "False discovery and false nondiscovery rates in single-step multiple testing procedures," *The Annals of Statistics*, pp. 394–415, 2006.

[93] Wenge Guo and Joseph Romano, "A generalized sidak-holm procedure and control of generalized error rates under independence," *Statistical applications in genetics and molecular biology*, vol. 6, no. 1, 2007.

[94] Charles W. Dunnett and Ajit C. Tamhane, "Step-down multiple tests for comparing treatments with a control in unbalanced one-way layouts," *Statistics in Medicine*, vol. 10, no. 6, pp. 939–947, 1991.

[95] Mark J. van der Laan, Sandrine Dudoit, and Katherine S. Pollard, "Multiple testing. part ii. step-down procedures for control of the family-wise error rate," *Statistical Applications in Genetics and Molecular Biology*, vol. 3, no. 1, 2004.

[96] Sture Holm, "A simple sequentially rejective multiple test procedure," *Scandinavian journal of statistics*, pp. 65–70, 1979.

[97] Yosef Hochberg, "A sharper bonferroni procedure for multiple tests of significance," *Biometrika*, vol. 75, no. 4, pp. 800–802, 1988.

[98] Burt S. Holland and Margaret DiPonzio Copenhaver, "An improved sequentially rejective bonferroni test procedure," *Biometrics*, pp. 417–423, 1987.

[99] Juliet Popper Shaffer, "Modified sequentially rejective multiple test procedures," *Journal of the American Statistical Association*, vol. 81, no. 395, pp. 826–831, 1986.

[100] Burt S. Holland and Margaret DiPonzio Copenhaver, "An improved sequentially rejective bonferroni test procedure," *Biometrics*, pp. 417–423, 1987.

[101] Leon Jay Gleser, "Estimation in a multivariate" errors in variables" regression model: large sample results," *The Annals of Statistics*, pp. 24–44, 1981.

[102] Michal Pešta, "Total least squares and bootstrapping with applications in calibration," *Statistics: A Journal of Theoretical and Applied Statistics*, vol. 47, no. 5, pp. 966–991, 2013.

[103] Abdelhak M. Zoubir and D. Robert Iskander, *Bootstrap techniques for signal processing*, Cambridge University Press, 2004.

[104] Dimitris N. Politis, "Computer-intensive methods in statistical analysis," *IEEE Signal Processing Magazine*, vol. 15, no. 1, pp. 39–55, 1998.

[105] Bogdan Matei and Peter Meer, "Bootstrapping errors-in-variables models," in *Vision Algorithms: Theory and Practice*, pp. 236–252. Springer, 2000.

Lebenslauf

Name:	Mouhammad Alhumaidi
Anschrift:	Ulmer Straße 8 — 87700 Memmingen
Geburtsdatum:	01.01.1984
Geburtsort:	Raqa / Syrien
Familienstand:	verheiratet

Schulausbildung

09/1989-06/1998	Grund- und Mittelschule in Ratlah, Raqa / Syrien
09/1998-07/2001	Alrasheed Gymnasium in Raqa / Syrien

Studium

09/2001-12/2006	Studium der Kommunikationstechnik am Higher Institute for Applied Sciences and Technology (HIAST), Damaskus, Syrien, Studienabschluß: Engineering Diploma
10/2008-10/2010	Studium der Elektrotechnik und Informationstechnik, Vertiefung: Nachrichten- und Kommunikationsstechnik, an der TU Darmstadt, Studienabschluß: Master of Science

Berufstätigkeit

11/2010-10/2014	wissenschaftlicher Mitarbeiter am Fachgebiet Signalverarbeitung, Institut für Nachrichtentechnik, Technische Universität Darmstadt
seit 10/2014	Entwicklungsingenieur Algorithmik für Radarsysteme, Continental AG

Erklärung laut §9 der Promotionsordnung

Ich versichere hiermit, dass ich die vorliegende Dissertation allein und nur unter Verwendung der angegebenen Literatur verfasst habe. Die Arbeit hat bisher noch nicht zu Prüfungszwecken gedient.

Darmstadt, 14. Januar 2015,